Direct numerical simulation on turbulent/non-turbulent interface in compressible turbulent boundary layers
圧縮性乱流境界層中の乱流・非乱流界面に関する直接数値計算

A thesis presented for the degree of Doctor of Philosophy

Fluid Dynamics Laboratory
Department of Aerospace Engineering
Graduate school of Engineering
Nagoya University

ZHANG　Xinxian

Contents

Chapter 1

Introduction

1.1 Backgroud

Turbulent boundary layer (TBL) plays an important role in many engineering applications and geophysical flows. For example, the development and separation of turbulent boundary layer can significantly affect the lift, drag and also the instability of the aircraft and vehicle as shown in figures 1.1 (a) and (b), respectively.

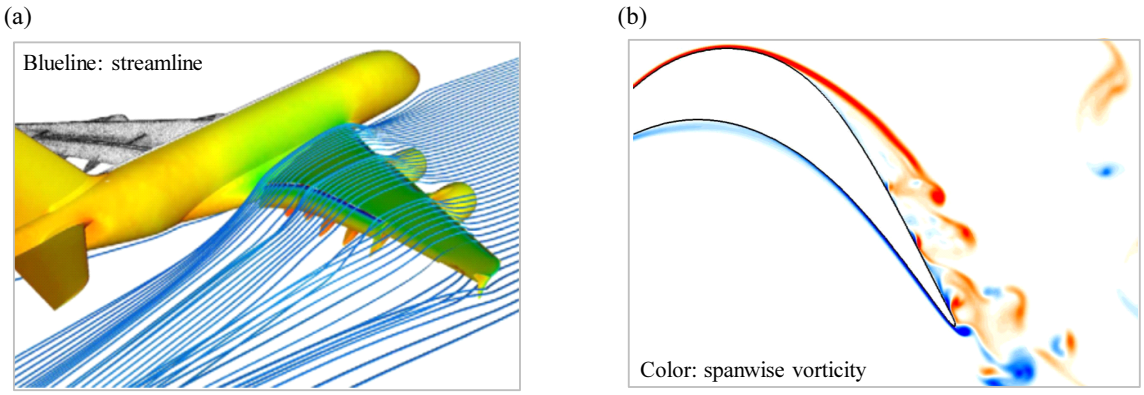

Figure 1.1 (a) Flow passing through an A320 airfoil.[1] (b) Flow around a blade inside a turbine.[2]

Passive scalar is also important to be investigated for studying turbulence, which is a diffusive contaminant in a fluid flow. Understanding the behavior of passive scalar is a necessary step in understanding turbulent mixing, chemical reaction or combustion.[3] For example, passive scalar can show the mixing degree of two different flows in a reaction flow.

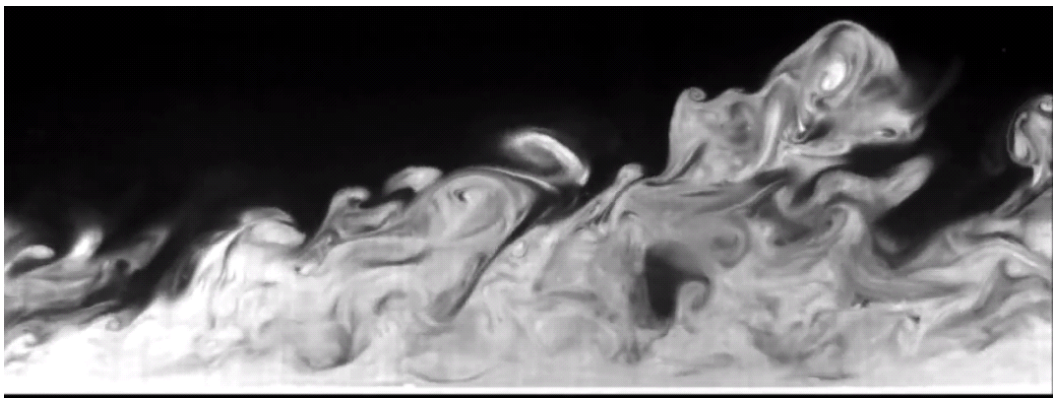

Figure 1.2 Instantaneous flow visualization of a spatial developing boundary layer.[4]

1.2 Turbulent/Non-turbulent interface

Over the past few decades, a large number of studies[5–7] have been devoted for understanding TBL from various points of view. Turbulent boundary layers are known as highly intermittent flows, where both turbulent and non-turbulent (laminar) fluids coexist as shown in figure 1.2. This turbulent boundary layer is visualized using fluorescein injected through a spanwise oriented slot.[4] Here, it can be clearly seen that the turbulent and non-turbulent flows are separated by an apparent boundary. In 1928, Prandtl[8] firstly pointed out the existence of this sharp interface between turbulent and non-turbulent flows in the intermittent region, which is called turbulent/non-turbulent interface (TNTI). After decades, the existence of TNTI was firstly examined in a free shear layer by Corrsin and Kistler,[9] and the recent studies[10,11] have revealed that the TNTI is a thin layer with finite thickness. The turbulent and non-turbulent flow regions are separated by this TNTI layer, where flow properties, such as enstrophy, kinetic energy dissipation, scalar concentration, sharply change in this layer so that they are adjusted between the turbulent and non-turbulent flows.[12] This layer is also important for the exchanges of substance, energy, and heat between turbulent and non-turbulent flow and is also related to the spatial development of turbulence.[13] Therefore, it is very important to understand the characteristics of TNTI.

The spatial distribution of turbulent fluids also plays an important role in scalar mixing in TBLs. Because the turbulence can create small-scale fluctuating scalar fields, which enhances turbulent mixing at molecular level. Modeling of turbulent mixing is crucial in numerical simulations of reacting flows[14] and combustions.[15] One of the key quantiles in modeling of turbulent reacting flows is scalar dissipation rate, which strongly depends on the characteristics of turbulence.[16] Many models developed for simulating turbu-

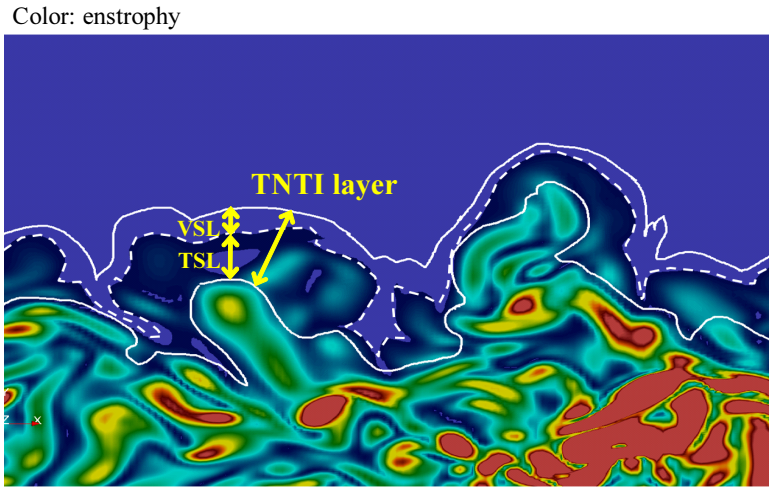

Figure 1.3 The concept of inner structures in TNTI layer.

lent reacting flows contain the scalar dissipation rate as an unknown variable.[17–20] The TNTI often appears near the interface that separates two streams with different chemical substances, the mixing process near the TNTI can be important in chemically reacting flows,[21–23] where the chemical reaction rate is strongly affected by turbulence. Therefore, it is also important to investigate the characteristics of scalar mixing near the TNTI.

1.3 Rencent studies on TNTI

The TNTI appears in many canonical flows such as jets, wakes, and boundary layers. Recently, with the improvement of supercomputer resources and laser-based measurement techniques, many numerical simulations and experiments have been conducting to investigate the TNTI in canonical turbulent flows as summarized in the review paper.[10] The flow properties near the TNTI in these flows have been investigated with the conditional statistics computed as a function of the distance from the TNTI.[11] The TNTI layer is found to consists of two (sub) layers with different dynamical characteristics as shown in figure 1.3. The outer part is called viscous superlayer (VSL), where viscous effects dominate vorticity evolution, while the region between the VSL and turbulent core region is called turbulent sublayer (TSL),[24] where the inviscid effects, such as vortex stretching, become important.

The phenomenon of mass transferred from the non-turbulent region to turbulent region is called the turbulent entrainment process, by which turbulence spatially grows. As studied in pervious study,[25] the entrainment caused by large-scale eddies is called

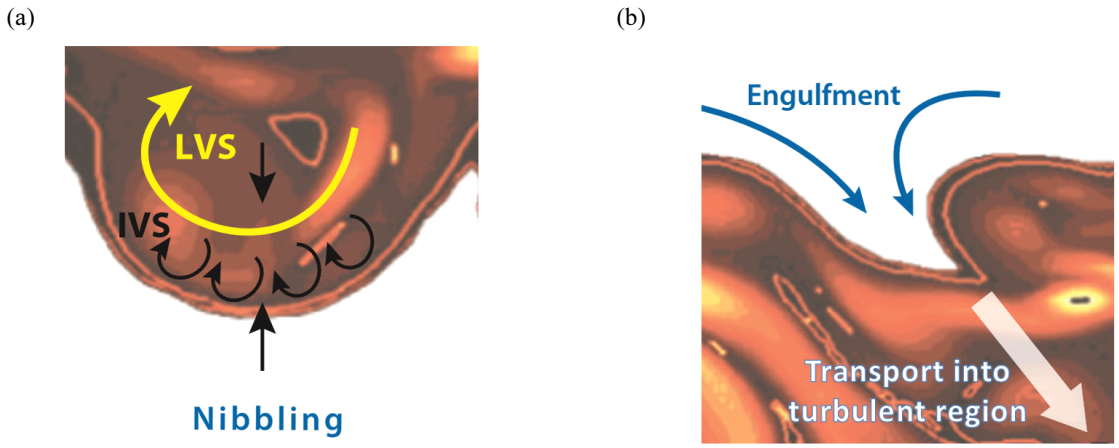

Figure 1.4 Two type of turbulent entrainment process:[10] (a)Nibbling caused by small-scale eddies; (b)Engulfment caused by large-scale eddies. (IVS: intense vorticity structure, LVS: large-scale vortices.)

engulfment, and the entrainment process caused by small-scale eddies near the TNTI is referred as nibbling(figure 1.4). The nibbling-type entrainment is aroused by the viscous diffusion of vorticity near the TNTI layer while the engulfment is described as the non-turbulent flow which is drawn into the turbulent side by large-scale eddies before acquiring vorticity. The dominant mechanism for the entrainment process has been argued for many years. Recent studies have suggested that the nibbling process is responsible for the entrainment mechanism, and large-scale features of turbulence impose the total entrainment rate.[13, 25, 26]

The geometry of TNTI is also an important issue for understanding the entrainment process: large pockets structures on the TNTI interface can indraft the non-turbulent fluids into the turbulent region before acquiring vorticity (engulfment) if the TNTI interface is intensely folded;[27] It is doubtless that the complex geometry of the interface is highly related to the total entrainment rate because the total entrainment rate can be expressed as the surface integral of the local entrainment velocity (nibbling). Therefore, it may need more information for the relation between nibbling and engulfment as mentioned by Borrell and Jiménez.[28] Some recent studies have revealed the influence of large-scale structures on the geometry of TNTI in the boundary layer,[29, 30] which can make differences in the entrainment process between the TBLs and free shear flows, because the large-scale motions depend on flow types.

Furthermore, the turbulent flow under the TNTI layer contains eddies with a wide range of scales, and all length scales can affect the properties and geometry of the TNTI layer. Therefore, motions from the smallest to the largest scales need to be captured

in measurement or simulations. Especially in the direct numerical simulations (DNS), all scales should be resolved, and insufficient resolution can directly affect computational results. With the DNS, researchers are able to access three-dimensional data of all quantities, which is difficult to obtain in experiments especially in high-speed flows. However, the resolution of TNTI in DNS for TBLs has not been investigated.

Recently, the TNTI in TBLs have been studied in experiments[30–34] and direct numerical simulations.[28–30,35] Some characteristics of the TNTI in TBLs are found to be similar with the ones in the free shear flows,[36] e.g., vorticity jump in the TNTI layer, and fractal features of the TNTI. There are still less studies on the TNTI in the turbulent boundary layer compared with in free shear flows. Especially, TNTI studies in TBL has been done in incompressible flows.

1.4 TNTI in high-speed flows

In many aerospace engineering applications, the TBLs often develop in a transonic or supersonic free-stream, where compressibility is no longer negligible.[37] Compressibility effects on the TNTI have been studied in compressible mixing layers.[38–41] There is only a few experimental studies on the TNTI in high-speed TBLs,[34,42] in which they conducted fractal analysis on the TNTI of supersonic turbulent boundary layer with the experimental data. However, the measurement near the TNTI is very limited and difficult especially in high speed flows so that many characteristics about TNTI in compressible TBLs have not been investigated.

1.5 Objectives and structure

1.5.1 Objectives

Even through there are already some DNS studies on the TNTI in TBL,[28,29,35] the grid setting has not been evaluated with the consideration of the resolution on the TNTI in TBL. Since the most DNS studies for TBL focus on the near-wall region, where the grid spacing are carefully considered in usual DNS for TBL, while the intermittent region has not been fully considered.

The TNTI has been extensively studied in recent studies on free shear flows and some similar characteristics of the TNTI are also found in the TBL.[36] However, there are less studies on the TNTI in the TBL than in free shear flows, and many things remains unclear for the entrainment process near TNTI layer. Although a high-speed regime is of great importance in realistic for aerospace engineering applications, most studies on the TNTI have been done in incompressible flows. However, the TNTI in compressible turbulence is still less understood compared with the one in incompressible flows.

Understanding the characteristics of the TNTI is greatly important in modeling and predicting the spatial development of turbulence as well as the flow control based on the turbulent structures near the TNTI. As described above, it is important to investigate the TNTI in compressible TBLs. In this study, direct numerical simulations (DNSs) with two types of grid setting are performed for both the subsonic and supersonic turbulent boundary layers in order to investigate the spatial resolution effects on TNTI, compressibility effects, entrainment process, as well as the development of the high-speed turbulent boundary layers.

The main objectives in the present thesis are written in the following list:

a. Develop the DNS code for the compressible TBLs with two types of grid setting.

b. Validate the DNSs code based on the study on fundamental characteristics of the compressible TBLs.

c. Evaluate a reasonable grid setting for the TNTI study in compressible TBLs.

d. Investigate the compressibility effects on TNTI in compressible TBLs.

e. Elucidate the physical mechanism of the entrainment in compressible TBLs.

1.5.2 Structure

In this study, DNS is performed for temporally developing subsonic and supersonic TBLs in order to investigate the characteristics of the TNTI in the compressible TBLs and the influence of the spatial resolution near the TNTI on the analysis on the TNTI. This thesis is organized as follows. The details of DNS are presented in section 2. In chapter 3,

the classical statistics of the compressible TBLs are presented and compared with previous studies. Chapter 4 discusses the effects of DNS spatial resolution and compressibility on TNTI followed by the statistical analysis. Chapter 5 investigate physical mechanism of the entrainment in compressible TBLs. The real-world data circulation (RWDC) and the relation with present study is discussed in chapter 6. Finally, the conclusion is summarized the Conclusion.

1.6 Major nomenclature

U_W	Wall velocity	[m/s]
u	Streamwise velocity	[m/s]
v	Wall-normal velocity	[m/s]
w	Spanwise velocity	[m/s]
$\boldsymbol{u}$	Velocity vector	[m/s]
ω	Vorticity magnitude	[1/s]
$\boldsymbol{\omega}$	Vorticity vector	[1/s]
T	Temperature	[K]
P	Pressure	[Pa]
ρ	Density	[kg/m^3]
t	Time	[s]
μ	Viscosity	[Pa $\cdot$ s]
ν	Kinematic viscosity	[m^2/s]
c	Sound speed	[m/s]
ϕ	Passive scalar	
$\overline{f}$	Average	
$\widetilde{f}$	Favre average	

Superscript

$'$: Fluctuation
$''$: Fluctuation about the Favre average

Subscript

rms : Root-mean square (RMS)
IB : Irrotational boundary

Other symbols will be explained in the text.

Chapter 2

Direct numerical simulations of temporally developing boundary layers

The numerical method and computational conditions are described in this chapter.

2.1 Governing equations

The governing equations in present simulations are the three-dimensional compressible Navier-Stokes equations and passive scalar transport equation. The conservation equations of mass, momentum, energy, and passive scalar ϕ are expressed as following:[43]

$$\frac{\partial \rho}{\partial t} + \frac{\partial \rho u_j}{\partial x_j} = 0, \tag{2.1}$$

$$\frac{\partial \rho u_i}{\partial t} + \frac{\partial \rho u_i u_j}{\partial x_j} = -\frac{\partial P}{\partial x_i} + \frac{\partial \tau_{ij}}{\partial x_j}, \tag{2.2}$$

$$\frac{\partial \rho T}{\partial t} + \frac{\partial \rho T u_j}{\partial x_j} = -(\gamma - 1) P \frac{\partial u_j}{\partial x_j} + \gamma \frac{\partial}{\partial x_j}\left(k \frac{\partial T}{\partial x_j}\right) + (\gamma - 1)\tau_{ij}\frac{\partial u_i}{\partial x_j}, \tag{2.3}$$

$$\frac{\partial \rho \phi}{\partial t} + \frac{\partial \rho u_j \phi}{\partial x_j} = \frac{\partial}{\partial x_j}\left(\rho D_m \frac{\partial \phi}{\partial x_j}\right), \tag{2.4}$$

with the equation of state for the perfect gas:

$$P = \rho R T. \tag{2.5}$$

The viscous stress tensor τ_{ij} is represented with Stokes hypothesis as below:

$$\tau_{ij} = \mu\left(\frac{\partial u_i}{\partial x_j} + \frac{\partial u_j}{\partial x_i} - \frac{2}{3}\delta_{ij}\frac{\partial u_k}{\partial x_k}\right). \tag{2.6}$$

Here, u_i is the velocity, ρ is the density, P is the pressure, T is the temperature, μ is the dynamic viscosity, k is the thermal conductivity, D_m is the molecular diffusivity for the

passive scalar ϕ, and $\gamma = C_p/C_v = 1.4$, $R = C_p - C_v = 287$ [J/(kg · K)] are the ratio between specific heats and the gas constant, respectively. The temperature-dependent viscosity μ is provided by Sutherland's law:

$$\mu = \mu_s \left(\frac{T}{T_s}\right)^{3/2} \frac{T_s + S}{T + S}, \tag{2.7}$$

where $\mu_s = 1.742 \times 10^{-5}$ [Pa·s], $T_s = 273$ [K], and $S = 110.4$ [K]. Prandtl number $Pr = \mu C_p/k = 0.71$ and Schmidt number $Sc = \mu/\rho D_m = 1$ are assumed in present study.

2.2 Temporally developing direct numerical simulation

DNS is a powerful tool to analyze the behavior of turbulence, because it directly solves the full equations which describe turbulence (Navior-Stokes equations) without any turbulence model. DNS also provides three-dimensional data of all quantities, which is very difficult to obtain in experiments with current technique. Many numerical studies have investigated spatially developing turbulent boundary layers.[44, 45] However, the DNS of spatially developing turbulent boundary layer requires a very long computational domain, which makes the cost of DNS prohibitive for high Reynolds number. In 1988, Spalart[46] developed a technique, which assumes that the boundary layer grows so slowly in the streamwise direction that the turbulence can be approximately treated as homogeneous in this direction. This technique can be realized in numerical simulation by using periodic conditions in streamwise and spanwise directions. Because of the expensive computational costs of spatial simulations, temporal simulations are often used in fundamental researches of turbulence.[47, 48] In recent numerical studies, it has been shown that temporal simulations of both compressible boundary layers[49, 50] and incompressible boundary layers[48] are able to reproduce important statistics of spatial counterparts of these flows. It should be noted that the temporal approach is also found to be useful in free shear flows, such as mixing layer[21] and jet.[51]

In present study, a three-dimensional computational domain with a size of $(L_x \times L_y \times L_z)$ is considered as shown in figure 2.1. The wall is at the bottom of the computational domain, the origin of the coordinate system is set at the center of the wall. The x, y, and z directions represent the streamwise direction, wall-normal direction, and spanwise direction, respectively.

The temporal DNS approach[47] is performed for compressible turbulent boundary layers in this study. This approach is inspired by the temporal simulation of flows which are generally thought of as developing in space. The flow is the turbulent counterpart to the Stokes's first problem, in which a fluid at rest is set into a turbulent motion by a wall moving at constant velocity U_W. Figure 2.2 (a) is the spatially developing boundary

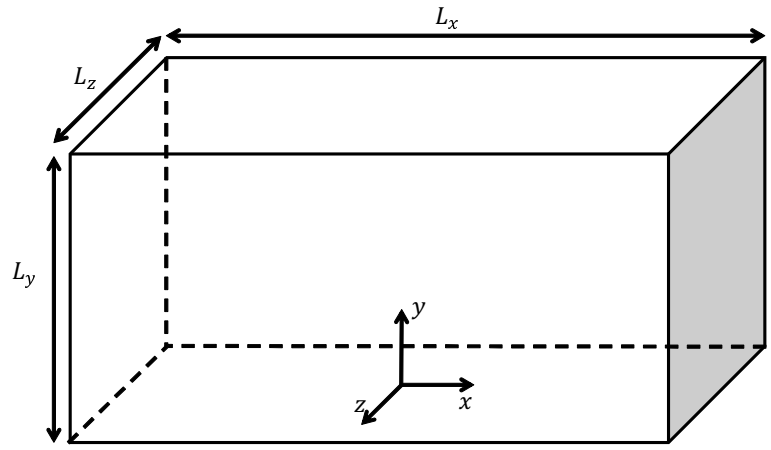

Figure 2.1 Computational domain.

layer, which grows with the streamwise direction x. In contrast, the proposed temporally developing boundary layer is developing with time t by applying periodic condition in the streamwise and spanwise direction as shown in figure 2.2 (b), which shows instances at two different time in a temporal developing boundary layer. Here δ is the boundary layer thickness, which is defined as the value of y where the streamwise mean velocity reduce to 1% of the wall velocity U_W.[52]

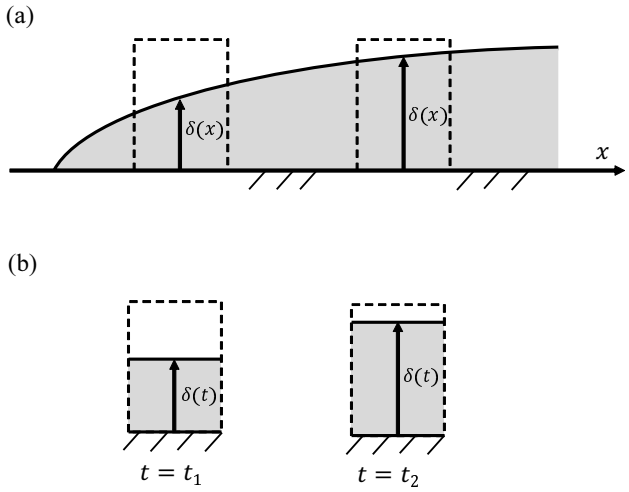

Figure 2.2 (a) Spatially developing boundary layer. (b) Temporally developing boundary layer.

2.3 Initial conditions boundary conditions

2.3.1 Initial conditions

In DNS studies, proper initial conditions are crucial for replicating the physical phenomenon. The initial conditions in present simulations are similar to the ones introduced by Kozul et al.,[48] where incompressible boundary layers are studied with temporal DNSs.

The initial velocity profile approximates the velocity induced by a trip wire with a diameter D installed on the moving wall with velocity U_W.[53] The trip wire is often used in wind tunnel experiments to promote the transition from laminar to turbulence.[54] Here, the subscript 'W' refers to the properties on the wall. The initial mean streamwise velocity profile $\overline{u}_0$ is a function of y as shown in figure 2.3, where $\overline{u}_0$ is equal to the wall velocity U_W at $y = 0$ and decreases toward 0 as y increase. The total velocity field consists of a mean velocity and fluctuating components. On another hand, the mean spanwise velocity $\overline{v}_0$ and mean wall-normal direction velocity $\overline{w}_0$ are zero. Specifically, the initial velocity components in the three directions, u_0, v_0, w_0, are written as:[48]

$$u_0 = \overline{u}_0(y) + u_0'(x, y, z); \quad v_0 = v_0'(x, y, z); \quad w_0 = w_0'(x, y, z). \tag{2.8}$$

Here, the subscript '0' refers to an initial value. The overbar denotes the averaged value, where the spatial averaging procedure is applied in the homogeneous (x and z) directions, the subscript $'$ refers to the fluctuation component. The initial mean streamwise velocity $\overline{u}_0$ is represents as:

$$\overline{u}_0(y) = \frac{U_W}{2} + \frac{U_W}{2} \tanh\left[\frac{D}{2\theta_{sl}}\left(1 - \frac{y}{D}\right)\right], \tag{2.9}$$

where $\theta_{sl} = 0.01D$ is the initial shear layer momentum thickness, and $\theta_{sl} = 0.01D$ is used in this study. Here, the trip wire diameter D is determined by trip wire Reynolds number $Re_D \equiv U_W D/\nu$, where $\nu = \mu/\rho$ is the kinematic viscosity. Kozul et la[53] showed that $Re_D = 500$ is the critical value for turbulent transition: if Re_D is smaller than 500, turbulent transition will not occur. $Re_D = 2000$ is used in present study so that the turbulent transition can occur. The step-function-like shape of the tanh profile also means that the trip wire diameter can be identified with the initial boundary layer displacement thickness.[53] For triggering turbulent transition, the velocity fluctuations with the root-mean square (RMS) value $0.05U_W$ is added to all the velocity components in the near-wall region of $y < D$. The velocity fluctuations used in this study are generated by a diffusion process, which converts the random noise into fluctuations that possess the required length scales in turbulence (see Kempf[55] for details). Initial temperature and pressure is uniform in whole computational domain: $T_0 = 300$ K, $P_0 = 101.3$ kPa.

For the scalar field, the initial condition is given by a scalar profile similar with the

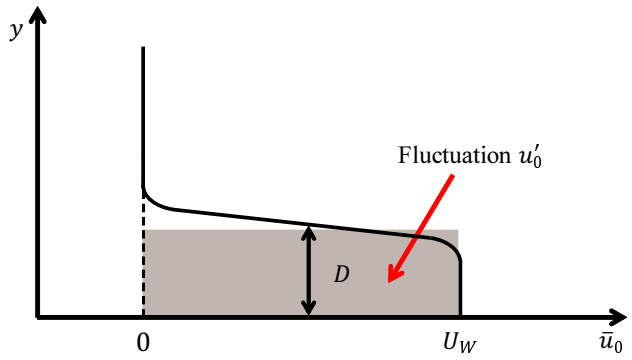

Figure 2.3 Initial streamwise velocity profile.

initial mean streamwise velocity without any scalar fluctuations:

$$\phi_0(y) = \frac{\phi_W}{2} + \frac{\phi_W}{2}\tanh\left[\frac{D}{2\theta_{sl}}(1-\frac{y}{D})\right], \tag{2.10}$$

where, $\phi_W = 1$ is the passive scalar at the wall. The distribution of passive scalar indicates that the passive scale is injected from the wall and full of the near wall region of $y \leq D$, where trip wire exists, in the initial condition.

2.3.2 Boundary conditions

In addition to the initial conditions, proper boundary conditions are also necessary for replicating flows in a computational domain. In this study, the periodic boundary conditions are applied in streamwise (x) and spanwise (z) directions. In the wall-normal direction (y), the no-slip adiabatic condition is applied on the wall ($y = 0$), for which the velocity and passive scalar on the wall are given by:

$$u = U_W; \quad v = 0; \quad w = 0; \quad \phi = 1. \tag{2.11}$$

According to the adiabatic condition, the temperature and density scalar gradients in the wall-normal direction are zero on the wall:

$$\left(\frac{\partial T}{\partial y}\right)_W = 0, \tag{2.12}$$

$$\left(\frac{\partial \rho}{\partial y}\right)_W = 0. \tag{2.13}$$

The pressure P can be calculated by equation (2.5).

For the boundary condition in the top of computational domain ($y = L_y$), the non-reflective outflow boundary conditions of Navier-Stokes Characteristics Boundary Conditions (NSCBC) is used with a sponge layer.[56] In high-speed flows, turbulence can generate and radiate waves which can reach the boundaries of computational domain. If the boundary conditions are not appropriate, the waves can be reflected when they reach the boundaries of computational domain (the top boundary in the present DNS) and thereby affect and distort the interior flow. To prevent the spurious wave reflections on the boundary, Poinsot and Lele[57] developed NSCBC based on the Euler equations, then Lodato et al.[56] modified it so that the convection and pressure gradient in boundary are also considered. However, this modified NSCBC can only be proved to perform well when flow vertically passes through the boundary. The NSCBC used in present study is further modified by Wang et al.[58] where the contribution of transverse terms to waves is also taken into consideration, and this NSCBC is called 3D-NSCBC. The governing equations at the boundary normal direction x_1, which can be x, y, z arbitrarily in theory and it is y in present study, are expressed though the wave analysis by truncating all the viscous terms:

$$\frac{\partial \rho}{\partial t} + \frac{1}{c^2}\left[\zeta_2 + \frac{1}{2}(\zeta_5 + \zeta_1)\right] - \psi_1 = 0, \tag{2.14}$$

$$\frac{\partial u_1}{\partial t} + \frac{1}{2\rho c}(\zeta_5 - \zeta_1) - \psi_2 = 0, \tag{2.15}$$

$$\frac{\partial u_2}{\partial t} + \zeta_3 - \psi_3 = 0, \tag{2.16}$$

$$\frac{\partial u_3}{\partial t} + \zeta_4 - \psi_4 = 0, \tag{2.17}$$

$$\frac{\partial T}{\partial t} + \frac{T}{\rho c^2}\left[-\zeta_2 + \frac{\gamma - 1}{2}(\zeta_5 + \zeta_1)\right] - \psi_5 = 0, \tag{2.18}$$

$$\frac{\partial \phi}{\partial t} + \zeta_6 - \psi_6 = 0, \tag{2.19}$$

where ζ_i is the magnitude of the waves that go through the boundary, and ψ_i is the transverse contribution (x_2 and x_3 directions) in the boundary plane. Each of these waves has one characteristic velocity which is donated as λ_i. Moreover, λ_1 is the velocity of sound wave traveling in negative x_1 and λ_5 is positive one in terms of quantification for x_1 direction. λ_2 is the convection velocity of the entropy wave; λ_3 and λ_4 are the advection velocities of u_2 and u_3 in x_1 axis. Finally, λ_6 refers to the advection velocity of the other scalar, e.g., species mass. They can be summarized as:

$$\lambda_1 = u_1 - c, \tag{2.20}$$

$$\lambda_2 = \lambda_3 = \lambda_4 = \lambda_6 = u_1, \tag{2.21}$$

$$\lambda_5 = u_1 + c, \tag{2.22}$$

where c is the speed of sound wave. The expressions of ζ_i and ψ_i are given by:

$$\zeta = \begin{pmatrix} \lambda_1\left(\frac{c^2}{\gamma}\frac{\partial \rho}{\partial x_1} + \frac{\rho c^2}{\gamma T}\frac{\partial T}{\partial x_1} - \rho c\frac{\partial u_1}{\partial x_1}\right) \\ \lambda_2\left(\frac{c^2(\gamma-1)}{\gamma}\frac{\partial \rho}{\partial x_1} - \frac{\rho c^2}{\gamma T}\frac{\partial T}{\partial x_1}\right) \\ \lambda_3\frac{\partial u_2}{\partial x_1} \\ \lambda_4\frac{\partial u_3}{\partial x_1} \\ \lambda_5\left(\frac{c^2}{\gamma}\frac{\partial \rho}{\partial x_1} + \frac{\rho c^2}{\gamma T}\frac{\partial T}{\partial x_1} - \rho c\frac{\partial u_1}{\partial x_1}\right) \\ \lambda_6\frac{\partial \phi}{\partial x_1} \end{pmatrix}, \tag{2.23}$$

$$\psi = \begin{pmatrix} -\frac{\partial m_k}{\partial x_k} \\ -u_k\frac{\partial u_k}{\partial x_k} \\ -u_k\frac{\partial u_2}{\partial x_k} - \frac{c^2}{\gamma T}\frac{\partial T}{\partial x_2} - \frac{c^2}{\gamma \rho}\frac{\partial \rho}{\partial x_2} \\ -u_k\frac{\partial u_3}{\partial x_k} - \frac{c^2}{\gamma T}\frac{\partial T}{\partial x_3} - \frac{c^2}{\gamma \rho}\frac{\partial \rho}{\partial x_3} \\ -u_k\frac{\partial T}{\partial x_k} - T(\gamma-1)\frac{\partial u_k}{\partial x_k} \\ -u_k\frac{\partial \phi}{\partial x_k} \end{pmatrix} (k = 2, 3) \quad \text{(no summation)}. \tag{2.24}$$

Here, $k = 2, 3$ indicate the directions in transverse plane of boundary.

Sponge layers[59] are set for the boundary where the artificial boundary conditions are used. The fluctuations induced by waves are damped before the wave reach the boundary. The sponge layer is set at $L_y - 10D < y < L_y$, where is just under the NSCBC. In the same way as for pressure and density at the radiation boundaries, the mean flow variables in the sponge zone are also adjusted so that they match the classical laws observed in turbulent boundary layers. The sponge layer in the present DNS is formed by combining the coarse grid stretched in the boundary normal direction and Laplacian low-pass filtering applied to ρ, ρu_i, ρT, and $\rho\phi$ at the end of every computational time step. The mathematical algorithm for the sponge layer is shown below.

In x direction:

$$fx_{i,j,k} = (1 - A_{sp}(j))f_{i,j,k} + A_{sp}(j)\left(\frac{f_{i+1,j,k}}{4} + \frac{f_{i,j,k}}{2} + \frac{f_{i-1,j,k}}{4}\right). \tag{2.25}$$

In z direction:

$$fz_{i,j,k} = (1 - A_{sp}(j))fx_{i,j,k} + A_{sp}(j)\left(\frac{fx_{i,j,k+1}}{4} + \frac{fx_{i,j,k}}{2} + \frac{fx_{i,j,k-1}}{4}\right). \tag{2.26}$$

In y direction:

$$g_{i,j,k} = \begin{cases} (1 - A_{sp}(j))fz_{i,j,k} + A_{sp}(j)\left(\dfrac{fz_{i,j+1,k}}{4} + \dfrac{fz_{i,j,k}}{2} + \dfrac{fz_{i,j-1,k}}{4}\right), & (2 \le j \le N_y - 1) \\ (1 - A_{sp}(j))fz_{i,j,k} + A_{sp}(j)\left(\dfrac{fz_{i,j,k}}{2} + \dfrac{fz_{i,j-1,k}}{2}\right). & (j = N_y) \end{cases} \tag{2.27}$$

Here, $f_{i,j,k}$ represents the quantity at the point (i, j, k) before applying the low-pass filter and $g_{i,j,k}$ is the value after the filter is applied. The strength of the filter is determined by the coefficient A_{sp}, which gets larger as it gets closer to the boundary. A_{sp} is defined using following equation so that it is 0 in the beginning of sponge layer and reaches 1 at the boundary:

$$A_{sp}(j) = \frac{1}{2}\left[1 + \tanh\left(B_{sp}\frac{y - (L_y/2 - 10D)}{10D} - C_{sp}\right)\right]. \tag{2.28}$$

Here, $B_{sp} = 7$ and $C_{sp} = 0.5$ are constants (See Bogey (2009)[59] for more details).

2.4 Numerical schemes

The present DNS code is based on the fully explicit numerical schemes proposed in Wang et al.[58]

2.4.1 Spatial discretization

Spatial discretization used in this study is based on the fully explicit finite difference schemes used in Wang et al.[58] The explicit 8th-order center-difference scheme is used in interior nodes, where first-order derivatives at a node i is given by:

$$\frac{\partial f_i}{\partial x_i} = \frac{4(f_{i+1} - f_{i-1})}{5\Delta x_i} - \frac{(f_{i+2} - f_{i-2})}{5\Delta x_i} - \frac{4(f_{i+3} - f_{i-3})}{105\Delta x_i} - \frac{(f_{i+4} - f_{i-4})}{280\Delta x_i}, \tag{2.29}$$

where x_i can be the grid spacing x, y, and z in the x, y, and z directions respectively. It is important to note that the spatial difference near the computational boundaries in y directions should be particularly treated with internal-biased lower-order finite difference schemes for stability:

$$\frac{\partial f_1}{\partial y} = \frac{1}{6\Delta y_1}(-11f_1 + 18f_2 - 9f_3 + 2f_4), \tag{2.30}$$

$$\frac{\partial f_2}{\partial y} = \frac{1}{6\Delta y_2}(-2f_1 - 3f_2 + 6f_3 - f_4), \tag{2.31}$$

$$\frac{\partial f_3}{\partial y} = \frac{1}{12\Delta y_3}(f_1 - 8f_2 + 8f_4 - f_5), \tag{2.32}$$

$$\frac{\partial f_4}{\partial y} = \frac{1}{60\Delta y_4}(-f_1 + 9f_2 - 45f_3 + 45f_5 - 9f_6 + f_7). \tag{2.33}$$

Here, subscript $i = 1, 2...7$ refers to the node which is $i - 1$ apart from the boundary. Namely, $\frac{\partial f_1}{\partial y}$ is derivative on the node of the boundaries, $\frac{\partial f_2}{\partial y}$ is derivative on the next node apart from boundaries, similarly for $\frac{\partial f_3}{\partial y}$ and $\frac{\partial f_4}{\partial y}$. As shown in above equations, $\frac{\partial f_1}{\partial y}$, $\frac{\partial f_2}{\partial y}$, $\frac{\partial f_3}{\partial y}$, and $\frac{\partial f_3}{\partial y}$, are the third-order, third-order, forth-order, and sixth-order of internal-biased finite differences, respectively. Similarly, for the second-order derivatives, they are computed by the above formulations by replacing f_i by the first-order derivatives $\frac{\partial f_i}{\partial x_i}$. The convective terms in the governing equations are calculated in the cubic skew-symmetric form:[60]

$$\frac{\partial(\rho f u_j)}{\partial x_j} = \frac{1}{2}\frac{\partial(\rho f u_j)}{\partial x_j} + \frac{1}{2}\left[f u_j \frac{\partial \rho}{\partial x_j} + \rho u_j \frac{\partial f}{\partial x_j} + \rho f \frac{\partial u_j}{\partial x_j}\right], \tag{2.34}$$

where f in the above equation is 1, u_i, T, and ϕ for the governing equation of mass, momentum, energy, and passive scalar (equations (2.1) - (2.4)), respectively. This form reduces aliasing error caused by the finite difference schemes in convective terms (see[61] for details).

2.4.2 Time integration

The time integration of the governing equations (2.1) - (2.4) is also based on the fully explicit schemes in the present DNS code. The Euler terms and other terms including viscous stress, conductive diffusion, and molecular diffusion are handled by different numerical schemes. The Euler terms that contain convective and pressure terms are treated with the explicit five-stage fourth-order Runge-Kutta method written as:

$$df_m = A_m df_{m-1} + \Delta t \cdot df_{m-1}, \tag{2.35}$$

$$f_m = f_{m-1} + B_m df_m, \tag{2.36}$$

where $m = 1, ..., 5$ represents the m-th stage of the Runge-Kutta method, df represents the corresponding convective and pressure terms in the governing equations of the variable f:

$$f = \rho, \qquad df = -\frac{\partial \rho u_j}{\partial x_j}, \tag{2.37}$$

$$f = \rho u_i, \qquad df = -\frac{\partial \rho u_i u_j}{\partial x_j} - \frac{\partial P}{\partial x_i}, \tag{2.38}$$

$$f = \rho T, \qquad df = -\frac{\partial \rho T u_j}{\partial x_j} - (\gamma - 1) P \frac{\partial u_j}{\partial x_j}, \tag{2.39}$$

$$f = \rho \phi, \qquad df = -\frac{\partial \rho u_j \phi}{\partial x_j}. \tag{2.40}$$

Δt is the time step interval, which is determined by the Courant Friedrichs Lewy (CFL) condition, and CFL = 0.8 is used in all simulations in this thesis. The coefficients A_j and B_j as displayed in table 2.1, are carefully considered for both numerical errors and computational stability. Carpenter[62] proved that this five-stage fourth-order Runge-Kutta can save computational storage and ensure stability compared to the traditional fourth-order Runge-Kutta scheme.

The time integration with the Runge-Kutta method is followed by the explicit 1st-order Euler scheme applied to remaining terms, which involves viscous diffusion, thermal conduction, and scalar diffusion. The scheme can be written as:

$$f = f_5 + \Delta t \cdot d_2 f, \tag{2.41}$$

where f_5 is the result by computing five step Runge-Kutta. $d_2 f$ here is the remaining terms in the governing equations (2.3)-(2.4), which are viscous diffusion, thermal conduction, and scalar diffusion terms.

Table 2.1 Coefficients used in five-stage fourth-order Runge-Kutta scheme

A_1	A_2	A_3	A_4	A_5
0	$-\frac{73838075589}{153778244506}$	$-\frac{6194124222391}{4410992767914}$	$-\frac{875753879689}{434298951106}$	$-\frac{375951423649}{355864889808}$
B_1	B_2	B_3	B_4	B_5
$\frac{69922298306}{679754813293}$	$-\frac{151102391305}{203957027379}$	$-\frac{168159696081}{226431017777}$	$-\frac{189406283338}{403426599621}$	$-\frac{184809359603}{982122979183}$

2.4.3 Low-pass filtering

For removing the spurious fluctuations induced by the finite difference schemes, the following 10th-order low-pass filter[60] is applied to the whole computational domain at each time step:

$$\begin{aligned}\hat{f}_i \quad = \quad & f_i + 2^{-10}[252f_i - 210(f_{i+1} + f_{i-1}) + 120(f_{i+2} + f_{i-2})] \\ & + 2^{-10}[-45(f_{i+3} + f_{i-3}) + 10(f_{i+4} + f_{i-4}) - (f_{i+5} + f_{i-5})],\end{aligned} \tag{2.42}$$

where $\hat{f}$ in the above equations is quantity filtered by low-pass filter. The nodes near the computational boundaries (except periodic boundaries) are particularly treated as:

$$\begin{aligned}\hat{f}_1 =& f_1 + 2^{-10}(f_1 - 5f_2 + 10f_3 - 10f_4 + 5f_5 - f_6), \\ \hat{f}_2 =& f_2 + 2^{-10}(-5f_1 + 26f_2 - 55f_3 + 60f_4 - 35f_5 + 10f_6 - f_7), \\ \hat{f}_3 =& f_3 + 2^{-10}(10f_1 - 55f_2 + 126f_3 - 155f_4 + 110f_5 - 45f_6 + 10f_7 - f_8), \\ \hat{f}_4 =& f_4 + 2^{-10}(-10f_1 + 60f_2 - 155f_3 + 226f_4 - 205f_5 + 120f_6 - 45f_7 + 10f_8 - f_9), \\ \hat{f}_5 =& f_5 + 2^{-10}(5f_1 - 35f_2 + 110f_3 - 205f_4 + 251f_5 - 210f_6 + 120f_7 - 45f_8 + 10f_9 - f_{10}),\end{aligned} \tag{2.43}$$

whose orders are fifth-order, sixth-order, seventh-order, eighth-order, and ninth-order, respectively.

2.5 Computational conditions and girds

The DNSs are performed with two different Mach numbers $M = 0.8$ and 1.6 defined as $M = U_W/c_0$, which correspond to subsonic and supersonic boundary layers. Here, $c_0 = \sqrt{\gamma R T_0}$ is the sound speed in the initial time. As described in section 2.3, the trip wire Reynolds number $Re_D = 2000$ is used for both M.

The wall shear stress τ_W is given by

$$\tau_W \equiv \rho_W \nu_W \left(\frac{d\overline{u}}{dy} \right)_W , \tag{2.44}$$

which is entirely contributed by the viscous stress on the wall. It is important to note that the viscous stress is dominant in the near-wall region, and thus the viscosity ν_W and τ_W are important parameters in the near-wall region. From these quantities ν_W, τ_W, and ρ_W, viscous scales[52] are defined for the near-wall region: the friction velocity u_τ is the viscous velocity scale and δ_ν is the viscous length scale, which are respectively defined as:

$$u_\tau \equiv \sqrt{\frac{\tau_W}{\rho_W}}, \tag{2.45}$$

$$\delta_\nu \equiv \nu_W / u_\tau. \tag{2.46}$$

The viscous length scale δ_ν is used to set grid spacing according to previous numerical studies of boundary layers.[46] The superscript '+' refers to the quantity nondimensionalized by the viscous scales. For example, $\Delta x^+ = \Delta x/\delta_\nu$.

Large computational domain (L_x, L_y, L_z) enough to contain a large number of large-scale flow structures is of great importance for DNS. Therefore, (L_x, L_y, L_z) in the present DNS is determined based on the length of large-scale motion in a boundary layer, namely boundary layer thickness δ. The size of the computational domain is set following Kozul et al.,[48] the wall-parallel domain size is $L_x \approx 6\delta$ in the mean flow direction and $L_z \approx 3\delta$ in the spanwise direction, the wall-normal domain size is set as $L_y \approx 3\delta + 10D$, where $10D$ is the thickness of the sponge layer.

The Cartesian mesh is used in this study, where the grid spacing is uniform in the streamwise x and spanwise z directions, while the wall-normal grid spacing obeys a half-tanh mapping:

$$y(j) = L_y(1 - \tanh(\alpha_y(1 - \frac{j}{N_y - 1}))/\tanh \alpha_y). \tag{2.47}$$

Here, $j = 1, 2..., N_y$ is the grid point number in y direction apart from the wall, α_y is a factor used to adjust the grid spacing in the function, and $\alpha_y = 2.9$ is used in present study. This function gives a finer grid near the wall and a coarser grid away from the wall by stretching the grid as y increases. Small enough grid spacing is required to resolve the smallest eddies, especially in the near-wall region. Furthermore, the resolution near the TNTI should also be carefully examined for TNTI studies, where the DNS must resolve

Table 2.2 Computational and grid parameters

Case	F001	F002	C001	C002
M	0.8	1.6	0.8	1.6
Re_D	2000	2000	2000	2000
Re_θ	2206	2174	2315	2540
Re_τ	639	524	707	584
$L_x/D, L_y/D, L_z/D$	$54, 46, 27$	$54, 46, 27$	$66, 54, 33$	$66, 54, 33$
$L_x/\delta, L_y/\delta, L_z/\delta$	$6.30, 5.37, 3.15$	$7.23, 5.29, 3.62$	$5.74, 4.89, 2.87$	$6.17, 5.05, 3.08$
$\Delta x^+, \Delta y_W^+, \Delta z^+$	$4.9, 0.188, 4.6$	$4.9, 0.180, 4.6$	$9.49, 0.188, 4.75$	$8.36, 0.180, 4.70$
N_x, N_y, N_z	$972, 738, 486$	$972, 772, 512$	$486, 628, 486$	$576, 648, 512$

the smallest scale of turbulence that appears underneath the TNTI, i.e., Kolmogorov scale $\eta = (\overline{\nu}^3/\overline{\varepsilon})^{1/4}$ in the turbulent region. Here, $\varepsilon = \tau_{ij}S_{ij}$ is the kinetic energy dissipation rate, and $S_{ij} = (\partial u_i/\partial x_j + \partial u_j/\partial x_i)/2$ is the rate of strain tensor. For investigating the influences of the DNS resolution near the TNTI, DNSs with two different types of mesh setting for each value of the Mach number are performed in this study as summarized in table 2.2. The DNS with computational grid sizes similar to the work by Kozul et al.[48] is referred to group C (cases C001 and C002 for $M = 0.8$ and 1.6, respectively). In group C, the grid spacing, $(\Delta x, \Delta y, \Delta z)$, is determined based on the smallest length scale near the wall δ_ν. The numbers of the grid points, N_x and N_z, are determined so that $\Delta x^+ < 9.7$ and $\Delta z^+ < 4.8$ are satisfied in the streamwise and spanwise directions. To ensure fine resolution in the normal-wall direction, $\Delta y_1^+ < 0.2$ should be hold during the simulation.[63] More details regarding the setting of the domain size and grid spacing can be found in Moser and Mansour.[63]

The simulations in group F (cases F001 and F002 for $M = 0.8$ and 1.6, respectively) are performed with finer meshes than group C. The number of the grid points in group F is determined not only based on the length of the near-wall region δ_ν but also based on the Kolmogorov scale η_c in the turbulent core region away from the wall ($y = 0.5\delta$), where subscript c represent a value in the turbulent core region ($y = 0.5\delta$). The difference in the resolution between groups C and F are discussed in relation to the TNTI in section 4. In group F, $\Delta x \approx 1.5\eta_c$, $\Delta y_\delta \approx 1.5\eta_c$, and $\Delta z \approx 1.5\eta_c$ are ensured. Here, Δy_δ is the Δy at $y = \delta$. Thereby, the number of the grid points (N_x, N_y, N_z) is determined from the required resolutions and computational domain size.

Finally, the computational parameters and normalized grid size in the DNS of temporally developing boundary layers are summarized in table 2.2. The DNS in present study is designed for studying the TBL at $Re_\theta \approx 2000$. The TBLs reach this target

Reynolds number ($Re_\theta \approx 2000$) in the end of temporal simulation. The above conditions for computational domain size lead to $(L_x, L_y, L_z) = (54D, 46D, 27D)$ for $M = 0.8$ and $(L_x, L_y, L_z) = (66D, 54D, 33D)$ for $M = 1.6$. The definitions of momentum displacement thickness Reynolds number Re_θ and friction Reynolds number Re_τ can be written as:

$$Re_\theta = U_W \theta / \nu_0, \tag{2.48}$$

$$Re_\tau = u_\tau \delta / \nu_W = \delta / \delta_\nu. \tag{2.49}$$

Here, θ is momentum displacement thickness defined as $\theta = \int_0^\infty (\overline{\rho u}/\rho_0 U_W)(1-(\overline{u}/U_W))dy$.

Chapter 3

Development of temporally developing boundary layers

Fundamental characteristics of DNS data for temporally developing boundary layers are shown in this chapter, including the comparison with experimental data, spatial DNS data and theoretical laws.

3.1 Temporal development of turbulent boundary layers

The development of the turbulent boundary layers can be tracked by the transport of ϕ, which takes $\phi_W = 1$ on the wall and $\phi_\infty = 0$ in the free-stream. Here, ∞ refers to the properties of free-stream flow. Figure 3.1 shows the snapshots of ϕ at different time throughout the simulation for case F001 ($M = 1.6$), which offer a view of the boundary layer development process in the temporal DNS. It can be seen that the boundary layer develops from a laminar flow and reaches the fully developed turbulent state as in figure 3.1 (d). The well-known structures of the boundary layers can be found in this visualization, such as large-scale eddy motions,[64] engulfment process.[25] The passive scalar ϕ can be considered as the marker of turbulent region,[65] where $\phi > 0$. It can also be seen that the non-turbulent region with $\phi = 0$ always coexists with the turbulent region with $\phi > 0$ in the outer region of the turbulent boundary layer.

In comparison of how the skin friction coefficient C_f varies with Reynolds number Re_{theta} at different Mach numbers M, it is necessary to utilize suitable transformations to C_f and the Re_θ, where C_f is defined as $C_f = 2\tau_W/(\overline{\rho}_W U_W^2)$. Hopkins and Inouye (1971)[66] introduced a way based on Driest II transformation[67] for reducing the 'compressible' friction coefficient and Reynolds number to 'incompressible' value for the adiabatic wall state. The transformed 'incompressible' values are denoted with the subscript 'i', and the

transformations are written as:

$$C_{f.i} = F_c C_f, Re_{\theta.i} = \frac{\mu_0}{\overline{\mu}_W} Re_\theta, \tag{3.1}$$

$$F_c = \frac{\overline{T}_W/T_0 - 1}{\arcsin^2 \alpha}, \quad \alpha = \frac{\overline{T}_W/T_0 - 1}{\sqrt{\overline{T}_W/T_0(\overline{T}_W/T_0 - 1)}}. \tag{3.2}$$

The transformed skin friction for the present DNSs is compared in figure 3.2 with a widely used friction law:[68]

$$C_{f.i} = 0.024 Re_{\theta.i}^{-1/4}. \tag{3.3}$$

It is important to note that Re_θ increases with time t because of the boundary layer temporal development. The skin frictions obtained from the present DNSs are in better agreements with the friction law with increasing of Re_θ. It implies that the boundary layers undergo the transition from the laminar state to the fully-development turbulent state.

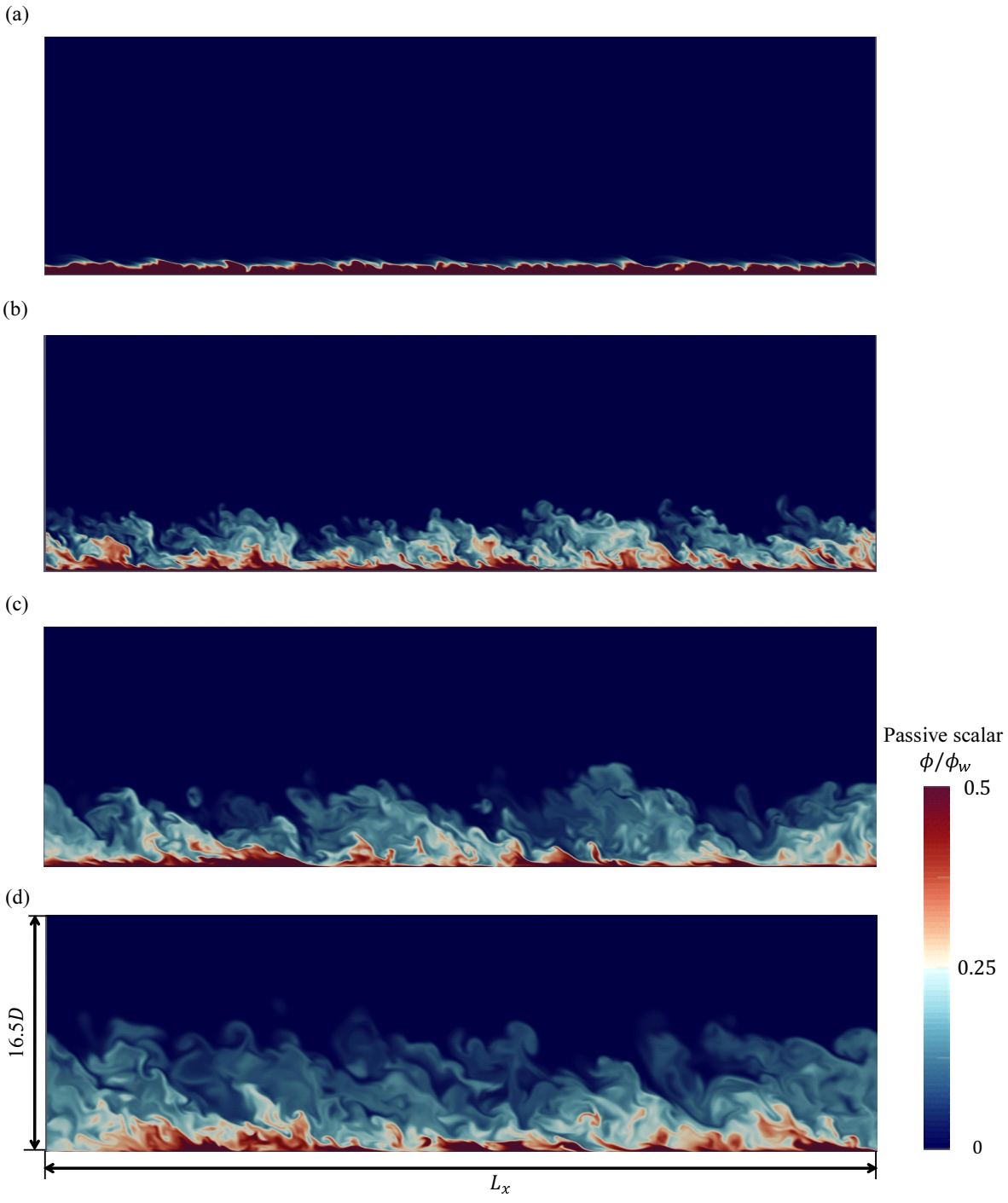

Figure 3.1 Visualization of temporally developing boundary layer with passive scalar ϕ for case F001 ($M = 1.6$). The wall is moving in the x direction (from left to right). (a) $tU_W/D = 8.2, Re_\theta = 278, Re_\tau = 6$. (b) $tU_W/D = 54.1, Re_\theta = 1336, Re_\tau = 327$. (c) $tU_W/D = 136.5, Re_\theta = 1764, Re_\tau = 495$. (d) $tU_W/D = 260.1, Re_\theta = 2152, Re_\tau = 622$.

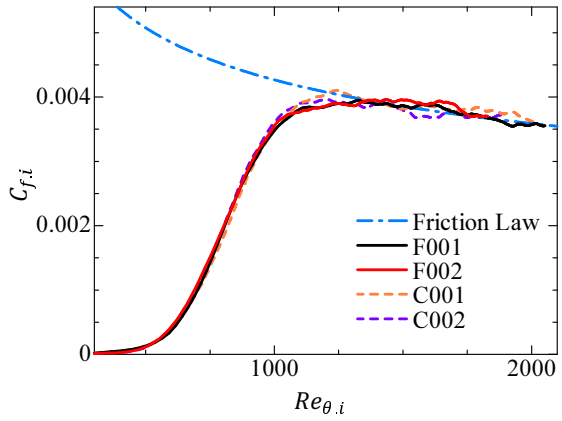

Figure 3.2 Variation of skin friction coefficient $C_{f,i}$ versus Reynolds number $Re_{\theta,i}$ calculated with the transformation introduced by Hopkins and Inouye (1971).[66] The present DNS results are compared with the friction law given by equation (3.3).

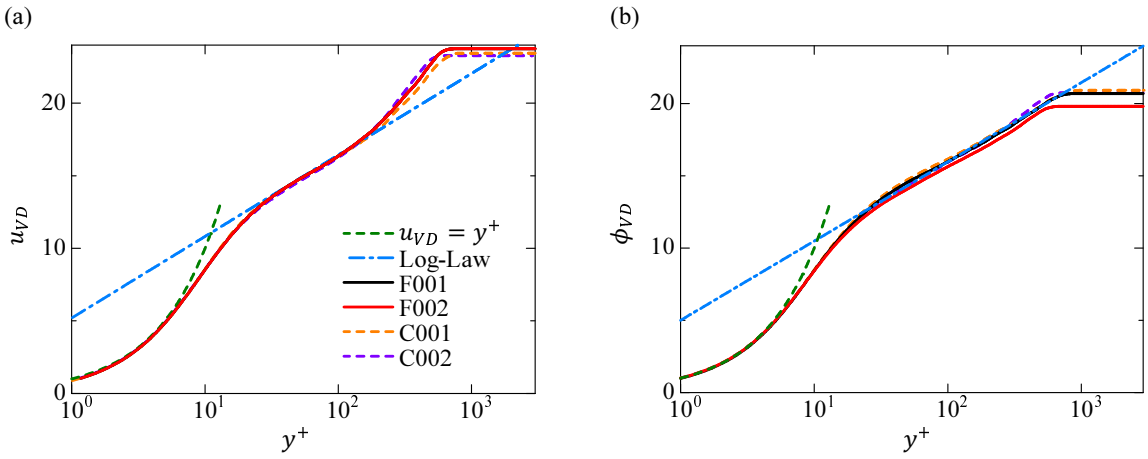

Figure 3.3 The mean profiles of Van Direst transformed (a) streamwise velocity and (b) passive scalar. Here, curve for log-law[52] represents as $u_{VD} = (1/k)\ln y^+ + A$ with the constants $k = 0.41$ and $A = 5.1$.

3.2 Mean velocity and velocity fluctuation

The Mach number effects on the velocity statistics are well taken into account in the Van Driest transformation, by which the mean streamwise velocity can be compared among different Mach numbers. The definitions of Van Direst transformed[69] mean streamwise velocity u_{VD} and normalized wall-normal distance y^+[52] are displayed as following:

$$u_{VD} = \int_0^{u^+} \sqrt{\frac{\overline{\rho}}{\rho_W}} du^+, \tag{3.4}$$

$$u^+ = (U_W - \overline{u})/u_\tau, \tag{3.5}$$

$$y^+ = y/\delta_\nu, \tag{3.6}$$

where u_τ is the friction velocity and δ_ν is the viscous length-scale shown in equation (2.46). Similarly, Van Driest transformed[69] mean passive scalar is:

$$\phi_{VD} = \int_0^{\phi^+} \sqrt{\frac{\overline{\rho}}{\overline{\rho}_W}} d\phi^+, \tag{3.7}$$

$$\phi^+(y) = [\phi_W - \overline{\phi}]/\phi_\tau, \tag{3.8}$$

with $\phi_\tau \equiv \overline{D}_{m.W}(-d\overline{\phi}/dy)_W/u_\tau$. The mean profiles of Van Direst transformed streamwise velocity[69] are plotted in figure 3.3 (a). The green dashed curve indicates $u_{VD} = y^+$ and blue dot-dashed curve indicates the log-law[52] represented as $u_{VD} = (1/k)\ln y^+ + A$. Table 3.1 describes the classification of these sublayers:[52] In the viscous sublayer ($u_{VD} =$

Table 3.1 Van Direst transformed streamwise velocity profile.

Viscous sublayer	$y^+ < 5$	Mean flow is dominant by viscous stress, $u_{VD} = y^+$
Buffer layer	$5 < y^+ \lesssim 35$	Between viscous sublayer and log-law region
Log-law region	$y^+ \gtrsim 35 \quad \& \quad y/\delta \ll 1$	The log-laws hold, $u_{VD} = (1/k)\ln y^+ + A$

y^+), the Reynolds shear stress is negligible compared to the viscous stress and the DNSs data agrees well with the green dashed line; In the log-law region, the viscous stress is ignored, the present DNSs data represents a good agreement with the log-law with the constants $k = 0.41$ and $A = 5.1$; The buffer layer is the region between the viscous sublayer and log-law region. Similarly, ϕ_{VD} follows $\phi_{VD} = y^+$ in the viscous sublayer ($y^+ < 5$), while the log-law $\phi_{VD} = (1/k)\ln y^+ + A$ is also valid in the log-law region as shown in figure 3.3 (b). This also confirms the accuracy of the present DNS code and the reliability of the Van Driest II transformation at different Mach numbers.

The second-order statistics are also compared with experimental data[70] and other DNS data[44] of incompressible boundary layers. As described in Morkovin's hypothesis (1962),[71] the turbulence time-scale and length-scale are not affected by compressibility, which mainly affects the density and the thermodynamic properties across the wall layer. Since DNS data of compressible boundary layers is usually validated by comparing with incompressible flows for a similar Re_θ, the following transformation of second-order statistics in the compressible boundary layers is required for the comparison:[45]

$$u^*_{rms} = \frac{\sqrt{\widetilde{u''u''}}}{u_\tau}\sqrt{\frac{\overline{\rho}}{\overline{\rho}_W}}; \quad v^*_{rms} = \frac{\sqrt{\widetilde{v''v''}}}{u_\tau}\sqrt{\frac{\overline{\rho}}{\overline{\rho}_W}}; \quad uv^* = \frac{\widetilde{u''v''}}{u_\tau^2}\frac{\overline{\rho}(y)}{\overline{\rho}_W}, \tag{3.9}$$

$$y^* = y/\delta^*_\nu; \quad \delta^*_\nu = \overline{\nu}/(u_\tau\sqrt{\overline{\rho}_W/\overline{\rho}}), \tag{3.10}$$

where $\widetilde{f}$ is a density-weighted average (Favre average):

$$\widetilde{f} = \overline{\rho f}/\overline{\rho}, \tag{3.11}$$

while a fluctuation from the Favre average is denoted by $f'' = f - \widetilde{f}$. The statistics taken from incompressible boundary layers are nondimensionalized by the viscous scales as following:

$$u^+_{rms} = \frac{\sqrt{\overline{u'u'}}}{u_\tau}; \quad v^+_{rms} = \frac{\sqrt{\overline{v'v'}}}{u_\tau}; \quad uv^+ = \frac{\overline{u'v'}}{u_\tau^2}, \tag{3.12}$$

$$y^+ = y/\delta_\nu. \tag{3.13}$$

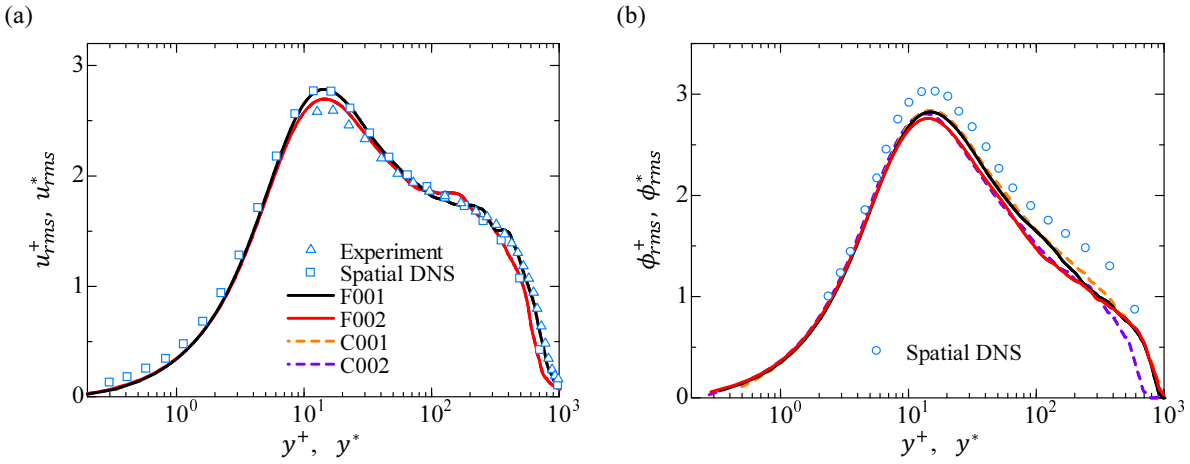

Figure 3.4 Second-order statistics, (a) RMS of streamwise velocity fluctuation compared with incompressible boundary layers studied in experiment at $Re_\theta = 2266$[70] and in spatial DNS at $Re_\theta = 1986$.[44] (b) RMS of passive scalar fluctuation compared with incompressible boundary layers studied in spatial DNS at $Re_\theta = 1986$.[72]

Similar transformations can be defined for ϕ by replacing u_i and u_τ by ϕ and ϕ_τ, respectively.

These second order statistics of velocity and passive scalar are compared with previous studies in figures 3.4 and 3.5. The present DNS agrees well with previous data from experiments[70] and DNS[44, 72] of spatially developing boundary layers for a comparable value of the Reynolds number Re_θ. These statistics of the present DNS compared with other studies show that the temporal DNS performed here accurately replicates the compressible turbulent boundary layers.

Although the high-speed TBLs are performed in present study, the one-order and second order statistics still can be compared with incompressible TBLs with some appropriate transformations. It is because the compressibility effects through the fluid properties agree with Morkovin's hypothesis,[71] which proposed that, "the essential dynamics of these shear flows will follow the incompressible pattern"[71] at moderate Mach number, namely $M \leq 5$.

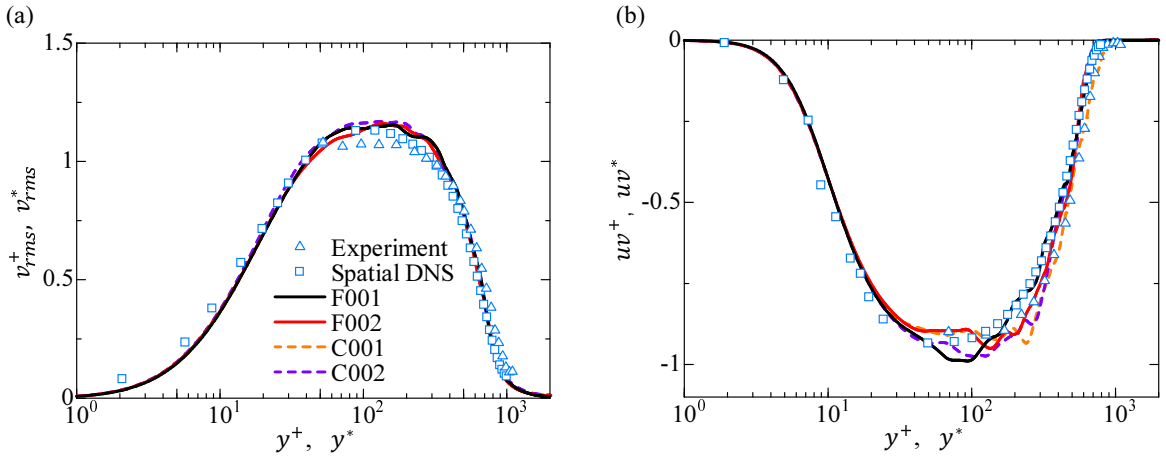

Figure 3.5 Second-order statistics, (a) RMS of wall-normal velocity fluctuation; (b) Reynolds stress. The present DNS results are compared with incompressible boundary layers studied in experiment at $Re_\theta = 2266$[70] and in spatial DNS at $Re_\theta = 1986$.[44]

3.3 Characteristics of the turbulent boundary layers

Other characteristics of the fully development turbulent boundary layers are presented in this subsection.

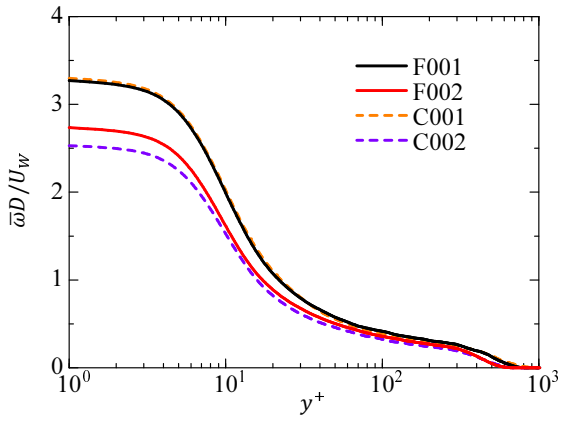

Figure 3.6 Vertical profile of mean vorticity magnitude.

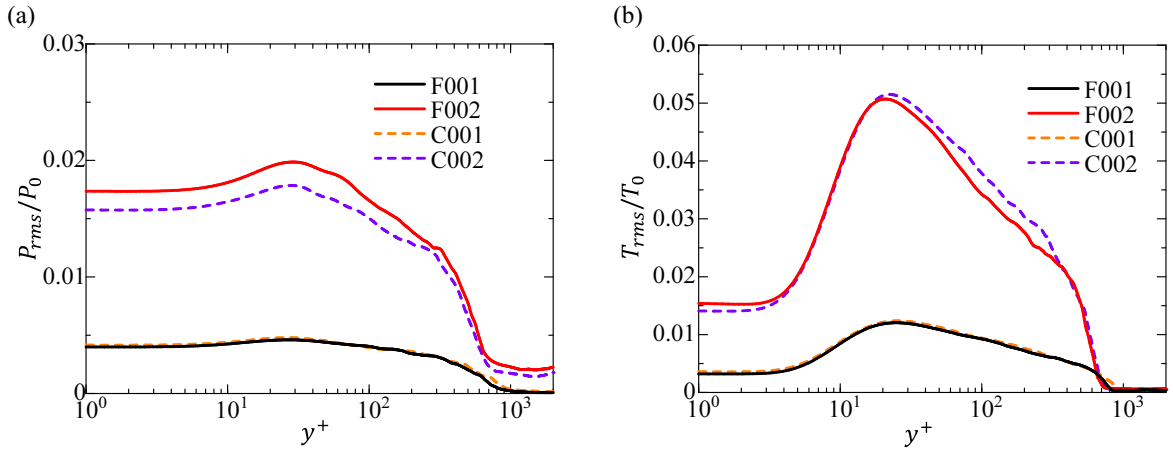

Figure 3.7 Vertical profiles of RMS of (a) pressure fluctuation, (b) temperature fluctuation.

The vertical profile of mean vorticity magnitude $\overline{\omega}$ are computed shown in figure 3.6. The vorticity in the near wall viscous sublayer ($y^+ < 5$) is very large, start to decrease

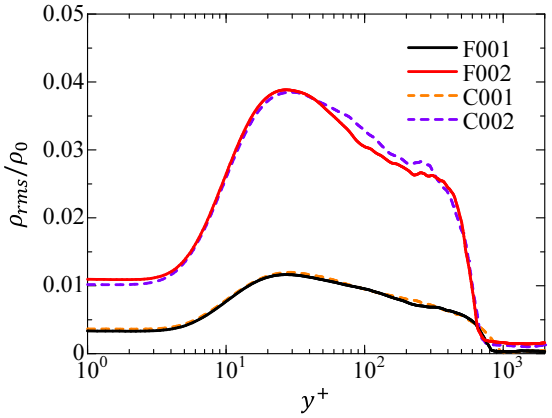

Figure 3.8 Vertical profiles of RMS of density.

in the buffer layer ($5 < y^+ < 35$) and gradually decreases in the log-law region ($y^+ > 35$ & $y/\delta << 1$), finally becomes almost zero at the height of the boundary layer thickness, where $y^+ = \delta^+ = \delta/\delta_\nu$. The RMS of pressure fluctuation and temperature fluctuation normalized by free-stream pressure and temperature P_0, T_0 are shown in figures 3.7 (a) and (b), respectively. RMS of density fluctuation is also plotted in figure 3.8. In all these three figures, it can be seen that all the peaks of the fluctuations are located in the buffer layer, and the fluctuations are much larger in $M = 1.6$ (Case F002 and C002) than in $M = 0.8$ (Case F001 and C001). This is because fluctuations in these thermodynamic properties are caused by compressibility effects, which become more significant for higher Mach numbers. In addition, some differences can be found for all these properties between group C and group F at Mach number $M = 1.6$.

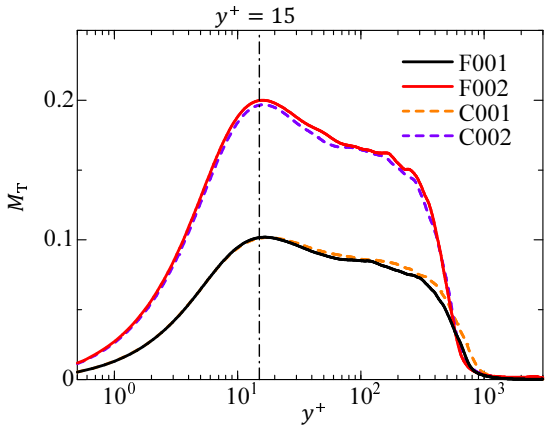

Figure 3.9 Turbulent Mach number.

The turbulent Mach number M_T is shown in figure 3.9, where M_T implying the degree of compressibility effects is defined as:

$$M_T = \frac{(\overline{u_i' u_i'})^{1/2}}{\overline{c}}, \tag{3.14}$$

where $c = \sqrt{\gamma RT}$ is the local sound speed. As shown in figure 3.9, M_T is large in the buffer layer and the log-law region, and the largest M_T is located in the buffer layer at $y^+ \approx 15$, which is the location with the peak of turbulence production. Since M_T is less than 0.3 throughout the boundary layers for $M = 0.8$ (Case F001 and C001) and 1.6 (Case F002 and C002), the compressibility is weak so that the compressibility does not change the turbulence behaviour significantly.[73] However, it should be noted that the compressibility effects do exist for the thermodynamics properties, e.g., temperature, pressure and density.

3.4 Summary

The skin friction, mean velocity, and rms velocity fluctuations in the compressible boundary layers are consistent with those in incompressible boundary layers when appropriate transformations are used. Excellent agreements can be found for first- and second-order statistics in present DNS with previous studies of theoretical law, experimental data, and data in spatial TBL for a comparable value of Re_θ. By the comparisons of first- and second-order statistics, the results show that the temporal DNS performed here accurately replicates the compressible TBLs for both groups F and C.

The compressibility effects do exist for the thermodynamics properties (e.g., temperature, pressure and density.) especially in the buffer layer, and it becomes more significant for higher Mach numbers. The peak of turbulence production is found to be located at the buffer layer. However, the turbulent Mach number M_T is less than 0.3 throughout the boundary layers even for $M = 1.6$ (cases F002 and C002), the compressibility is weak so that the compressibility does not change the turbulence structures significantly.

Chapter 4

Properties of the TNTI layer in compressible turbulent boundary layers

This chapter will describes the way of TNTI layer detection, then discusses the DNS spatial resolution and compressibility effects on the TNTI layer.

4.1 Detection of turbulent/non-turbulent interface

As in previous studies on the TNTI layer,[10,74] the outer edge of the TNTI layer , which is called irrotational boundary,[74] can be detected as an isosurface of vorticity magnitude $\omega = \omega_{th}$. Since the location of the isosurface of vorticity magnitude changes with the threshold ω_{th}, it is important to choose a reasonable value of ω_{th}. In this study, the vorticity threshold ω_{th} is selected by computing the volume fraction of the turbulent region ($\hat{V}_T$), which is a function of ω_{th}. Here, the volume fraction $\hat{V}_T$ is computed in the computational domain only without sponge layer. This approach is widely used for detecting turbulent and non-turbulent fluids in previous studies[10,28,74] including compressible flows,[38] and is also related to the method to obtain the threshold based on the probability density function of vorticity magnitude.[36] These two methods have been shown to yield a similar value of threshold.[36] The latter method has also been used in the detection of scalar interface in experiments.[75] A fluid with $\omega > \omega_{th}$ is referred to as a turbulent fluid while a non-turbulent fluid has $\omega < \omega_{th}$, then the corresponding turbulent volume V_T can be calculated. The normalized threshold applied for vorticity magnitude in TBL is displayed as below:

$$\omega_{th}^{*} = \frac{\omega_{th}}{(\delta^{+})^{-1/2} u_{\tau}^{2}/\overline{\nu}_{W}}, \tag{4.1}$$

where δ^{+} is the boundary layer thickness normalized by the viscous length scale, which is also equal to Re_{τ}. This scaling is linked to the TNTI interface because the TNTI layer appears around the vertical height of δ,[28,36] because mean vertical height of irrotational

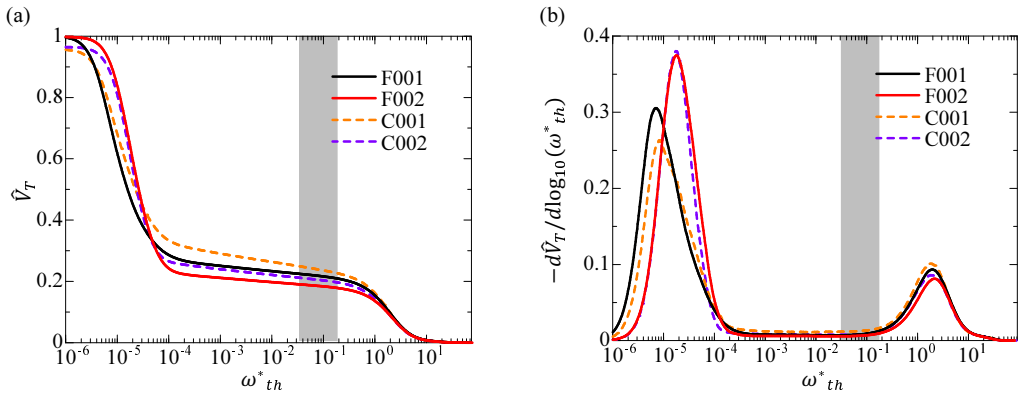

Figure 4.1 (a) Volume fractions of turbulent region $\hat{V}_T$ plotted against threshold ω^*_{th} used for detecting turbulent fluids. (b) First derivative of volume fraction $d\hat{V}_T/d\log(\omega^*_{th})$. The several values of vorticity magnitude in the range of gray shadow are used to examine the robustness of irrotational boundary detection in the subsection 4.2.

boundary is the order of boundary layer thickness $\langle y_{IB} \rangle \sim \delta$.[28] While the conventional scaling with the friction velocity $\omega^+ = \omega\nu/u_\tau^2$ is related to the near-wall region. Figure 4.1 (a) shows $\hat{V}_T = V_T/L_xL_yL_z$ as a function of the threshold ω^*_{th}. The turbulent volume largely increases for $\omega^*_{th} < 10^{-4}$ as ω^*_{th} decreases because of very small values of vorticity magnitude in the non-turbulent region. The derivatives of $\hat{V}_T$, $d\hat{V}_T/d\log(\omega^*_{th})$, are also calculated as a function of ω^*_{th} in figure 4.1 (b). It can be seen that $\hat{V}_T$ hardly changes with ω^*_{th} for the range of $10^{-4} < \omega^*_{th} < 10^{-1}$. This means that the location of the vorticity isosurface hardly changes with ω^*_{th} when ω^*_{th} is taken from this range. By comparing the curves for two groups in figure 4.1 (a), $\hat{V}_T$ in group F is found to be flatter than group C in the range of $10^{-4} < \omega^*_{th} < 10^{-1}$, which indicates that the level of the numerical noise might be higher for group C.

The choice of the threshold is further discussed based on the joint probability density functions (jpdfs) of normalized vorticity magnitude ω^* and wall-normal distance y/δ,[28] which are shown in figure 4.2 for cases F002 and C002. Similar plots are obtained for F001 and C001 (not shown here). The jpdfs are also useful to examine the spatial distribution of vorticity. In the figure, the color contours of the jpdf are chosen so that the red, green, and cyan contours contain 50%, 40%, and 9% of fluid element in the computational domain, respectively, where the residual 1% fluid element can be ignored. The turbulent core region corresponds to the lower right corner (namely, low height and strong vorticity) while the small vorticity magnitude in the upper left is the vorticity in the freestream, which could arise by pressure wave radiations and numerical error. In case F002, it can be seen that the distribution of jpdf significantly changes with y around $y/\delta = 1$ in figure 4.2

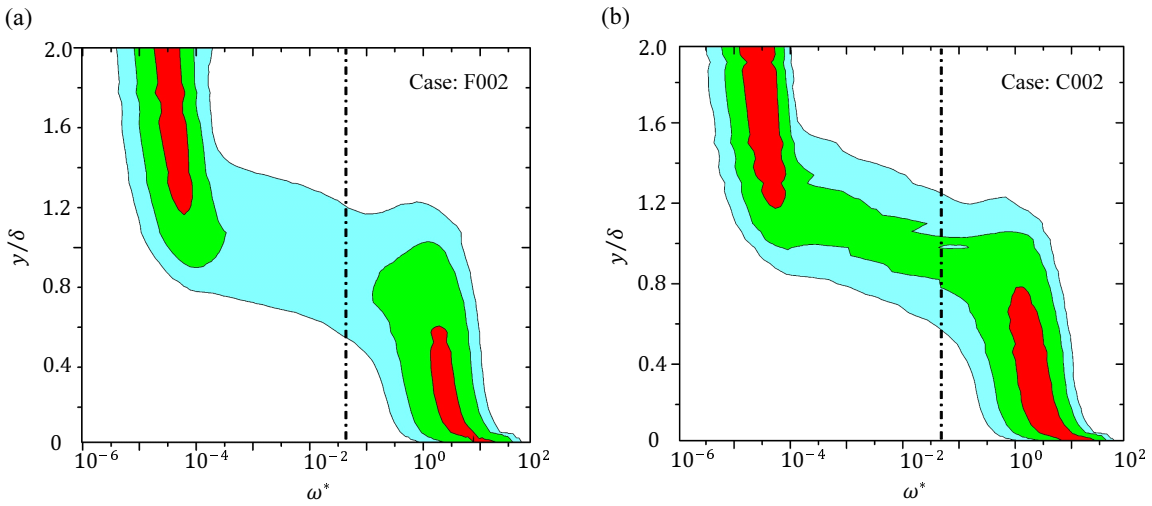

Figure 4.2 Jpdfs of normalized vorticity magnitude ω^* and vertical height y/δ. Contours contain 9%, 40%, and 50% of fluid element, which are shown with cyan, green, and red, respectively. (a) Case F002. (b) Case C002.

(a), which separates the lower right corner with large vorticity magnitude from the upper left corner with very small vorticity magnitude. A low probability is found for a fluid with intermediate values of vorticity magnitude around $y/\delta = 1$ in the figure 4.2 (a). This corresponds to a sharp jump in enstrophy found across the TNTI layer in previous studies.[10] In contrast, the jpdf for case C002 shown in figure 4.2 (b) exhibits a relatively large probability for a moderate level of vorticity magnitude around $y/\delta = 1$. The TNTI layer is very thin and should occupies small volume (low probability). This feature cannot be clearly seen in case C002 as relatively larger probability for indeterminate ω.

$\omega^*_{th} = 5.012 \times 10^{-2}$ ($\log(\omega^*_{th}) = -1.3$) is used to detected irrotational boundary in this study and shown as the dashed lines in figure 4.2. This value detects the turbulent region without including the region with small vorticity magnitude, where the irrotational boundary is represented as the isosurface of $\omega = \omega_{th}$. This threshold is on the plateau of $\hat{V}_T$ in figure 4.1 (a), where the turbulent volume is not sensitive to the choice of the threshold.

The top views of the irrotational boundary from all DNS dataset are visualized in figure 4.3. The irrotational boundary exhibits structures with various length scales, which are the imprints of turbulent structures underneath the TNTI layer.[29,76] The color of irrotational boundary shows dilatation $\nabla \cdot \boldsymbol{u} = -(D\rho/Dt)/\rho$ on the irrotational boundary. Positive and negative values of dilatation indicate the regions with fluid expansion and compression, respectively. It can be found that both compression and expansion regions coexist on the irrotational boundary, where the dilatation at $M = 1.6$ (F002, C002) is

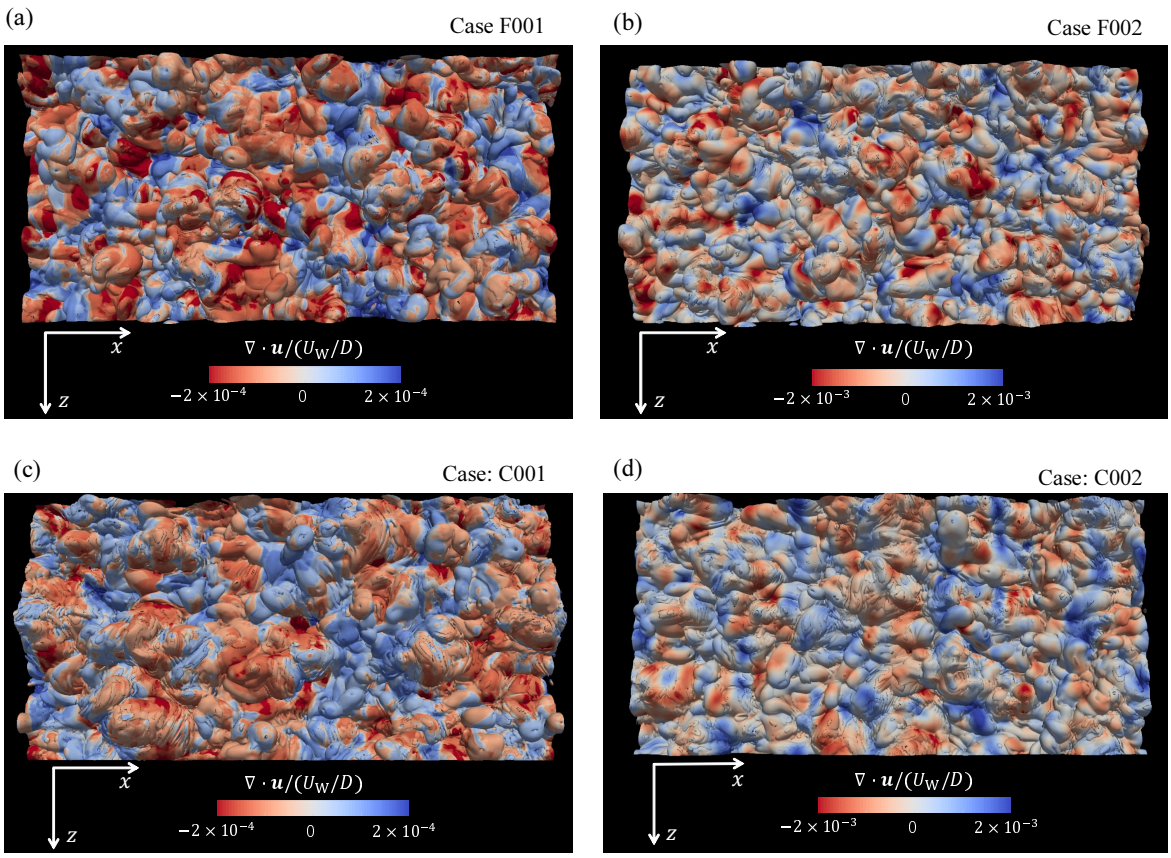

Figure 4.3 Visualization of irrotational boundary forming at the outer edge of the TNTI layer for (a) case F001, (b) case F002, (c) case C001, and (d) case C002. Color represents dilatation $\nabla \cdot \boldsymbol{u}$.

larger in magnitude than at $M = 0.8$ (F001, C001) by a factor of $\sim 10^1$.

The average resolution on the irrotational boundary (Δx_{IB}, Δy_{IB}, Δz_{IB}) is computed and shown in table 4.1, which is obtained by taking average of the mesh size at the grid points of all irrotational boundary locations. Δx_{IB}, Δy_{IB}, and Δz_{IB} are in comparison with the Kolmogorov length scale in the turbulent core region η_c. Here, the value at $y = 0.5\delta$ is used as the reference in the turbulent core region since non-turbulent fluids hardly reach this height. It should be stressed that although the TNTI appears in the intermittent region, the Kolmogorov scale η_c should be taken from the turbulent core region without including any contributions from non-turbulent fluids because the intermittent region contains both turbulent and non-turbulent fluids.[39,77] When η is computed in the intermittent region without excluding the contribution from the non-turbulent fluid, the value of η tends to be much larger than η_c since the non-turbulent flow has very large

Table 4.1 Average resolution at irrotational boundary.

Case	M	$\langle y_{IB}\rangle/\delta$	$\langle\Delta x_{IB}\rangle$	$\langle\Delta y_{IB}\rangle$	$\langle\Delta z_{IB}\rangle$
F001	0.8	0.85	$1.36\eta_c$	$1.42\eta_c$	$1.36\eta_c$
F002	1.6	0.83	$1.59\eta_c$	$1.36\eta_c$	$1.50\eta_c$
C001	0.8	0.87	$2.69\eta_c$	$1.80\eta_c$	$1.39\eta_c$
C002	1.6	0.87	$2.57\eta_c$	$1.84\eta_c$	$1.49\eta_c$

η.[39,77] In the present DNS, the average grid spacing at the outer edge of TNTI layer is about $1.5\eta_c$ in three directions in group F, which is close to the resolution in recent DNS of free shear flows used for studying the TNTI.[78,79] However, group C, where the grid size is determined solely from the wall unit, does not have a resolution enough to study the small scale near the TNTI especially in the x direction, where group C has the streamwise grid spacing determined based on the suggestion $\Delta x^+ < 9.7$ by Moser, Kim, and Mansour.[63] This is almost double of the grid spacing in the spanwise direction $\Delta x^+ \approx 2\Delta z^+$. This setting is reasonable for the near-wall region because the flow near the walls was found to be dominated by alternating high and low speed streaks, which is elongated in the streamwise direction.[80] However, the structure near the TNTI is very different from the near-wall region, resulting in the insufficient resolution near the TNTI in the streamwise direction for $\Delta x^+ \approx 2\Delta z^+$. It is also important to be careful with the grid size in the wall-normal direction near the TNTI layer since it is conventional to use finer grids near the wall and larger grid spacing in the intermittent region.

From the comparisons between groups F and C as shown in figure 4.3, it can be clearly seen how the resolution near the TNTI affects the geometry of TNTI. It should be noted that the DNS of group C has a mesh size small enough to resolve the near-wall structure and provides the global statistics, such as mean velocity and second order statistics, similar to group F. However, the influence of insufficient resolution in group C is crucial in the visualization in figures 4.3 (c) and (d): many stripy patterns exist on the enstrophy isosurface, which is hardly seen in the DNS of incompressible free shear flows.[77–79] On the contrary, the enstrophy isosurface visualized in group F (figures 4.3(a) and (b)) is much smoother and is similar to those obtained in previous DNS[77–79] and also of compressible shear layers.[40] It seems that the stripy patterns orthogonal to the streamwise direction in group C are caused by the insufficient resolution in the streamwise direction near the TNTI. The numerical noise, or oscillation in variables solved in the DNS, can produce the non-physical or artificial vorticity in the non-turbulent region near the TNTI. This explains different vorticity distributions between groups C and F in the figure 4.2, which result in a difficulty in the detection of irrotational boundary in group C.

Figure 4.4 shows the near-wall vortical structures with the irrotational boundary for

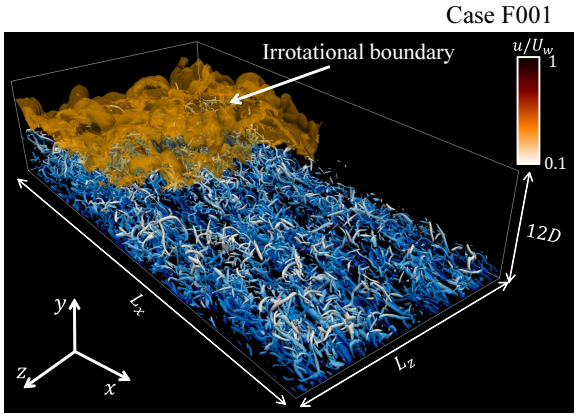

Figure 4.4 Near wall vortical structures visualized by isosurface of $Q/(U_W/D)^2 = 0.15$ colored by streamwise velocity u, and visualization of irrotational boundary in upper side for case F001.

case F001, where the semitransparent surface in the upper left side is the irrotational boundary and the near-wall vortical structures are shown with blue-white color indicating the streamwise velocity u. The vortical structures are visualized with the isosurface of the second invariant of velocity gradient tensor $Q/(U_W/D)^2 = 0.15$, where $Q = [2(\nabla \cdot \boldsymbol{u})^2 + \omega_i\omega_i - 2S_{ij}S_{ij}]/4$. It shows the well-known hairpin-like structures near the wall, while the irrotational boundary appears above these structures. The average height of the irrotational boundary $\langle y_{IB} \rangle$ is also shown in table 4.1, where the mean height is about 0.85 times of the boundary layer thickness δ in all cases. In the wall-normal direction, although the mesh is extremely fine near the wall ($\Delta y_W^+ < 0.2$) in group C, the grid spacing is still large near the TNTI, where the smallest length scale is not well resolved.

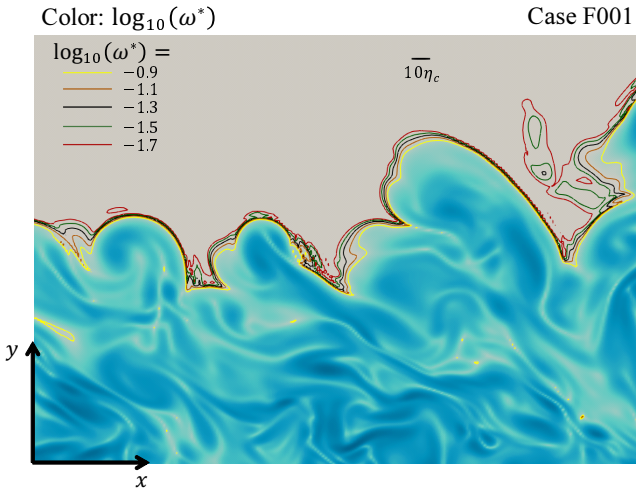

Figure 4.5 Visualization of irrotational boundary detected by different threshold values.

4.2 Dependence on threshold value for interface detection

For examining the robustness of the irrotational boundary location detected with vorticity magnitude, the isoline of vorticity magnitude is visualized for different thresholds in figure 4.5 for case F001. All of the threshold values are taken in the range of gray shadow shown in figure 4.1, where the irrotational boundary does not change much for these thresholds. For the relatively small values (green and red line), some bubbles of turbulent fluids appear surrounded by non-turbulent fluids. In contrast, small bubbles of non-turbulent fluids appear under the irrotational boundary when it is detected by a relatively large threshold (yellow line). The black and khaki lines detected by $\log(\omega^*) = -1.3$ and -1.1 are smoother and cause fewer bubbles, indicating that these are more appropriate thresholds than the other values. Figure 4.5 also shows the size of $10\eta_C$. For $\log(\omega^*) = -1.3$ and -1.1, the location of irrotational boundary is different by several times of η_C. Therefore, the range of $\log(\omega^*) = -1.3 \sim -1.1$ is a reasonable choice for a threshold value, and $\log(\omega^*) = -1.3$ is used in the present study.

4.3 Local coordinate system

Since the irrotational boundary detected as the enstrophy isosurface is located at the outer edge of the TNTI layer (An isosurface of vorticity magnitude $\sqrt{\omega_i\omega_i} = \omega_{th}$ is the same as an isosurface of enstrophy $\omega_i\omega_i/2 = \omega_{th}^2/2.$), the TNTI layer can be found just inside the irrotational boundary. The local coordinate y_I as shown in figure 4.6 (a) is used for computing the conditional statistics that is conditioned on the distance from the irrotational boundary. In this local coordinate system, the origin is located at the irrotational boundary, which is represented by $y_I = 0$. The direction of y_I is normal to the irrotational boundary, which is defined with the enstrophy gradient at the irrotational boundary:

$$\boldsymbol{n} = -\nabla\omega^2/|\nabla\omega^2|. \tag{4.2}$$

Positive/negative y_I points in the non-turbulent/turbulent region. Hereafter, subscript I denotes the conditional statistics and conditional average is denoted by $\langle\ \rangle_I$.

For finding suitable reference scale for studying TNTI layer, the conditional profiles of Kolmogorov scale ($\langle\nu\rangle_I^{3/4}/\langle\varepsilon\rangle_I^{1/4}$) are computed and shown in figure 4.6 (b). The Kolmogorov scale is quite large in the non-turbulent region, decreases rapidly from the non-turbulent to turbulent region, then tends to be uniform in the turbulent core region. Similar profiles of Kolmogorov scale near the TNTI were also seen in previous studies.[39,77] The geometry and statistical properties of the TNTI layer are characterized by the properties of turbulence in the turbulent region below the TNTI layer.[76,81] In the present study, the Kolmogorov scale at the location $y_I/\delta = -0.3$ shown by a large triangle in figure 4.6 (b), denoted by η_{TI}, is used as the reference length scale of turbulence near the TNTI, and the conditional statistics are presented against y_I/η_{TI}. The turbulent statistics computed from this location are marked with subscript TI. The other reference scales of turbulence near the TNTI, e.g., the Kolmogorov velocity scale $v_{\eta_{TI}} = (\langle\varepsilon\rangle_{TI}\langle\nu\rangle_{TI})^{1/4}$, are also calculated from the conditional statistics at this location. The Kolmogorov scale normalized by viscous units is also shown in the top left corner of figure 4.6 (b), where η_{TI} under the TNTI is around 3 times of viscous length scale.

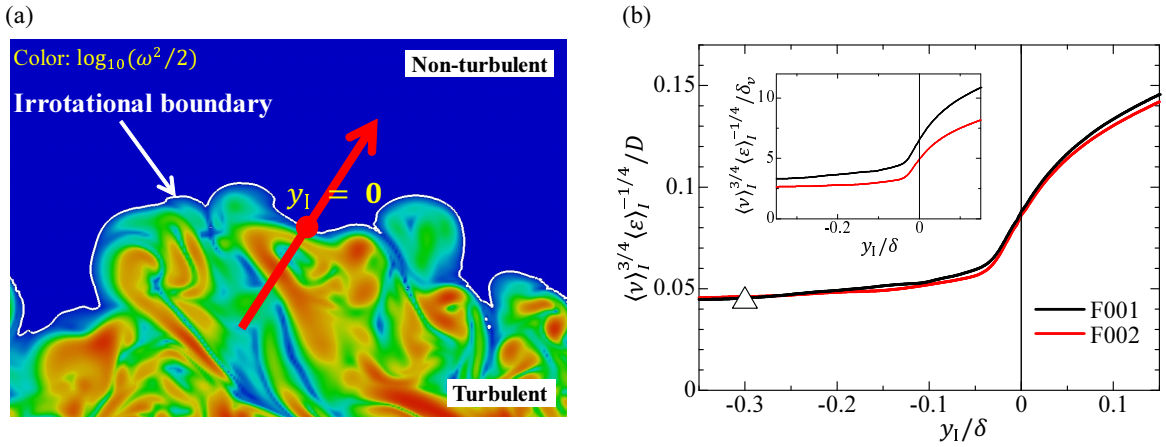

Figure 4.6 (a) Definition of local coordinate y_I, which is used for computing conditional statistics conditioned on the distance from the irrotational boundary. (b) Conditional profiles of Kolmogorov length scale defined with conditional average. △ shows the location where the Kolmogorov scale is taken as the reference length scale of turbulence near the TNTI. The Kolmogorov scale normalized by viscous unit is also shown in the top left corner.

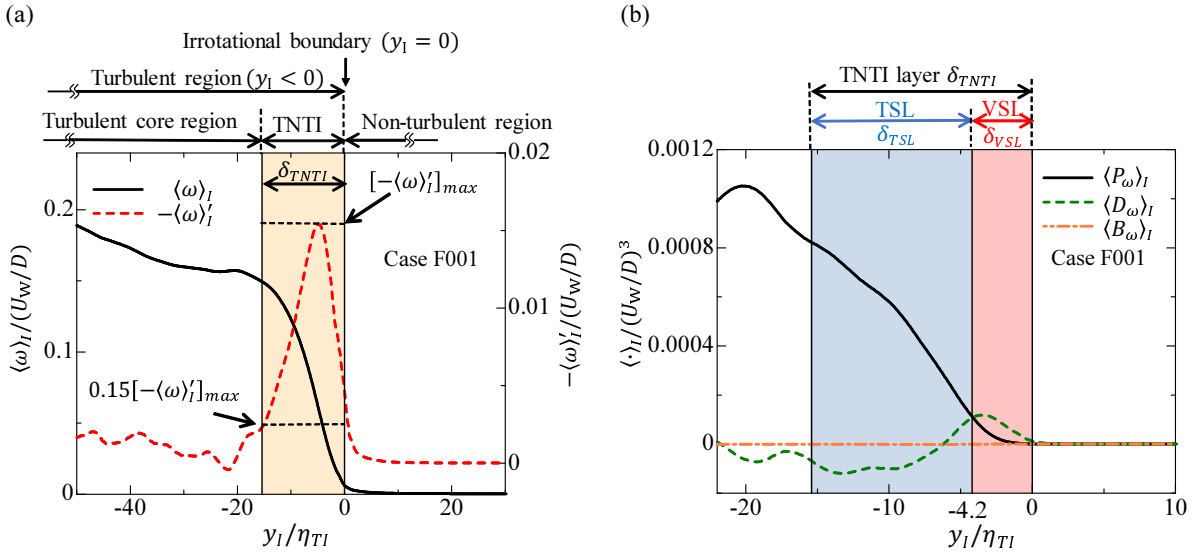

Figure 4.7 (a) Conditional mean vorticity and its derivative with respective to y_I for F001. (b) Conditional averages of enstrophy production P_ω, viscous diffusion D_ω, and baroclinic torque term B_ω for F001. These figures also define the turbulent/non-turbulent interfacial (TNTI) layer, viscous superlayer (VSL), turbulent sublayer (TSL), and turbulent core region.

4.4 The mean thickness of turbulent/non-turbulent interfacial layer

The structure of the TNTI layer is investigated here, which can be divided into two sublayers, VSL and TSL. The TNTI layer can be defined as a region where the vorticity magnitude is adjusted between the turbulent and non-turbulent regions and is characterized with a large gradient in vorticity magnitude. Therefore, the mean extent of the TNTI layer can be quantified based on the derivative of $\langle\omega\rangle_I$ with respective to y_I following to previous studies.[82] $\langle\omega\rangle_I$ and $-\langle\omega\rangle_I' = -d(\langle\omega\rangle_I)/d(y_I/\eta_{TI})$ are shown in figure 4.7 (a) for case F001 ($M = 0.8$). The mean thickness of the TNTI layer δ_{TNTI} is defined based on the location where $-\langle\omega\rangle_I'$ reaches 15% of its maximum value as in figure 4.7 (a). Therefore, the region of $-15.4 < y_I/\eta_{TI} < 0$ can be defined as the TNTI layer for F001.

The inner structures of the TNTI layer are well distinguished by vorticity dynamics, where the enstrophy evolves according to the following transport equation:[24,83]

$$\frac{D\omega^2/2}{Dt} = \omega_i S_{ij}\omega_j - \omega_i\omega_i\nabla\cdot\boldsymbol{u} + \frac{1}{\rho^2}\omega_i\varepsilon_{ijk}\frac{\partial P}{\partial x_j}\frac{\partial\rho}{\partial x_k} + \omega_i\varepsilon_{ijk}\frac{\partial}{\partial x_j}\left(\frac{1}{\rho}\frac{\partial\tau_{kl}}{\partial x_l}\right). \tag{4.3}$$

The terms on the right-hand side are the production term (P_ω) due to vortex stretch-

Table 4.2 The mean thicknesses of the TNTI layer, VSL and TSL normalized by the Kolmogorov scale and Taylor scale in the turbulent region near the TNTI layer.

Case	M	TNTI layer δ_{TNTI}	δ_{VSL}	δ_{TSL}
F001	0.8	$15.4\eta_{TI}$ / $0.96\lambda_{TI}$	$4.2\eta_{TI}$	$11.2\eta_{TI}$
F002	1.6	$16.3\eta_{TI}$ / $0.97\lambda_{TI}$	$4.2\eta_{TI}$	$12.1\eta_{TI}$
C001	0.8	$18.7\eta_{TI}$ / $1.08\lambda_{TI}$	$4.4\eta_{TI}$	$14.3\eta_{TI}$
C002	1.6	$20.4\eta_{TI}$ / $1.17\lambda_{TI}$	$4.4\eta_{TI}$	$16.0\eta_{TI}$

ing/compression, dilatation term (Θ_ω), baroclinic torque term (B_ω), and viscous term (V_ω), respectively. The viscous term can further be divided into four terms:

$$\begin{aligned}\omega_i\varepsilon_{ijk}\frac{\partial}{\partial x_j}\left(\frac{1}{\rho}\frac{\partial\tau_{kl}}{\partial x_l}\right) &= \nu\frac{\partial^2\omega^2/2}{\partial x_j^2} - \nu\left(\frac{\partial\omega_i}{\partial x_j}\right)^2 - \frac{1}{\rho^2}\varepsilon_{ijk}\omega_i\frac{\partial\tau_{kl}}{\partial x_l}\frac{\partial\rho}{\partial x_j} \\ &+ \varepsilon_{ijk}\frac{1}{\rho}\omega_i\left(\frac{\partial\tau_{kl}/\mu}{\partial x_l}\frac{\partial\mu}{\partial x_j} + \frac{\tau_{kl}}{\mu}\frac{\partial^2\mu}{\partial x_j\partial x_l} + \frac{\partial\tau_{kl}/\mu}{\partial x_j}\frac{\partial\mu}{\partial x_l}\right).\end{aligned} \tag{4.4}$$

From the first terms to forth terms in the right hand side represent the term of viscous diffusion (D_ω), the term of viscous dissipation (ε_ω), the term of viscous torque (S_ω), and the term arising from the temperature dependence of viscosity (μ_ω). Previous DNS studies have used the ratio between the production and viscous diffusion terms for defining the VSL.[24] Here, the VSL can be defined as the region within the TNTI layer, where D_ω is greater than P_ω. The conditional averages of P_ω, D_ω, and B_ω are shown in figure 4.7 (b) for case F001. At the irrotational boundary ($y_I = 0$), these terms are very small, which confirms that the isosurface with $\omega^*_{th} = 5.012 \times 10^{-2}$ is located at the outer edge of TNTI layer. These two terms begin to deviate from 0 from the irrotational boundary ($y_I = 0$) toward the turbulent region. The viscous diffusion term is larger than the production term near the irrotational boundary as found in many incompressible turbulent flows[24,83,84] and compressible shear layers.[38] Even though the baroclinic torque can generate enstrophy in the non-turbulent side for the high-speed flows, the conditional average of $\langle B_\omega\rangle$ is close to zero near the TNTI layer in the present DNS. DNS of compressible mixing layers[40] showed that it becomes more important within the TNTI layer as the convective Mach number increases. However, the enstrophy in the non-turbulent side is still very small so that the turbulent fluid can be detected with enstrophy in their DNS.[40] The baroclinic torque might play an important role in the enstrophy generation in the non-turbulent region if Mach number is much higher such as in hypersonic flows.

The mean position of the VSL can be identified as the region with $\langle D_\omega\rangle_I > \langle P_\omega\rangle_I$ near the irrotational boundary following to previous studies,[38,74] where the mean thickness of the VSL can be obtained as $\delta_{VSL} = 4.2\eta_{TI}$ from figure 4.7 (b). Thus, the region of

$-15.4 \leq y_I/\eta_{TI} \leq -4.2$ corresponds to the TSL, where the inviscid process (production term) has a larger contribution to the increase of the enstrophy. The TSL is also regarded as a buffer region between the VSL and the turbulent core regions.[83] The conditional statistics of vorticity and enstrophy transport for case F002 ($M = 1.6$) are similar to the ones of F001 ($M = 0.8$), and the mean thicknesses of TNTI layer (δ_{TNTI}), VSL (δ_{VSL}), and TSL (δ_{TSL}) for different Mach numbers M are shown in table 4.2, where the thicknesses are normalized by the Kolmogorov scale η_{TI} or Taylor microscale $\lambda_{TI} = (10\langle\nu\rangle_I\langle k_t\rangle_I/\langle\varepsilon\rangle_I)^{1/2}$. $\langle k_t\rangle_I = 1/2\sum_{i=1}^{3}[\langle u_i^2\rangle_I - \langle u_i\rangle_I^2]$ is the turbulent kinetic energy defined with conditional average) near the TNTI (at $y_I = -0.3\delta$). Although the thicknesses of TNTI layer and TSL slightly change with Mach number, the mean thickness of TNTI layer is about 15-16η_{TI} (0.96λ_{TI}), VSL is about 4η_{TI}, and TSL is about 11-12η_{TI} for group F.

These values normalized by the Kolmogorov scale in group F are close to previous studies in free shear flows[10,74,85] and shear free turbulence.[85] However, δ_{TNTI} in F001 and F002 exhibits a closer match when it is normalized by Taylor microscale. The present DNS is not enough to investigate the scaling of the thickness because the Reynolds number range is limited.

The study of the TNTI with the LES indicates that an insufficient resolution in simulations causes a thicker TNTI layer.[86] Indeed, the TNTI layer thickness tends to be larger for group C, which does not have a resolution enough to resolve the smallest scale in the turbulence near the TNTI.

Hereafter, all the statistical analysis in the following is done for group F. In addition, although the mean thicknesses of TNTI layer, VSL, and TSL slightly change with the Mach number, the differences are very small. Hereafter, the mean thicknesses of the TNTI layer, VSL, and TSL are assumed to be 15η_{TI}, 4η_{TI}, and 11η_{TI}, respectively, for simplification of the discussions.

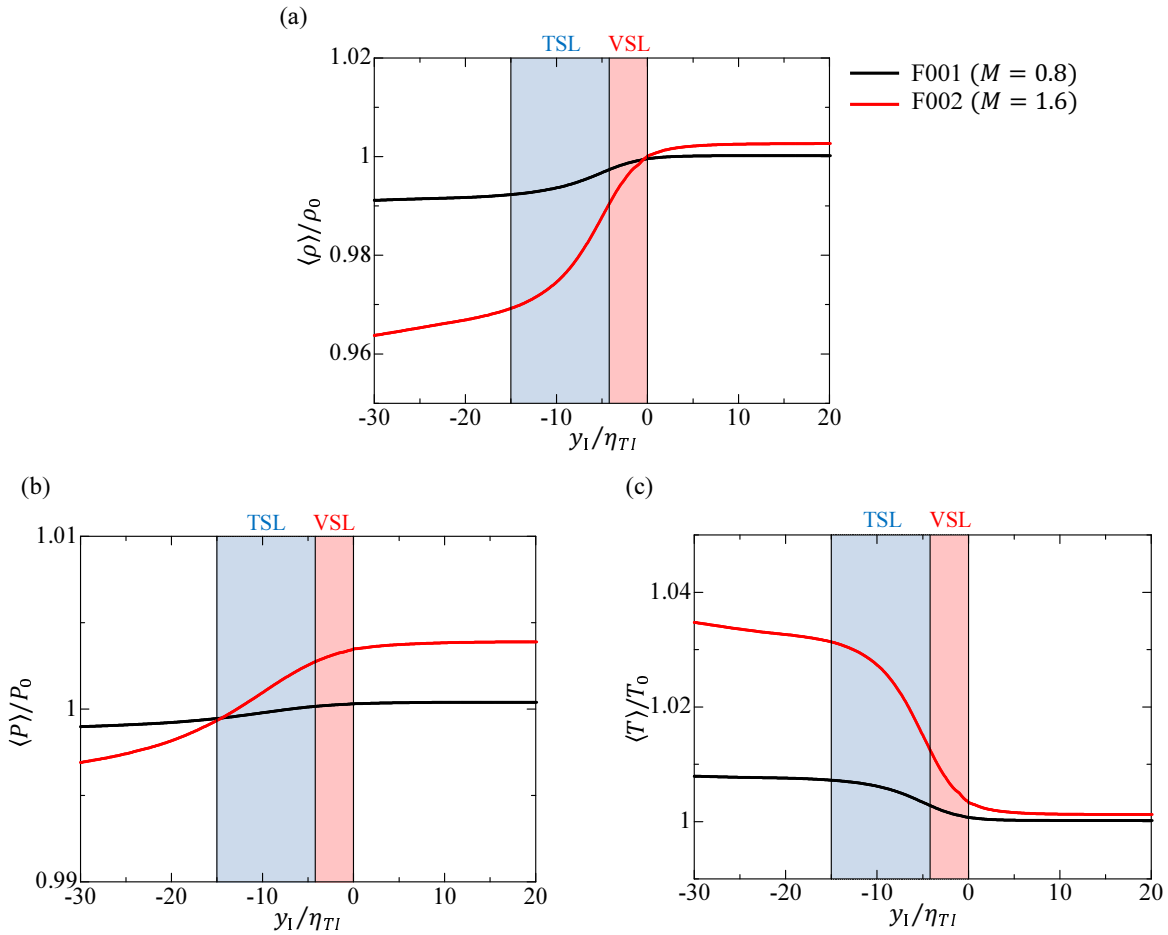

Figure 4.8 Conditional mean profiles of (a) density, (b) pressure, and (c) temperature.

4.5 Compressibility effects near the TNTI

The profiles of the conditional mean density, pressure and temperature near the TNTI are shown in figure 4.8. These quantities exhibit a jump near the TNTI layer, and the jump become sharp with the Mach number M. On another hand, the lower density and pressure, higher temperature are found in the turbulent side compared with the non-turbulent side. These indicates that the entrained fluid is expanded, and this expansion is increase with the Mach number. The dilatation is also calculated and the conditional mean profiles near the TNTI layer are shown in figure 4.9. The dilatation is defined in section 4.1. Positive and negative peaks, related to mean fluid expansion and compression, respectively, appear within TNTI layer. The peaks of mean expansion exist within the VSL, which confirms that the non-turbulent fluid passes during the entrainment process.

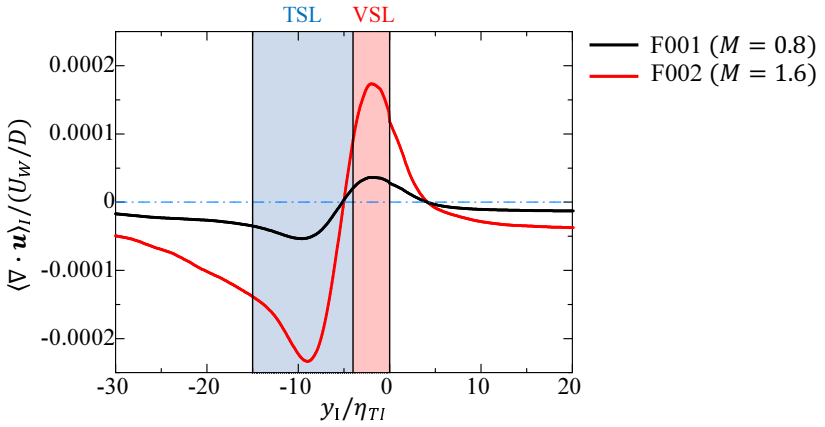

Figure 4.9 Conditional mean dilatation near the TNTI. The VSL and TSL estimated from the enstrophy statistics are identified in the figure.

On another hand, the peaks of mean compression exist within the TSL. It seems because the entrained fluid meet the turbulent flow in the TSL, this will be further discussed in the section 5.5. Furthermore, the mean expansion and compression in $M = 1.6$ are much stronger than in $M = 0.8$.

Figure 4.10 shows the conditional rms density fluctuation defined as $\langle\rho\rangle_{I.rms} = \sqrt{\langle\rho^2\rangle_I - \langle\rho\rangle_I^2}$ divided by the density in freestream ρ_∞. Even for $M = 1.6$, $\langle\rho\rangle_{I.rms}$ is about 2% of ρ_∞ near the TNTI layer, and the direct influences of compressibility are small near the TNTI layer as also expected from small turbulent Mach numbers in the outer region (figure 3.9).

For checking the existence of shockwaves/schocklets near the TNTI layer in the compressible boundary layers, local Mach number defined based on the local velocity and local sound speed as $M_L = |\boldsymbol{u}|/\sqrt{\gamma RT}$ is computed and shown in figure 4.11. It can be seen that the local Mach numbers M_L are smaller than the Mach number based on the wall velocity in most regions of the TBL. The local Mach number M_L in $M = 0.8$ is much smaller than 1 everywhere, but it exceeds 1 in the region very close to the wall for $M = 1.6$. Even through the small schoklets near the wall can be found in $M = 1.6$, they are very far from the intermittent region and hardly affect the TNTI layer. Shocklets are expected to appear in the intermittent region when the freestream Mach number is much higher than present DNS.[73] DNS of supersonic planar jets showed that compressibility affects the TNTI via the change in density and temperature.[51]

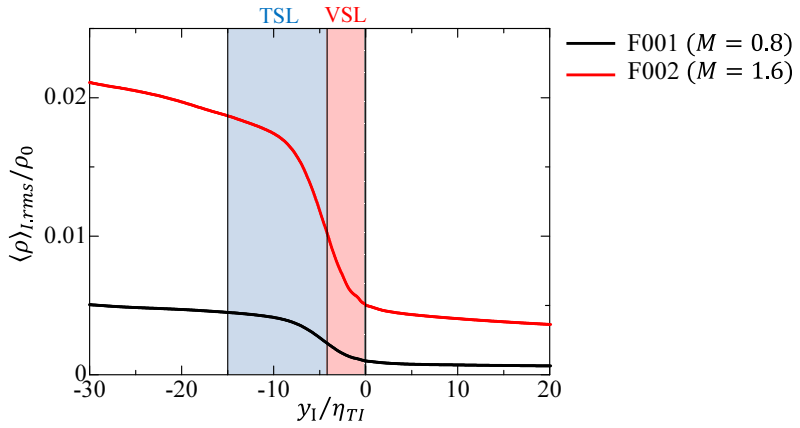

Figure 4.10 Conditional RMS density fluctuation.

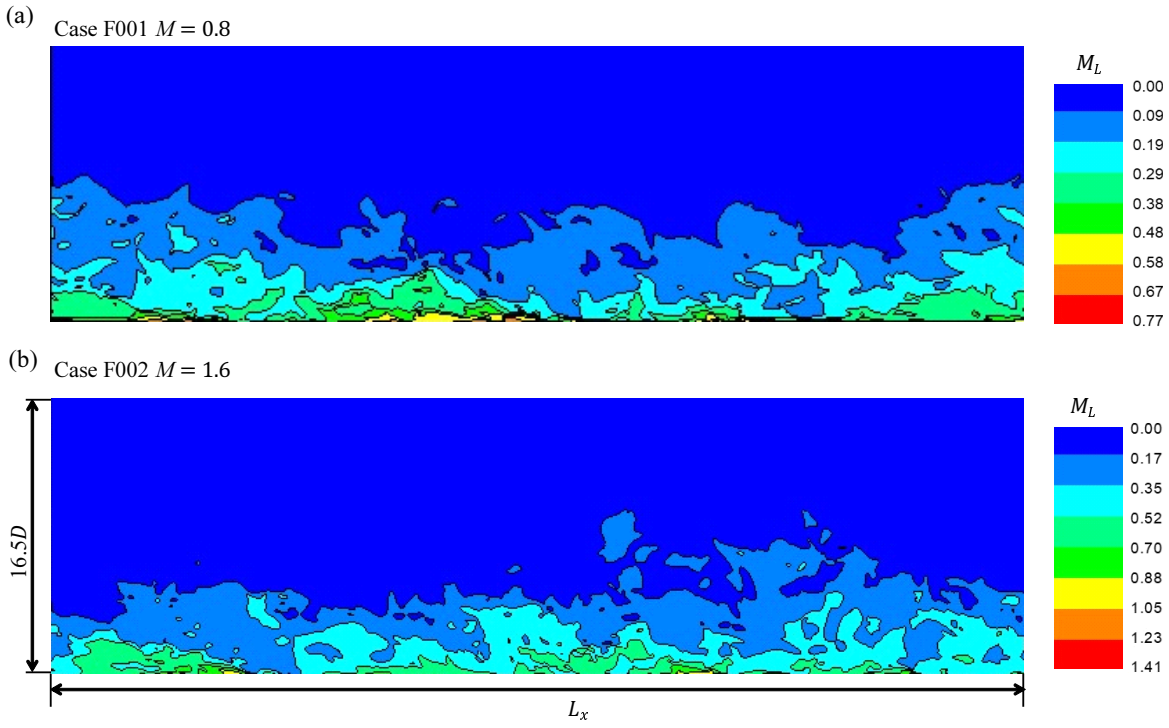

Figure 4.11 Isocontour of local Mach number M_L on x-y plane at $z = 0$ for (a) case F001 and (b) case F002.

4.6 Summary

Based on the 3D DNS data, the 3D irrotational boundary is detected as a vorticity magnitude isosurface, the mean thickness of TNTI layer and corresponding inner sublayers (VSL and TSL) are measured by computing the conditional mean vorticity and enstrophy transport equation.

The detected TNTI layer shown that the grid resolution near the TNTI in DNSs of group C is insufficient to resolve the smallest scale in the turbulence near the TNTI, which causes a thicker TNTI layer. In contrast, the results in group F are close to previous studies in free shear flows[10,74,85] and shear free turbulence.[85] Therefore, we suggest to set the DNS grid points as the ones in Group F for studying the TNTI in compressible TBLs. The mean thicknesses of the TNTI layer, VSL, and TSL are found to be around $15\eta_{TI}$, $4\eta_{TI}$, and $11\eta_{TI}$, respectively.

Even through the compressibility effects increase with Mach number, the conditional statistics confirm that the direct influences of compressibility are small near the TNTI layer even for Mach number $M = 1.6$, and the profiles of the conditional statistics are qualitatively similar between incompressible and compressible turbulent boundary layers.

Chapter 5

Entrainment process and passive scalar mixing near the TNTI layer in compressible turbulent boundary layers

This chapter will investigate the physical mechanism of the entrainment in compressible TBLs. As shown in chapter 4, all the statistical analysis in the chapter is done for only group F, F001 ($M = 0.8$) and F002 ($M = 1.6$). In addition, the mean thicknesses of the TNTI layer, VSL, and TSL are assumed to be $15\eta_{TI}$, $4\eta_{TI}$, and $11\eta_{TI}$, respectively, for simplification of the discussions.

5.1 Entrainment velocity

The velocity of the irrotational boundary (enstrophy isosurface) movement $\boldsymbol{u}^{\mathrm{I}}$ can be written as a sum of the propagation velocity $\boldsymbol{v}^{\mathrm{P}}$ (enstrophy isosurface propagation) and the fluid velocity $\boldsymbol{u}$, i.e., $\boldsymbol{u}^{\mathrm{I}} = \boldsymbol{v}^{\mathrm{P}} + \boldsymbol{u}$, where $\boldsymbol{v}^{\mathrm{P}} = v_n \boldsymbol{n}$. When the irrotational boundary propagated to the non-turbulent region, non-turbulent fluids pass through the irrotational boundary to the turbulent region, which is also called the local entrainment.[13] The propagation velocity can be derived by considering a local coordinate which moves with the irrotational boundary:[13]

$$v_n = \frac{D(\omega^2/2)/Dt}{|\nabla(\omega^2/2)|} = P_{v_n} + \Theta_{v_n} + B_{v_n} + V_{v_n} = \frac{P_\omega + \Theta_\omega + B_\omega + V_\omega}{|\nabla(\omega^2/2)|}. \tag{5.1}$$

The pdfs of the propagation velocity v_n are shown in figure 5.1, where the propagation velocities are normalized by the Kolmogorov velocity $v_{\eta_{TI}}$ in the turbulent core region near the TNTI at $y_I = -0.3\delta$. The positive value of v_n indicates that the irrotational boundary propagates into the non-turbulent region. It can be found that the irrotational boundary frequently propagates toward the non-turbulent region, and hardly propagates

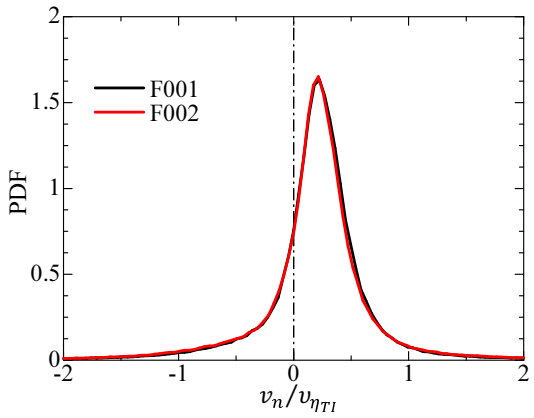

Figure 5.1 Conditional pdfs of propagation velocity v_n.

toward the turbulent region. The peak of propagation velocity is found to be the order of Kolmogorov velocity $v_{\eta_{TI}}$. These results are similar with incompressible flows.[13,74]

As described by the enstrophy transport equation, the terms on the right-hand side in equation (5.1) are the production term (P_{v_n}), dilatation term (Θ_{v_n}), baroclinic term (B_{v_n}), and viscous term (V_{v_n}), respectively. The conditional pdfs of these four terms are shown in figures 5.2 (a) and (b), and it reveals that the viscous term has the largest contribution in all terms as found in previous studies.[13,40,83,87] The viscous term of the propagation velocity V_{v_n} can further be divided into four terms: the diffusion term ($D_{v_n} = D_\omega/|\nabla(\omega^2/2)|$), the dissipation term ($\varepsilon_{v_n} = \varepsilon_\omega/|\nabla(\omega^2/2)|$), the viscous torque term ($S_{v_n} = S_\omega/|\nabla(\omega^2/2)|$), and the term related to temperature dependence of viscosity ($\mu_{v_n} = \mu_\omega/|\nabla(\omega^2/2)|$), whose pdfs are shown in figures 5.2 (c) and (d). It can be found that a positive value of propagation velocity is mainly contributed by the viscous diffusion while the terms related to viscous torque and temperature dependence of viscosity are almost negligible.

These results also show that the local entrainment mechanism described as the enstrophy transport is hardly affected by compressibility for the Mach number considered here. This observation agrees with previous studies on compressible boundary layers which have shown that compressibility effects are stronger in the near-wall region than in the outer region.[45,88] However, pervious study[73] also shows that some shocklets appear in the outer region when the Mach number M reach 3, the compressibility effects maybe become significant for entrainment process in this situation.

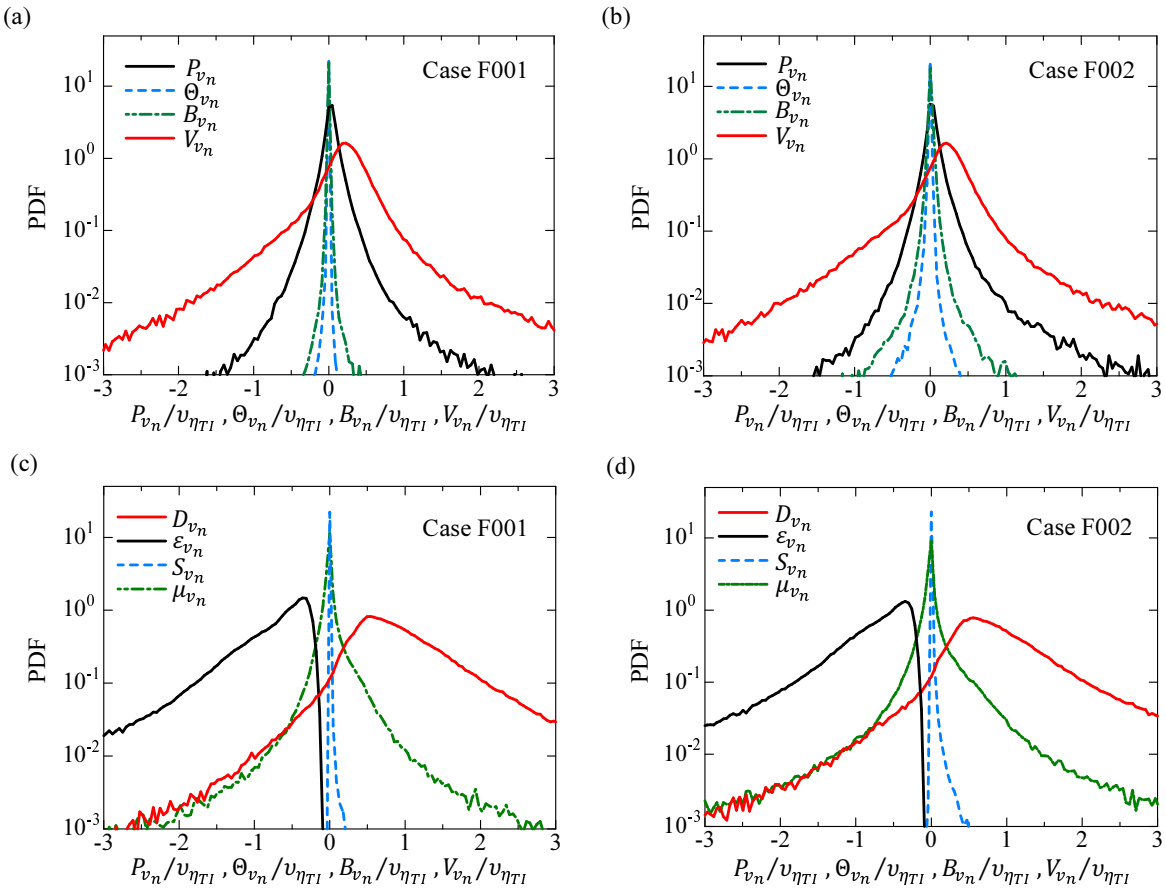

Figure 5.2 Conditional pdfs of the propagation velocity decomposed into different terms as in equation (5.1): (a) case F001; (b) case F002. Conditional pdfs of the contributions to V_{v_n} from four different viscous effects: (c) case F001; (d) case F002.

5.2 Mass fluxes by relative velocity of irrotational boundary near the TNTI

The propagation velocity, Eq. (5.1), shows the speed at which the non-turbulent fluid crosses the outer edge of the TNTI layer. The mass entrainment across the TNTI layer is also considered by introducing another local coordinate system $(\boldsymbol{x}^{\mathrm{I}}, t')$, which is moving with the irrotational boundary. The origin of this local coordinate system $\boldsymbol{x}^{\mathrm{I}}_{\mathrm{o}}$ is set on the irrotational boundary while t' represents the time in this local coordinate. The original coordinate system $(\boldsymbol{x}, t)$, whose origin is located at the center of the wall, is referred to as a fixed coordinate system hereafter. The location of $\boldsymbol{x} = \boldsymbol{x}^{\mathrm{I}}_{\mathrm{o}}$ in the fixed coordinate system is assumed to be located on the irrotational boundary, where the origin of this local coordinate system. By considering the coordinate transformation from the fixed coordinate system $(\boldsymbol{x}, t)$ to this local coordinate system $(\boldsymbol{x}^{\mathrm{I}}, t')$, the continuity equation in this local coordinate system can be written as below:[89]

$$\frac{\partial \rho}{\partial t'} = -\nabla \cdot (\rho(\boldsymbol{u}(\boldsymbol{x}^{\mathrm{I}}_{\mathrm{o}} + \boldsymbol{x}^{\mathrm{I}}) - \boldsymbol{u}^{\mathrm{I}})), \tag{5.2}$$

where the $\boldsymbol{u}^{\mathrm{I}}$ is the velocity of irrotational boundary movement. A similar equation for passive scalar in incompressible flows was also used in previous studies.[74,90] The term on the right-hand side in the above equation represents the pseudo transport of mass due to the relative velocity $\Delta\boldsymbol{u}^{\mathrm{I}} \equiv \boldsymbol{u}(\boldsymbol{x}^{\mathrm{I}}_{\mathrm{o}} + \boldsymbol{x}^{\mathrm{I}}) - \boldsymbol{u}^{\mathrm{I}}$ in the local coordinate system. The relative velocity can be written as:

$$\Delta\boldsymbol{u}^{\mathrm{I}} \equiv \boldsymbol{u}(\boldsymbol{x}^{\mathrm{I}}_{\mathrm{o}} + \boldsymbol{x}^{\mathrm{I}}) - \boldsymbol{u}^{\mathrm{I}} = \boldsymbol{u}(\boldsymbol{x}^{\mathrm{I}}_{\mathrm{o}} + \boldsymbol{x}^{\mathrm{I}}) - \boldsymbol{u}(\boldsymbol{x}^{\mathrm{I}}_{\mathrm{o}}) - \boldsymbol{v}^{\mathrm{P}}, \tag{5.3}$$

where $\boldsymbol{u}(\boldsymbol{x}^{\mathrm{I}}_{\mathrm{o}} + \boldsymbol{x}^{\mathrm{I}}) - \boldsymbol{u}(\boldsymbol{x}^{\mathrm{I}}_{\mathrm{o}})$ is the fluid velocity difference, and $\boldsymbol{v}^{P}$ is the propagation velocity. The fluid velocity difference is 0 at the irrotational boundary, which reveals that the mass transport is provided by the local entrainment at the irrotational boundary. The normalized mass flux $\boldsymbol{f} = \rho\Delta\boldsymbol{u}^{\mathrm{I}}/(\rho_0 U_W)$ in the local coordinate can be divided into the two components: an irrotational boundary normal component $f_N = \boldsymbol{f} \cdot \boldsymbol{n}/(\rho_0 U_W)$ and a tangential component $f_T = |\boldsymbol{f} - f^N\boldsymbol{n}|$. Because the tangential component is arbitrarily directed on the plane perpendicular to $\boldsymbol{n}$, the magnitude of the tangential flux is considered. It should be noted that the mass flux itself represents the mass transfer rather than the change in ρ at a given point, and a negative value of the normal component of mass flux f^N denotes that the mass transfer toward the turbulent region.

Figure 5.3 shows the conditional pdfs of f^N and f^T, at the several distances away from the irrotational boundary. The pdfs of the tangential component are not shown for the irrotational boundary because $f^T = 0$ at $y_I = 0$. From these pdfs, it can be found that the mass fluxes for normal component f^N are frequently negative at irrotational boundary ($y_I = 0$) and hardly depend on the location within the VSL while the tangential component f^T has a very small value in the viscous superlayer. A large probability for

negative f^N indicates a mass transfer from the non-turbulent region toward the turbulent region in a large part of the VSL. In the TSL and turbulent core region, the pdfs are very different from the VSL: both positive and negative values for f^N are observed; the tangential component f^T is no longer negligible compared with f^N.

For understanding the relation between normal and tangential mass transfers, the conditional joint pdfs of f^N and f^T are shown in figure 5.4, where the jpdfs are taken from the VSL and TSL. It can be found that the overall profile of the jpdf is very similar for both Mach numbers: $|f^N|$ is larger than f^T in most part of the VSL (large probability for $|f^N| > f^T$ in figures. 5.4(a) and (b)); a large value of f^T can be found in the TSL. The dependence of the jpdf of mass flux on the location within the VSL and TSL agrees well with the results obtained for a flux of passive scalar in incompressible flows.[74] These features can also be found in the conditional averages of f^N and f^T as shown in table 5.1. The jpdf within the VSL confirms a continuous mass transfer in an irrotational boundary normal direction from the non-turbulent toward the TSL across the VSL while the de-entrainment, defined as mass transfer from the turbulent to the non-turbulent region (positive f^N), hardly occurs. The TSL is characterized by a tangential mass transfer ($|f^N| < f^T$) for both Mach numbers. f^T in the TSL can be larger than $|f^N|$ within the VSL. Both positive and negative values of f^N can be found in the TSL. The positive value of f^N within the TSL is related to the mass transfer from the turbulent core region toward the TSL. A large probability for both signs of f^N confirms that there exist fluids within the TSL coming from both the turbulent and non-turbulent regions. The existence of the fluid coming from the turbulent core region also explains more turbulent-like features of the TSL, such as strong inviscid effects in the enstrophy evolutions. The standard deviations defined with conditional average are also shown for f^N and f^T in table 5.1. It can be seen that f^N has a larger fluctuation for case F002 within both VSL and TSL than for case F001, which implies larger magnitude of f^N appears in higher Mach number.

The entrainment process described by f^N and f^T is compared with the entrainment model based on a single vortex proposed in Ref.[81] It should be noted that the model developed for incompressible flows can be applied here because density fluctuations near the TNTI layer are very small even for $M = 1.6$. The model describes f^N and f^T on y_I as

$$f^N(y_I) = -\frac{1}{2}\rho_0\alpha_2(L + y_I) \tag{5.4}$$

$$f^T(y_I) = \frac{\rho_0\Gamma_0}{2\pi}\left|\frac{1}{L+y_I}\left[1-\exp\left(-\frac{(L+y_I)^2}{R_V^2}\right)\right] - \frac{1}{L}\left[1-\exp\left(-\frac{L^2}{R_V^2}\right)\right]\right| \tag{5.5}$$

with the model parameters of $L = \delta_{VSL} + R_V$, the constant radius of the vortex R_V, the strain rate for the steady Burgers vortex given by $\alpha_2 = 4\nu/R_V^2$, and the circulation Γ_0, which defines the circulation Reynolds number $Re_\Gamma = \Gamma_0/\nu$. The relation of these quantities to the turbulence characteristics has been studied in the boundary layers,[91] from which the values of $R_V = 5\eta_{TI}$ and $Re_\Gamma/Re_{\lambda_{TI}}^{1/2} = 13.7$ are taken, where η_{TI}, k_{TI},

and $Re_{\lambda_{TI}} = \lambda_{TI}(2k_{TI}/3)^{1/2}/\nu_{TI}$ are taken in the turbulent region near the TNTI layer ($y_I = -0.3\delta$). Here, $Re_{\lambda_{TI}}$ is 70 for $M = 0.8$ and 72 for $M = 1.6$. The thickness of the VSL, δ_{VSL}, is taken from table 4.2. From the turbulence characteristics at $y_I = -0.3\delta$, $f^N(y_I)$ and $f^T(y_I)$ can be obtained by Eqs. (5.4) and (5.5). Cross symbols in figure 5.4 show f^N and f^T from the model. For both Mach numbers, the model estimates (f^N, f^T) fairly well, where (f^N, f^T) obtained by the model is located near the values with the largest probability in the plots. The mass transfer across the TNTI layer is well represented by the flow related to a single vortex, which describes the entrainment across the TNTI layer as a two-stage process: i) the non-turbulent fluid is drawn toward the vortex core region within the VSL with the velocity related to the strain imposed on the vortex; ii) the circular motion caused by the vortex transfers the fluid being entrained toward the turbulent core region.

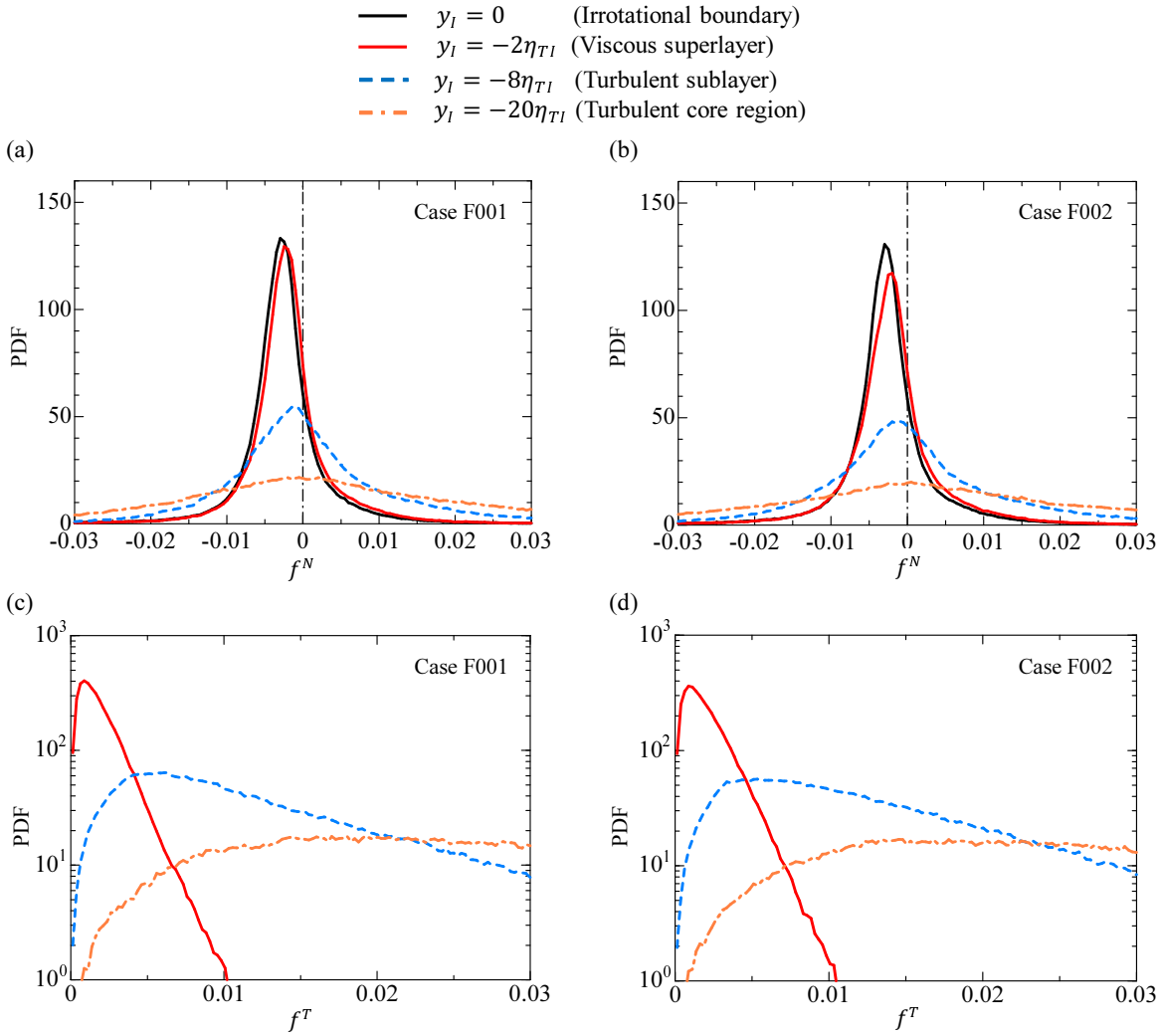

Figure 5.3 Conditional pdfs of mass fluxes across the TNTI layer described by relative velocity to irrotational boundary near the TNTI. The mass fluxes are decomposed in (a, b) normal and (c, d) tangential components to the irrotational boundary. (a, c) case F001 and (b, d) case F002.

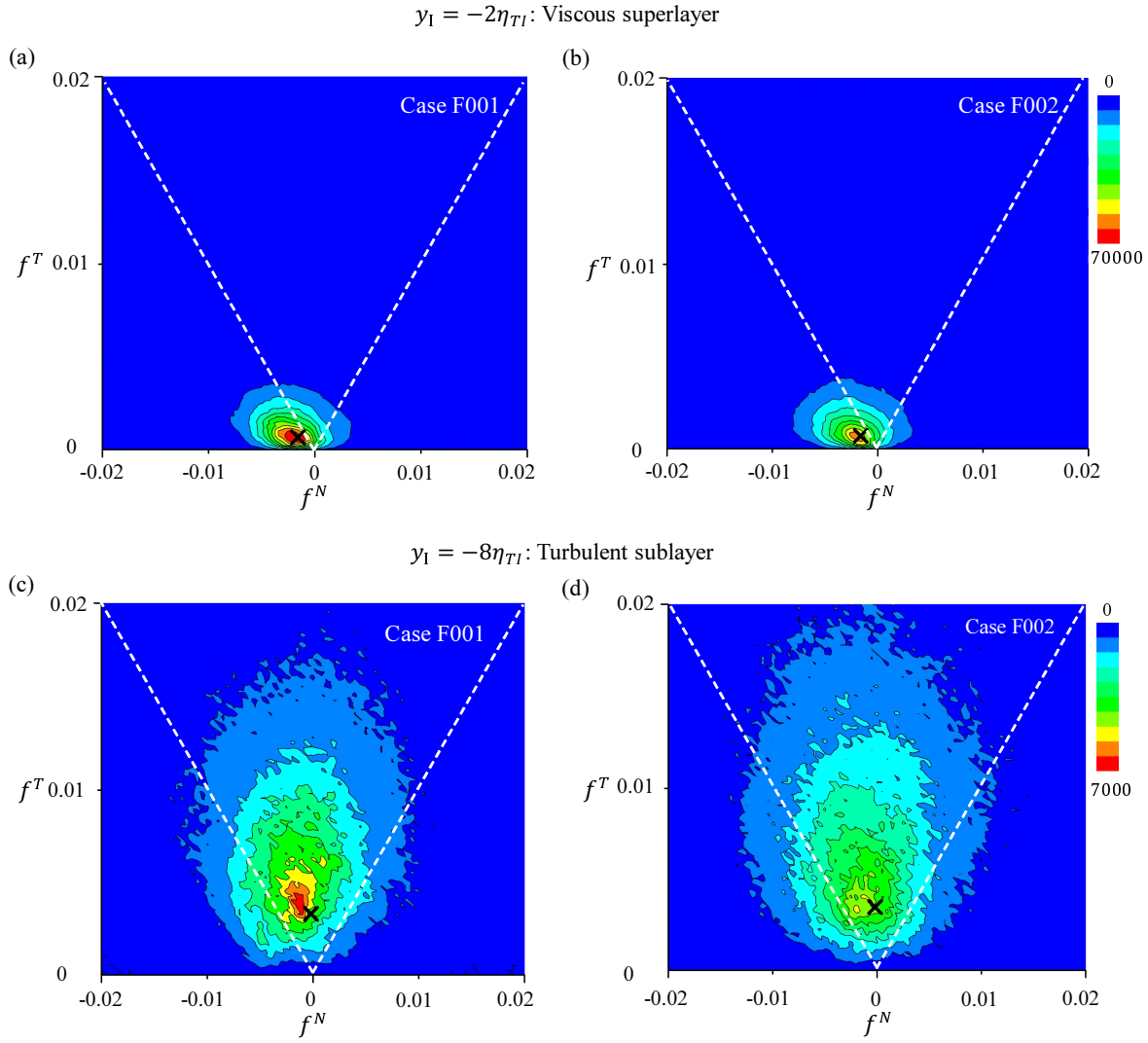

Figure 5.4 Conditional jpdfs of the tangential and normal mass fluxes to the irrotational boundary within the VSL (at $y_I = -2\eta_{TI}$) (a, b) and the TSL (at $y_I = -8\eta_{TI}$) (c, d). (a, c) case F001 and (b, d) case F002. The mass fluxes obtained by a single vortex model for the entrainment[81] at the same location of y_I are shown with cross symbols. White broken lines denote $|f^N| = f^T$.

Table 5.1 Conditional averages $\langle\cdot\rangle_I$ and standard deviations $\sigma(\cdot)$ of the tangential and normal mass fluxes to the irrotational boundary within the VSL (at $y_I = -2\eta_{TI}$) and the TSL (at $y_I = -8\eta_{TI}$).

	Case	M	$\langle f^N \rangle_I$	$\langle f^T \rangle_I$	$\sigma(f^N)$	$\sigma(f^T)$
VSL	F001	0.8	-0.58×10^{-2}	0.20×10^{-2}	0.47	0.15×10^{-2}
	F002	1.6	-0.70×10^{-2}	0.22×10^{-2}	1.11	0.16×10^{-2}
TSL	F001	0.8	-0.25×10^{-2}	0.14×10^{-1}	0.34	0.11×10^{-1}
	F002	1.6	-0.35×10^{-2}	0.15×10^{-1}	1.12	0.12×10^{-1}

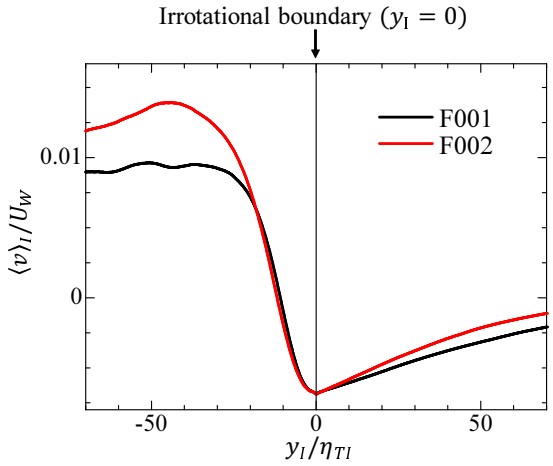

Figure 5.5 Conditional mean profiles of wall-normal velocity.

5.3 Entrainment process compared in temporal and spatial developing TBLs

Conditional mean of wall-normal velocity $\langle v \rangle_I$ is computed and shown in figure 5.5. $\langle v \rangle_I$ has a distinct Z-shaped profile near the TNTI layer, which is consistent with the experimental results of spatially-developing boundary layer.[30,92] Average of v in the x-z plane, $\langle v \rangle$, is close to zero at any location in the temporal simulations of compressible boundary layers unlike in spatial developing boundary layers. However, the mean fluid motion in the wall-normal direction described by $\langle v \rangle_I$ is similar for both spatial and temporal boundary layers.

Even through the differences of $\langle v \rangle_I$ between spatial and temporal boundary layers might be observed in the non-turbulent region very far from the TNTI (large y_I/δ that corresponds to the region of large y/δ, which is not included in the figure), $\langle v \rangle_I$ should be close to $\langle v \rangle$ because turbulent fluids do not reach this height in this region.

As shown in figure 5.5, negative $\langle v \rangle_I$ in the non-turbulent side is expected to be caused by the large-scale motion of TBLs, such as sweep motions and valley structures,[52] which are expected to be related to the engulfment. Indeed, the non-turbulent fluid in the intermittent region was shown to have mean downward velocity in the spatially developing incompressible TBL,[29] consistent with the present results for $\langle v \rangle_I$. Thus, the temporal simulation also captures well the process by which the non-turbulent fluids reach the TNTI, at least, in the intermittent region.

For comparing the mass entrainment between temporal and spatial TBLs, a feasible normalization method is required for the mass entrainment rate. In Kozul et al.,[48] both theoretical and DNS results confirmed that the momentum transport, which cause the

growth of the boundary layer thickness δ, is dominated by the same term in both temporal and spatial incompressible TBLs ($C_f \lesssim 0.005$ in their simulations), where $U_W^+ d\delta/dX$ in temporal TBLs is close to $U_\infty^+ d\delta/dx$ in spatial TBLs ($X = tU_W$: the temporal counterpart to x in spatial boundary layers). Furthermore, Chauhan[32] showed the averaged mass entrainment rate per unit horizontal area, denoted by f_m, can be calculated as $f_m = \rho U_\infty [d\delta/dx - d\delta^*/dx]$ in spatially-developing incompressible TBLs, where δ^* is the displacement thickness and U_∞ is the freestream velocity. It is also shown that δ/δ^* is constant in both compressible and incompressible TBLs.[37] These studies indicate that the mass entrainment rate f_m normalized by $u_\tau \rho$ is useful for comparison between temporal and spatial TBLs. Hereafter, $f_{m,t}$ and $f_{m,s}$ represent f_m for temporal and spatial boundary layers, respectively.

At first, $f_{m,s}/u_\tau \rho$ is examined based on previous experimental results of spatially-developing incompressible turbulent boundary layers at different Reynolds numbers[92] as shown in table 5.2. The normalized mass flux is $f_{m,s}/u_\tau \rho \approx 0.33$ for both experiments, which is expected from above discussion.

In terms of the TNTI, the mass entrainment rate is defined as the mass flux across the irrotational boundary. Then, the mass entrainment rate per unit horizontal area in the temporal boundary layer is calculated as $f_{m,t} \approx \rho_0 \langle v_n \rangle_I A_{IB}/L_x L_z$ from the present DNS, where $\langle v_n \rangle_I$ taken at $y_I = 0$, A_{IB} is the surface area of irrotational boundary, the freestream density ρ_0 used here is because the compressibility is very weak near the irrotational boundary as shown in figure 4.10. On the other hand, the averaged mass entrainment rate in spatially-developing compressible TBLs can be calculated by $f_{m,s} = \rho_0 U_\infty [d\delta/dx - d\delta^*/dx]$ based on the compressible TBL theory:[37] the theory of boundary layer thickness in incompressible TBLs $\delta^{5/4} = 0.289(\mu_0/\rho_0 U_\infty)^{1/4} x$ is also useful for compressible flows, because the boundary layer thickness δ does not depend significantly on the Mach number; the displacement thickness δ^* in compressible TBLs, defined as $\delta^* = \int_0^\infty (1 - \rho u/\rho_0 U_W) dy$, can be calculated by the relation of $\delta^*/\delta = 1 - 7F(M)/2\beta$ for compressible TBLs[37]

$$F(M) = \alpha_1^3 \ln(\alpha_1/(\alpha_1 - 1)) - \alpha_1^2 - \alpha_1/2 - 1/3, \tag{5.6}$$

where $\alpha_1 = 1 + 1/\beta, \beta = r(\gamma - 1)M^2/2$, and $r \approx 0.9$ for zero pressure gradient boundary layer. The above equations with the parameters in the present DNS give the averaged mass entrainment in spatially developing compressible TBL. Table 5.3 shows $f_{m,t}/u_\tau \rho_0$ and $f_{m,s}/u_\tau \rho_0$ for $M = 0.8$ and 1.6. For both Mach numbers, $f_{m,t}/u_\tau \rho_0$ and $f_{m,s}/u_\tau \rho_0$ have similar values, confirming that the mass entrainment rate per unit horizontal area is similar in both spatial and temporal TBLs. It is also clear that $f_{m,t}/u_\tau \rho_0$ and $f_{m,s}/u_\tau \rho_0$ are larger for $M = 1.6$ than for $M = 0.8$. Values of $f_{m,t}/u_\tau \rho_0$ and $f_{m,s}/u_\tau \rho_0$ for $M = 0.8$ are very close to those obtained in incompressible experiments summarized in table 5.2.

Table 5.2 Normalized mean mass entrainment rate per unit horizontal area in previous experiments of incompressible TBLs: $Re_\tau = 7870$ and 14500.[92]

Re_τ	7870	14500
$f_{m,s}/u_\tau\rho$	0.333	0.333

Table 5.3 Normalized mean mass entrainment rate per unit horizontal area in compressible TBLs. The temporal TBLs in the present DNS are compared with spatial compressible TBLs, where the entrainment rate is computed from the theoretical results of compressible TBLs.[37]

Case	M	$f_{m,t}/u_\tau\rho_0$	$f_{m,s}/u_\tau\rho_0$
F001	0.8	0.355	0.347
F002	1.6	0.398	0.392

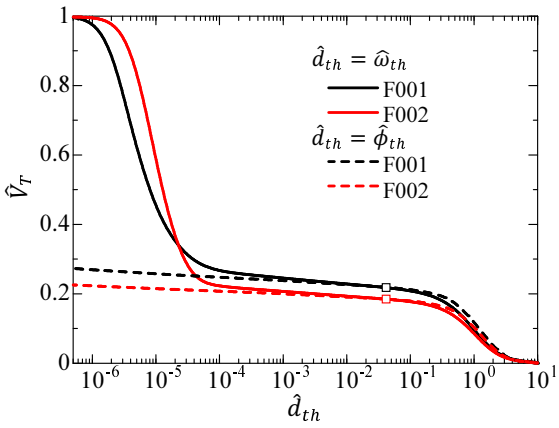

Figure 5.6 Normalized volume fractions of turbulent region V_T plotted against threshold $\hat{d}_{th}$ used for detecting turbulent fluids, $\hat{d}_{th}$ is $\hat{\omega}_{th}$ or $\hat{\phi}_{th}$.

5.4 The TNTI detected by a passive scalar

V_T computed as a function of $\hat{\omega}_{th}$ as shown in figure 5.6, where $\hat{\omega}_{th}$ is vorticity magnitude normalized by the mean vorticity magnitude $\overline{\omega}_c$ at $y = 0.5\delta$. In this study, the threshold value $\hat{\omega}_{th} = 0.04034$ is used to detect the irrotational boundary, which is the same value with $\omega*_{th}$ that is used in pervious section, only the normalization method is different. $\hat{\omega}_{th} = 0.04034$ is shown with the squares in figure 5.6. It has been already confirmed that the small change in $\hat{\omega}_{th}$ from this value hardly affects the location of the isosurface.[93]

It has been shown that the passive scalar is also a good marker of turbulent fluids,[78,94] and isosurface of ϕ with the threshold ϕ_{th} determined by the dependence of V_T and ϕ_{th} can be also used as the irrotational boundary.[78,94] V_T for turbulent fluids defined as $\phi > \phi_{th}$ is plotted against normalized threshold $\hat{\phi}_{th} = \phi_{th}/\overline{\phi}_c$ in figure 5.6. Unlike V_T computed with vorticity magnitude, V_T does not show rapid increase even for small $\hat{\phi}_{th}$. This is because the vorticity is computed with velocity gradient, which enhances small numerical error in velocity fields. Similar plots of V_T for vorticity magnitude and passive scalar were also obtained in incompressible TBLs and planar jets.[86,94]

The same value of normalized threshold is used for both vorticity magnitude and passive scalar. Thus, $\hat{\phi}_{th} = 0.04034$ is used in the analysis presented below. For these thresholds, both vorticity magnitude and passive scalar criteria result in almost same turbulent volume as shown in figure 5.6.

The irrotational boundary detected by a passive scalar is compared with the one detected by vorticity magnitude as shown in figure 5.7. The color shows the dilatation $\nabla \cdot \boldsymbol{u} = -(D\rho/Dt)/\rho$, and the positive and negative values indicate fluid expansion and compression in the regions, respectively. In these figures, the irrotational boundaries de-

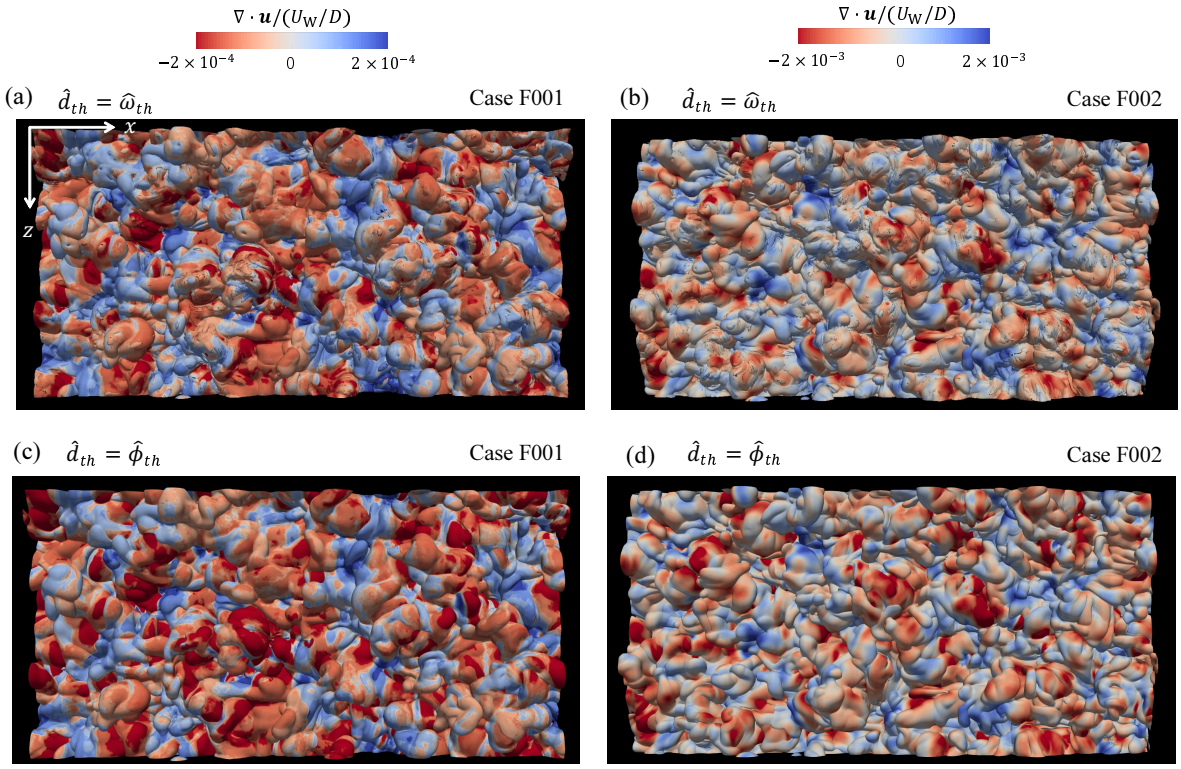

Figure 5.7 Visualization of irrotational boundary forming at the outer edge of the TNTI layer. Color represents dilatation $\nabla \cdot \boldsymbol{u}$. $\hat{d}_{th}$ indicates the threshold value of different detectors. The irrotational boundary detected by vorticity magnitude is shown in the upside for case F001 ($M = 0.8$) (a) and case F002 ($M = 1.6$) (b), detected by a passive scalar is shown in the bottom for case F001 ($M = 0.8$) (c) and case F002 ($M = 1.6$) (d).

tected by vorticity magnitude and passive scalar are very similar, including both colors (which indicates the expansion and compression regions). This implies that the passive scalar can be used to detect the irrotational boundary in experiments when vorticity magnitude is difficult to measure.

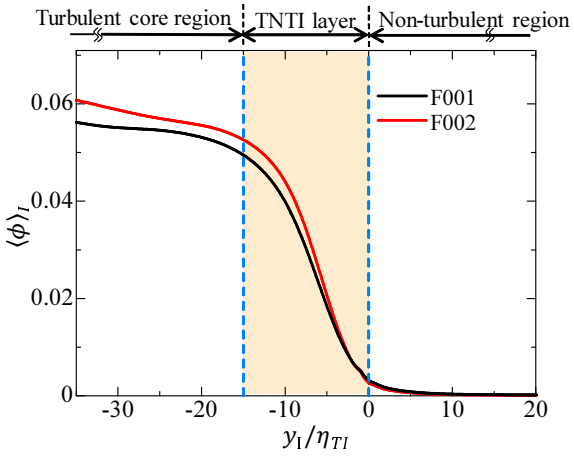

Figure 5.8 Conditional average of passive scalar.

5.5 Passive scalar in entrainment process

The conditional mean profiles of the passive scalar are shown in figure 5.8. $\langle\phi\rangle_I$ is very closed to zero in the non-turbulent region, exhibits a sharp jump within the TNTI layer, and tends to be constant in the turbulent core region. This profile also confirms that the passive scalar can be used as a detector function of turbulent fluids. The conditional average of scalar dissipation rate $\langle\varepsilon_\phi\rangle_I$ are calculated and shown in figure 5.9, where the scalar dissipation rate ε_ϕ is defined as:

$$\varepsilon_\phi = 2D_m \frac{\partial\phi}{\partial x_j}\frac{\partial\phi}{\partial x_j}. \tag{5.7}$$

There is a peak of scalar dissipation rate near the boundary between TSL and VSL. As discussed in previous studies,[74] the boundary between TSL and VSL is where a fluid with low vorticity (low scalar) from the non-turbulent region encounters a fluid with relatively high vorticity (high scalar) coming from the turbulent core region. This causes the scalar gradient to be very large here. This can be also found in the instantaneous profile of scalar dissipation rate on $x-y$ plane for case F001 ($M = 0.8$) (figure 5.10). There exist thin layers with high scalar dissipation rate near the irrotational boundary visualized by white lines, and these thin layers with high scalar dissipation rate near the TNTI layer are often aligned with the irrotational boundary.

Production terms of scalar gradient $G_iG_i = (\partial\phi/\partial x_i)^2$ and enstrophy can be written as $-G_iS_{ij}G_j$ and $\omega_iS_{ij}\omega_j$, respectively. These terms arise from the coupling between a strain tensor and vorticity or scalar gradient. The production rates related to the effective contribution of the strain are defined as $\alpha_\phi = -G_iS_{ij}G_jD/(G^2U_W)$ and $\alpha_\omega = \omega_iS_{ij}\omega_jD/(\omega^2U_W)$, which are also related to the alignment between strain eigenvectors

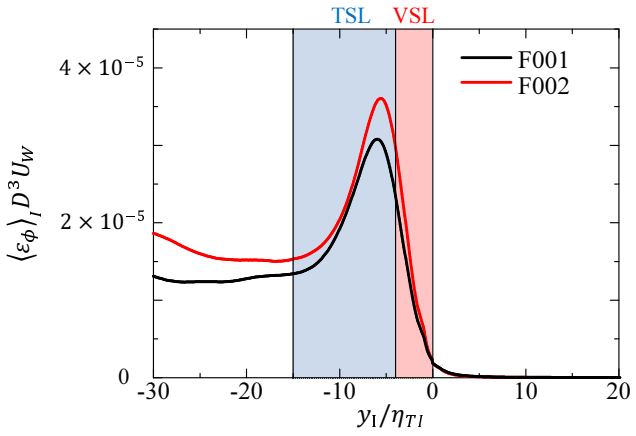

Figure 5.9 Conditional average of passive scalar dissipation rate.

and vorticity vector or scalar gradient.[95] Positive α_ϕ indicates dominant contribution of the compressive strain acting on the scalar gradient while positive α_ω indicates that vortex is stretched by the extensive strain. The conditional mean profiles of α_ϕ and α_ω are shown in figure 5.11. $\langle \alpha_\phi \rangle_I$ and $\langle \alpha_\omega \rangle_I$ are very similar for $M = 0.8$ and 1.6. They have positive values in the turbulent region. Thus, the enstrophy and scalar dissipation rate are produced via coupling between strain and vorticity vector or scalar gradient. Within the TNTI layer, $\langle \alpha_\phi \rangle_I$ and $\langle \alpha_\omega \rangle_I$ are larger than their non-turbulent values. $\langle \alpha_\phi \rangle_I$ and $\langle \alpha_\omega \rangle_I$ have a peak near the boundary between TSL and VSL.

From figure 5.10, there is a tendency that high scalar dissipation rate near the irrotational boundary appears more frequently when the irrotational boundary faces in the streamwise (x) direction. The orientation of the irrotational boundary can be distinguished by the unit normal vector $\boldsymbol{n} = (n_x, n_y, n_z)$.[96] For investigating the dependence on the interface orientation, the conditional statistics are computed separately for the leading edge and trailing edge, where leading edge defined as $n_x > 0.5$ faces the downstream direction and trailing edge $n_x < -0.5$ faces the upstream direction. It should be noted here that the downstream is the same orientation of x direction and upstream is the opposite orientation of x direction. The conditional averages of the scalar dissipation rate ε_ϕ and the production rate α_ϕ of G^2 for the leading edge and trailing edge are shown in figure 5.12. The scalar dissipation rate near the training edge is lower than the one near the leading edge, especially within the TNTI, in consistent with the visualization in figure 5.10. The production rate $\langle \alpha_\phi \rangle_I$ is also much higher near the leading edge, and $\langle \alpha_\phi \rangle_I$ near the training edge is very close to the non-turbulent value within the entire VSL and some part of TSL. The scalar gradient within the TNTI layer has a tendency of parallel alignment with the normal direction of the irrotational boundary[78] since the scalar

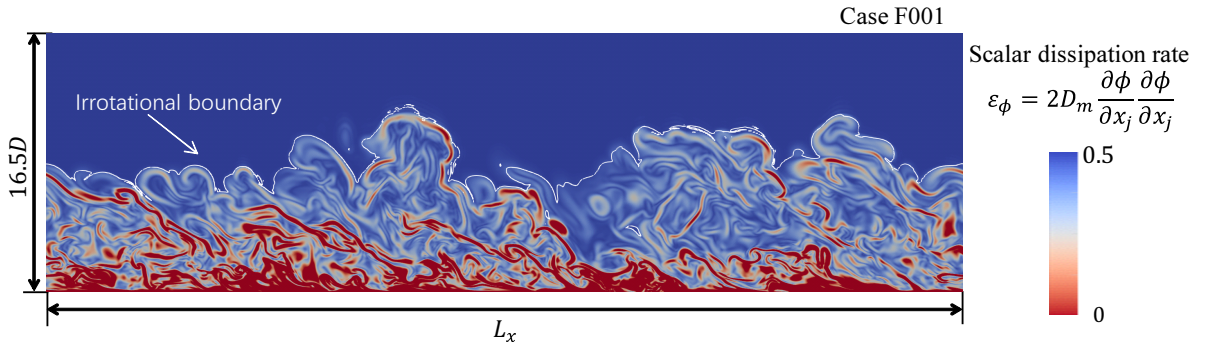

Figure 5.10 Instantaneous profile of scalar dissipation rate (color contour) and irrotational boundary (white line) on x-y plane for case F001 ($M = 0.8$).

rapidly changes across the TNTI layer. The orientation of the interface in relation to the mean flow direction has a strong influence on the strain field near the TNTI layer.[96,97] In the TBLs developing over the moving wall, the turbulent fluid has a larger streamwise velocity u than the non-turbulent fluid. The leading edge is the TNTI that faces the downstream direction, where the turbulent fluid with larger streamwise velocity is often located in the upstream side of the leading edge with smaller streamwise velocity. Then, the turbulent fluid near the leading edge tends to have $\partial u/\partial x < 0$, which is related to the compressive strain in the streamwise direction. Because the scalar gradient tends to align with the normal direction of the irrotational boundary, the compressive strain near the leading edge tends to align with the scalar gradient, and the scalar gradient is effectively intensified by the compressive strain. In contrast, a fluid with $\partial u/\partial x > 0$ often appears near the trailing edge because the turbulent fluid in the downstream side of the trailing edge has a larger streamwise velocity, and this extensive strain makes the production rate of G^2 smaller near the trailing edge. These dependences of $\langle \alpha_\phi \rangle_I$ also explain $\langle \varepsilon_\phi \rangle_I$, where the region with a small production rate $\langle \alpha_\phi \rangle_I$ has lower $\langle \varepsilon_\phi \rangle_I$. These dependences of $\langle \varepsilon_\phi \rangle_I$ and $\langle \alpha_\phi \rangle_I$ are similar to the relationship between the enstrophy production and TNTI orientation reported in the DNS of incompressible planar jets.[96]

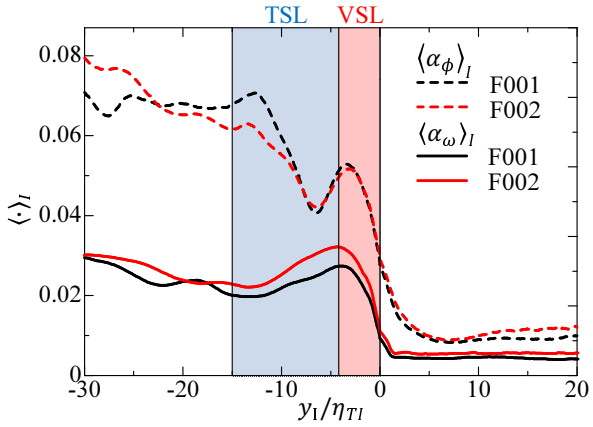

Figure 5.11 Conditional profiles of the production rate of enstrophy and scalar gradient.

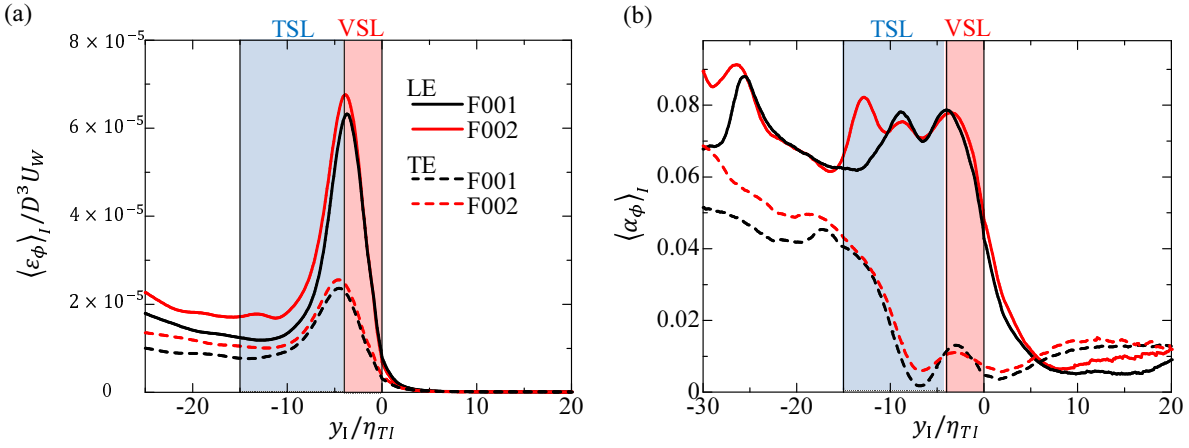

Figure 5.12 Conditional average of (a) scalar dissipation rate and (b) production rate of scalar gradient near the leading and trailing edges (LE: leading edge, TE: trailing edge).

5.6 Summary

The propagation velocity of irrotational boundary is computed for investigating the local entrainment process. It is found that the propagation velocity is dominated by the viscous effects, the irrotational boundary frequently propagates toward the non-turbulent region and hardly propagates toward the turbulent region.

In the intermittent region, the mean downward velocity is found for the non-turbulent flow. This is consistent with spatially developing TBLs.[29,92] The mass entrainment rate per unit horizontal area of the temporal TBLs is also found to be consistent with the theoretical prediction[37] for the spatial compressible TBL, and also with experimental data for a spatial incompressible TBL at Mach number $M = 0.8$. It confirms that the dominant mechanism for the momentum transport is not different between spatial and temporal compressible TBL.

The mass flux within the TNTI layer is studied by the mass transport equation in the local coordinate system $(\boldsymbol{x}^{\mathrm{I}}, t')$, which is moving with the outer edge of the TNTI layer. It shows that the mass within the VSL is transferred toward the TSL in the direction normal to the TNTI, while the TSL is dominated by a tangential transfer. The result is also compared with the single vortex model for incompressible flows.[81] This model indicates that the non-turbulent fluid is drawn toward the vortex core region within the VSL with the velocity related to the strain imposed on the vortex, then the circular motion caused by the vortex transfers the fluid being entrained toward the turbulent core region. The mass flux predicted by this model within the TNTI layer agrees well with the statistics result, which strongly suggests the connection between the entrainment process within the TNTI layer and the small-scale vortical structures found underneath the TNTI layer of the turbulent boundary layers.

The passive scalar mixing near the TNTI is also studied for investigating the entrainment process. The highest conditional mean scalar dissipation rate appears near the boundary between the VSL and TSL. This indicates that the fluid locally entrained from non-turbulent side encounters the fluid coming from the turbulent side, where the difference in the passive scalar between these fluids creates large scalar gradients. This discovery is similar with the one found in incompressible mixing layer.[74] Both visualization and conditional statistics show the dependence on the TNTI orientation for the scalar dissipation rate and the production rate of scalar gradient, both of which have a large value near the leading edge facing the downstream direction than the trailing edge facing the upstream direction.

Chapter 6

Real-World Data Circulation

In this chapter, the real-world data circulation (RWDC) and the relation with present study are explained. In addition, the contributions of this work on the society is also discussed.

6.1 Real-World Data Circulation

Real-World Data Circulation (RWDC) is a recent advanced new research field, which often conducts the real-world products or services in society and acquires comments or expectation for users. The information in RWDC is represented and analyzed in the form of data. By analyzing these data, people can create new designs or improve the old one based on the result of analysis.

The RWDC exists in many fields in the world, which is highly related to the development and globalization of the world. This topic is connected with many fields in the world,[98,99] e.g., business, medical treatment, economics, education and industries, namely, everywhere in our daily life. To improve the development and globalization of this world, people should know what is happening around the world and how it affects this world. In the real-world, even though people get data or information from the fields they are interested in, it is difficult to know how to use these data to contribute our life or understand things. That is the reason why we need to study RWDC.

Industries is of great importance in our daily life, from the plastic bag for food to the aircraft by which people can travel everywhere in this earth. However, the manufacturers cannot unilaterally create valuable products. In other words, techniques and user requirements are necessary for creating valuable products or services. The recent proposed fourth industrial revolution (Industry 4.0),[100] which has been developing with Information Technology (IT), has attracted a lot of attentions. This industrial revolution tries to connect many fields together, e.g., the Internet of Things (IoT), Cyber Physical System (CPS), information and communications technology (ICT), and Enterprise Architecture (EA).[101] RWDC is one of the key points in the realization of Industry 4.0.

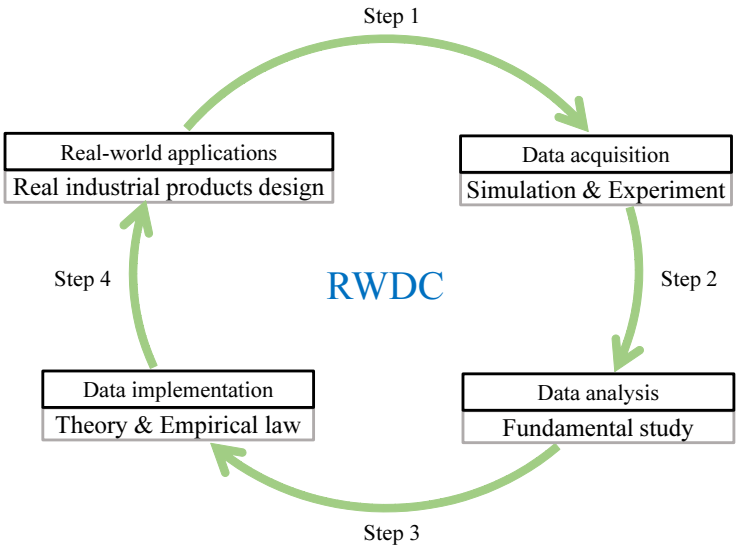

Figure 6.1 The general concept of RWDC in fluid dynamics.

6.2 Relation between RWDC and present study

Until now, many techniques in industries are quite limited, which makes a lot of difficulties to create desired products or service based on current techniques. For advancing the techniques, it is necessary to deeply understand the fundamental things, namely practical or industrial related science, which can help people essentially achieve a new stage of the technique.

Fluid dynamics plays a significant role in the performance of many applications in industries, e.g., aircraft, automobile. How to use the practical or industrial related science in fluid dynamics to improve industries can be studied by RWDC as shown in figure 6.1, which is a general concept of RWDC in fluid dynamics for industrial products design. Some products in industries may have some problems or users are not satisfied with these products, but engineers cannot solve them and need more information about the theory or fundamental characteristics. Then, researchers conduct some simulations or experiments to acquire data for the fundamental study. Thirdly, these fundamental studies can be done with the acquired data, and it can contribute to the development of the theories or empirical laws. Finally, the theories or empirical laws can be directly used for the industrial design. By these steps, the RWDC builds bridges for scientific study and real-world products design.

Computational fluid dynamics (CFD) is a widely used method for studying fluid dynamics. As shown in figure 6.2, CFD is used for designing many parts of A380, and the usage of CFD is growing rapidly due to the increases of computational resource.[1]

Figure 6.2 Example of growing usage of CFD for design of Airbus A380.[1]

The increase of the CFD usage also decreases the time and financial cost on aircraft design, because the aerodynamics studies of aircraft highly depended on the wind tunnel experiments in the past which takes a lot of time, human resources and financial cost. Commercial CFD software (CFX, Fluent, Fastran and Comsol and so on) are frequently used for flow simulations in industrial applications, including many complex flows, e.g., combustion flow, high speed flow, flow with heating wall. However, the turbulent flow simulations for industrial applications can only be done with turbulent model due to the limited computational resource in current stage. Even through these turbulent models excellently reduce the computational cost, it also brings some accuracy problems especially in complex flows. Until now, turbulent model is still one of the biggest problems in CFD community.

As mentioned in da Silva et al.,[10] a better understanding about the TNTI layer is needed in order to predict the chemical reaction flows or combustion flows, in which the properties essentially depended on the position and inner structures of TNTI layer. New computational algorithms and turbulent model near the TNTI layer should also be further considered, because this layer separates turbulent region and non-turbulent region where the grid mesh used in applications near the TNTI is generally larger than the thickness of this layer.

The present study focuses on the TNTI layer in compressible turbulent boundary layers, which can be found in many engineering applications as described in chapter 1, especially in aerospace engineering. The relation between RWDC and the study in this thesis can be explained by four steps as shown in figure 6.3. Firstly, the development of compressible

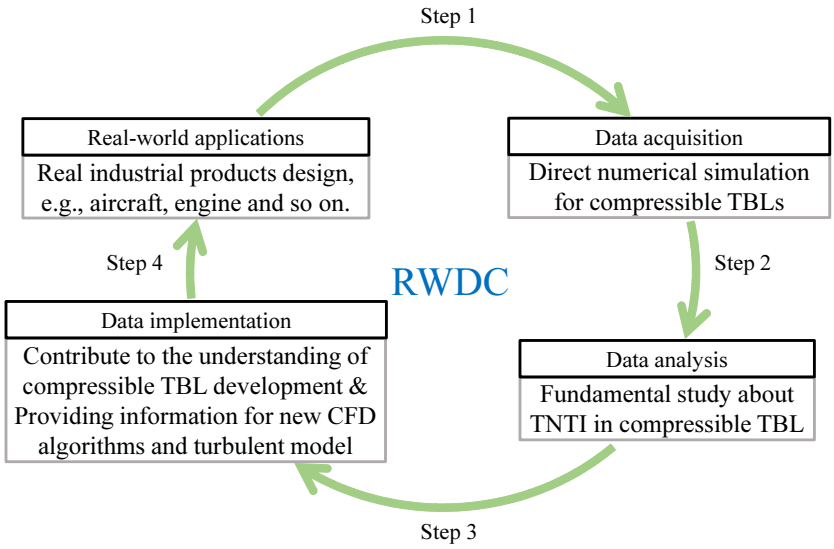

Figure 6.3 Connection of RWDC and TNTI study in compressible TBLs.

TBLs can significantly affect the efficiency and instability of the aircraft and vehicles, and the many fundamental mechanism about the development of compressible TBLs are still unclear as described in chapter 1, it need to be investigated more. Then, the direct numerical simulation of compressible TBLs are conducted for studying the fundamental characteristics of the TNTI layer and the entrainment process in compressible TBLs, which are strongly related to the development of compressible TBLs. Direct numerical simulations are conducted in present study is because it directly solves all the turbulence motions with different scales without any turbulent model. Thirdly, the results about the TNTI layer in present study can contribute to the understanding of the development of compressible TBLs, which can provide information for the CFD algorithms and turbulent model development near the TNTI. Finally, these improvement of compressible TBLs development understanding can be directly used for the real-world industrial products design, e.g., aircraft, turbine, and so on.

6.3 Contributions to the society

This work can contribute to the understanding of the development of compressible TBLs, which can significantly contribute to industrial products design from three points:

a. It can be used to improve the turbulent model and new CFD algorithms near the TNTI for compressible TBLs as described section 6.2. This will be a very big step if suitable turbulent model or new CFD algorithms can be developed for industries, because an improvement of CFD is an improvement for all the products design which are related to high-speed boundary layer. For example, the improvement of CFD in compressible TBLs can exactly improve the prediction of the flow around a high-speed vehicle, and it can be used to design a better vehicle with lower drag and higher stability, subsequently better efficiency.

b. In addition, understanding of the development of compressible TBLs is also helpful for develop related theories or empirical laws, which can be directly used in the industrial products design.

c. Furthermore, it also gives some ideas for flow control, e.g., it is possible to control the development of compressible TBL by controlling the large structures in the boundary layer because the large structure can affect properties of the TNTI in TBLs.

Until now, the work in present study mainly focuses on the first and second steps of the RWDC shown in figure 6.3, and contributes to the third step.

Chapter 7

Conclusion and Future Prospects

7.1 Conclusion

DNS of subsonic and supersonic temporally evolving turbulent boundary layers are performed for studying the TNTI. Two different setups of the DNS are considered, where in one case the grid spacing is determined solely based on the wall unit while the other case uses the computational grid small enough to resolve both the turbulent structures underneath the TNTI and near the wall. The global statistics are compared between the present DNS and previous studies, showing that the DNSs with both grids reproduce well the first- and second-order statistics of the fully-developed turbulent boundary layers.

However, the spatial distribution of vorticity in the outer region is found to be very sensitive to the spatial resolution near the TNTI. At the present Reynolds number ($Re_\theta \approx 2200$), the DNS based on the grid size determined by the wall unit does not have sufficient resolutions near the TNTI. The lack of the resolution results in the spiky patterns of the enstrophy isosurface used for detecting the outer edge of the TNTI layer and the thicker TNTI layer thickness. This problem can be solved by increasing the number of the grid points, where a smoother enstrophy isosurface is similar to the previous studies of incompressible free shear flows obtained in the DNS with the grid small enough to resolve Kolmogorov scale in the turbulent core region below the TNTI. Based on the 3D high-resolution DNS, the structure of the TNTI layer in compressible turbulent boundary layers can be investigated. The outer edge of TNTI layer, namely irrotational boundary, is detected as an isosurface of vorticity. The present results show that the thickness of the TNTI layer, defined with a large gradient of conditional mean vorticity magnitude, is about 15 times of the Kolmogorov scale η_{TI} in turbulence near the TNTI layer. The inner (sub)layers of the TNTI layer are detected based on the vorticity dynamics, where the TSL and VSL are found to have a thickness of 11-12η_{TI} and 4η_{TI}, respectively.

Even through the compressibility effects increase with Mach number, the conditional statistics confirm that the direct influences of compressibility are small near the TNTI layer, and the profiles of the conditional statistics are qualitatively similar between incompressible and compressible turbulent boundary layers. These structures of the TNTI layer

and their thicknesses divided by the Kolmogorov scale are very similar to those found in incompressible free shear flows. The compressibility effects at the Mach numbers $M = 0.8$ and 1.6 are very small within the TNTI layer, which appears in the outer intermittent region.

The local entrainment process is studied with the propagation velocity of the enstrophy isosurface, which represents the speed at which non-turbulent fluids crosses the outer edge of the TNTI layer. It has been shown that the compressibility effects are almost negligible for the propagation velocity, which is dominated by the viscous effects rather than a dilatational effect or baroclinic torque. The mean downward velocity is found in the non-turbulent region in the intermittent region, which is consistent with spatially-evolving boundary layers.[29,92] The mass entrainment rate per unit horizontal area of the temporal TBLs is consistent with the theoretical prediction[37] for the spatial compressible TBLs. This confirms that the dominant mechanism for the momentum transport, which is related to the TBL thickness growth, is not different between spatial and temporal compressible TBL as also found in incompressible TBLs.[53] Furthermore, the mass entrainment rate normalized by $u_\tau \rho_0$ at $M = 0.8$ also agrees well with experiments of spatially developing incompressible TBLs at various Reynolds numbers. Furthermore, the entrainment process across the TNTI layer is studied with the mass transport equation in the local coordinate system $(\boldsymbol{x}^{\mathrm{I}}, t')$ which is moving with the outer edge of the TNTI layer. The statistics of the mass flux show that the mass within the VSL is transferred toward the TSL in the direction normal to the TNTI while the TSL is dominated by a tangential transfer. These mass fluxes within the VSL and TSL are compared with the single vortex model for the entrainment within the TNTI layer, which was proposed for incompressible flows.[81] Because of very small effects of the compressibility in the outer region of the turbulent boundary layer, the entrainment model given by a single vortex predicts the mass flux within the TNTI layer fairly well, which strongly suggests the connection between the entrainment process within the TNTI layer and the small-scale vortical structures found underneath the TNTI layer of the turbulent boundary layers.

The irrotational boundary detected by an isosurface of passive scalar is also shown in this study, and the detected irrotational boundary shows an excellent agreement with the one detected by vorticity in visualization. It indicates passive scalar is also a good marker of turbulent fluids, which is easy to measure in experiment compared with vorticity. Conditional mean passive scalar also exhibits a sharp jump within the TNTI layer, and the highest conditional mean scalar dissipation rate appears near the boundary between the VSL and TSL. This indicates that the fluid locally entrained from non-turbulent side encounters the fluid coming from the turbulent side, where the difference in the passive scalar between these fluids creates large scalar gradients. It is also shown that the production rate of scalar gradient and enstrophy within the TNTI layer is as high as in the turbulent core region, and peaks in conditional averages of these quantities appear within the TNTI layer. Both visualization and conditional statistics show the dependence

on the TNTI orientation for the scalar dissipation rate and the production rate of scalar gradient, both of which have a large value near the leading edge facing the downstream direction than the trailing edge facing the upstream direction. The production rate of scalar gradient within the TNTI layer of the trailing edge is comparable to the non-turbulent value, which causes lower scalar dissipation rate near the trailing edge. These tendencies are explained from the difference in streamwise velocity between turbulent and non-turbulent fluids in a similar way to the TNTI orientation dependence of enstrophy production (rate) given for incompressible planar jets.[96,97]

7.2 Future Prospects

The Reynolds number dependence is one of the most important issues in the study of the TNTI layer. In previous literatures, the scaling of the mean thickness of the TNTI layer δ_{TNTI} has been argued extensively. The mean thickness of the TNTI layer, the Reynolds number dependence of turbulent statistics near and within the TNTI layer in the TBL all need to be investigated. How these statistics vary with the Reynolds number is also an important issue. There are several previous studies on the Reynolds number dependence of the TNTI layer in the TBL:[92] used the experimental data (Re_τ = 1230-14500) to study the Reynolds number dependence of the TNTI layer in the TBL. However, the TNTI layer in this study is detected with velocity, where the TNTI layer is treated as a shear layer. The interface detected by the velocity is completely different from the one detected by vorticity.[94] Borrell et al.[28] have studied the TNTI detected with vorticity using direct numerical simulation (DNS) database of the TBL. However, the Reynolds number range is still limited for Re_θ = 2800-6800 (Re_τ = 1000-2000). In addition, the wall can have a strong influence on the TNTI layer in the TBL.[29] This influence may result in difference with the results in free shear flows and it has not been studied well in previous papers. Therefore, the Reynolds number dependence of TNTI in TBL should be investigated in a future study. We plan to study the Reynolds number dependence by DNSs, which have enough fine resolution to solve the turbulent motions in the turbulence both underneath the TNTI layer and also the near-wall regions, with wide range of Reynolds number Re_θ = 2000-13000.

As mentioned in section 6.3, the final step is still absent in current stage. For understanding the connection from science studies to real-world products design, it is very important to complete this circle. Therefore, I plan to take some work with a company for fluid dynamics related work in inductry, and I believe that will highly enhances to my ability and my understanding about the RWDC.

Acknowledgements

This work would not be finished without the efforts and supports of my supervisor, and laboratory members. I would like to thank my supervisor Prof. K. Nagata. I am deeply thankful for his encouragement and guidance, and for the knowledge and insights that he shared on my research.

I would like to give special thanks to Dr. T. Watanabe for his patient support and helpful experiences. He has given me many constructive suggestions and guidance on my research. I also want to thank all the members in Fluid Dynamics Laboratory for their patient help and bringing me happiness.

I wish to thank Prof. K. Mori for his support. I also wish to thank Prof. Y. Sakai and Prof. Y. Tsuji for reviewing the thesis. I would like to thank Prof. C. B. da Silva (Technical University of Lisbon) and Dr. A. Sekimoto (Osaka University) for their valuable comments.

I would like to thank Graduate Program for Real-World Data Circulation Leaders (RWDC), Nagoya University for the financial support during my study. I am also thankful to Nagoya University for giving much support to my study and life.

Finally, the numerical simulations presented in this thesis were carried out on the high-performance computing system in Nagoya University and the high-performance computing system (NEC SX-ACE) in the Japan Agency for Marine-Earth Science and Technology. This work was partially supported by "Collaborative Research Project on Computer Science with High-Performance Computing in Nagoya University".

References

[1] A. Jameson and K. Ou, "50 years of transonic aircraft design," *Proc. Aero. Sci.*, vol. 47, no. 5, pp. 308–318, 2011.

[2] A. Gross and H. Fasel, "Investigation of low-pressure turbine separation control," in *AIAA Paper AIAA-2004-0750*, 2007.

[3] Z. Warhaft, "Passive scalars in turbulent flows," *Annu. Rev. Fluid Mech.*, vol. 32, no. 1, pp. 203–240, 2000.

[4] J. H. Lee, Y. S. Kwon, J. P. Monty, and N. Hutchins, "Tow-tank investigation of the developing zero-pressure-gradient turbulent boundary layer," in *Proc. 18th Austral. Fluid Mech. Conf.*, Austral. Fluid Mech. Soci., 2012.

[5] S. K. Robinson, "Coherent motions in the turbulent boundary layer," *Annu. Rev. Fluid Mech.*, vol. 23, no. 1, pp. 601–639, 1991.

[6] J. Jiménez, "Coherent structures in wall-bounded turbulence," *J. Fluid Mech.*, vol. 842, 2018.

[7] Y. Tsuji, J. H. M. Fransson, P. H. Alfredsson, and A. V. Johansson, "Pressure statistics and their scaling in high-reynolds-number turbulent boundary layers," *J. Fluid Mech.*, vol. 585, pp. 1–40, 2007.

[8] L. Prandtl, "Motion of fluids with very little viscosity," *NACA. Tech. Memo.*, vol. 452, 1928.

[9] S. Corrsin and A. L. Kistler, "Free-stream boundaries of turbulent flows," *NACA Tech. Rep.*, no. 1244, 1955.

[10] C. B. da Silva, J. C. R. Hunt, I. Eames, and J. Westerweel, "Interfacial layers between regions of different turbulence intensity," *Annu. Rev. Fluid Mech.*, vol. 46, pp. 567–590, 2014.

[11] D. K. Bisset, J. C. R. Hunt, and M. M. Rogers, "The turbulent/non-turbulent interface bounding a far wake," *J. Fluid Mech.*, vol. 451, pp. 383–410, 2002.

[12] C. B. da Silva, R. J. N. Dos Reis, and J. C. F. Pereira, "The intense vorticity structures near the turbulent/non-turbulent interface in a jet," *J. Fluid Mech.*, vol. 685, pp. 165–190, 2011.

[13] M. Holzner and B. Lüthi, "Laminar superlayer at the turbulence boundary," *Phys. Rev. Lett.*, vol. 106, no. 13, p. 134503, 2011.

[14] R. O. Fox, *Computational Models for Turbulent Reacting Flows*. Cambridge Univ. Pr., 2003.

[15] S. Tanaka, T. Watanabe, and K. Nagata, "Multi-particle model of coarse-grained scalar dissipation rate with volumetric tensor in turbulence," *J. Comput. Phys.*, vol. 389, pp. 128–146, 2019.

[16] L. K. Su and N. T. Clemens, "Planar measurements of the full three-dimensional scalar dissipation rate in gas-phase turbulent flows," *Exp. Fluids*, vol. 27, no. 6, pp. 507–521, 1999.

[17] R. L. Curl, "Dispersed phase mixing: I. Theory and effects in simple reactors," *AIChE J.*, vol. 9, no. 2, pp. 175–181, 1963.

[18] A. Y. Klimenko and R. W. Bilger, "Conditional moment closure for turbulent combustion," *Prog. Energy Combust. Sci.*, vol. 25, no. 6, pp. 595–687, 1999.

[19] M. J. Cleary and A. Y. Klimenko, "A generalised multiple mapping conditioning approach for turbulent combustion," *Flow, Turbul. Combust.*, vol. 82, no. 4, pp. 477–491, 2009.

[20] D. W. Meyer, "A new particle interaction mixing model for turbulent dispersion and turbulent reactive flows," *Phys. Fluids*, vol. 22, no. 3, p. 035103, 2010.

[21] T. Watanabe, T. Naito, Y. Sakai, K. Nagata, and Y. Ito, "Mixing and chemical reaction at high schmidt number near turbulent/nonturbulent interface in planar liquid jet," *Phys. Fluids*, vol. 27, no. 3, p. 035114, 2015.

[22] T. Watanabe, Y. Sakai, K. Nagata, Y. Ito, and T. Hayase, "Reactive scalar field near the turbulent/non-turbulent interface in a planar jet with a second-order chemical reaction," *Phys. Fluids*, vol. 26, no. 10, p. 105111, 2014.

[23] M. Gampert, K. Kleinheinz, N. Peters, and H. Pitsch, "Experimental and numerical study of the scalar turbulent/non-turbulent interface layer in a jet flow," *Flow, Turbul. Combust.*, vol. 92, no. 1-2, pp. 429–449, 2014.

[24] R. R. Taveira and C. B. da Silva, "Characteristics of the viscous superlayer in shear free turbulence and in planar turbulent jets," *Phys. Fluids*, vol. 26, no. 2, p. 021702, 2014.

[25] J. Mathew and A. J. Basu, "Some characteristics of entrainment at a cylindrical turbulence boundary," *Phys. Fluids*, vol. 14, no. 7, pp. 2065–2072, 2002.

[26] J. Westerweel, C. Fukushima, J. M. Pedersen, and J. C. R. Hunt, "Mechanics of the turbulent-nonturbulent interface of a jet," *Phys. Rev. Lett.*, vol. 95, no. 17, p. 174501, 2005.

[27] A. A. Townsend, *The structure of turbulent shear flow*. Cambridge Univ. Pr., 1976.

[28] G. Borrell and J. Jiménez, "Properties of the turbulent/non-turbulent interface in boundary layers," *J. Fluid Mech.*, vol. 801, pp. 554–596, 2016.

[29] J. Lee, H. J. Sung, and T. A. Zaki, "Signature of large-scale motions on turbulent/non-turbulent interface in boundary layers," *J. Fluid Mech.*, vol. 819, pp. 165–187, 2017.

[30] C. M. de Silva, J. Philip, N. Hutchins, and I. Marusic, "Interfaces of uniform momentum zones in turbulent boundary layers," *J. Fluid Mech.*, vol. 820, pp. 451–478, 2017.

[31] C. M. de Silva, J. Philip, K. Chauhan, C. Meneveau, and I. Marusic, "Multiscale geometry and scaling of the turbulent-nonturbulent interface in high Reynolds number boundary layers," *Phys. Rev. Lett.*, vol. 111, no. 4, p. 044501, 2013.

[32] K. Chauhan, J. Philip, C. M. de Silva, N. Hutchins, and I. Marusic, "The turbulent/non-turbulent interface and entrainment in a boundary layer," *J. Fluid Mech.*, vol. 742, pp. 119–151, 2014.

[33] J. Philip, C. Meneveau, C. M. de Silva, and I. Marusic, "Multiscale analysis of fluxes at the turbulent/non-turbulent interface in high Reynolds number boundary layers," *Phys. Fluids*, vol. 26, no. 1, p. 015105, 2014.

[34] Y. Zhuang, H. Tan, H. Huang, Y. Liu, and Y. Zhang, "Fractal characteristics of turbulent–non-turbulent interface in supersonic turbulent boundary layers," *J. Fluid Mech.*, vol. 843, 2018.

[35] T. Ishihara, H. Ogasawara, and J. C. R. Hunt, "Analysis of conditional statistics obtained near the turbulent/non-turbulent interface of turbulent boundary layers," *J. Fluids Struct.*, vol. 53, pp. 50–57, 2015.

[36] C. B. da Silva, R. R. Taveira, and G. Borrell, "Characteristics of the turbulent/nonturbulent interface in boundary layers, jets and shear-free turbulence," *J. Phys. Conf. Ser.*, vol. 506, p. 012015, 2014.

[37] A. J. Smits and J. P. Dussauge, *Turbulent shear layers in supersonic flow*. AIP Pr., 2006.

[38] R. Jahanbakhshi, N. S. Vaghefi, and C. K. Madnia, "Baroclinic vorticity generation near the turbulent/non-turbulent interface in a compressible shear layer," *Phys. Fluids*, vol. 27, no. 10, p. 105105, 2015.

[39] N. S. Vaghefi and C. K. Madnia, "Local flow topology and velocity gradient invariants in compressible turbulent mixing layer," *J. Fluid Mech.*, vol. 774, pp. 67–94, 2015.

[40] R. Jahanbakhshi and C. K. Madnia, "Entrainment in a compressible turbulent shear layer," *J. Fluid Mech.*, vol. 797, pp. 564–603, 2016.

[41] J. Mathew, S. Ghosh, and R. Friedrich, "Changes to invariants of the velocity gradient tensor at the turbulent–nonturbulent interface of compressible mixing layers," *Int. J. Heat Fluid Flow*, vol. 59, pp. 125–130, 2016.

[42] Y. Zhuang, H. Tan, W. Wang, X. Li, and Y. Guo, "Fractal features of turbulent/non-turbulent interface in a shock wave/turbulent boundary-layer interaction flow," *J. Fluid Mech.*, vol. 869, 2019.

[43] Z. Wang, J. Zhou, J. Fan, and K. Cen, "Direct numerical simulation of ozone injection technology for NOx control in flue gas," *Energy Fuels*, vol. 20, no. 6, pp. 2432–2438, 2006.

[44] M. P. Simens, J. Jiménez, S. Hoyas, and Y. Mizuno, "A high-resolution code for turbulent boundary layers," *J. Comput. Physics*, vol. 228, no. 11, pp. 4218–4231, 2009.

[45] S. Pirozzoli and M. Bernardini, "Turbulence in supersonic boundary layers at moderate Reynolds number," *J. Fluid Mech.*, vol. 688, pp. 120–168, 2011.

[46] P. R. Spalart, "Direct simulation of a turbulent boundary layer up to Reθ= 1410," *J. Fluid Mech.*, vol. 187, pp. 61–98, 1988.

[47] L. Kleiser and T. A. Zang, "Numerical simulation of transition in wall-bounded shear flows," *Ann. Rev. Fluid Mech.*, vol. 23, no. 1, pp. 495–537, 1991.

[48] M. Kozul, D. Chung, and J. P. Monty, "Direct numerical simulation of the incompressible temporally developing turbulent boundary layer," *J. Fluid Mech.*, vol. 796, pp. 437–472, 2016.

[49] S. E. Guarini, R. D. Moser, K. Shariff, and A. Wray, "Direct numerical simulation of a supersonic turbulent boundary layer at Mach 2.5," *J. Fluid Mech.*, vol. 414, pp. 1–33, 2000.

[50] M. P. Martín, "Direct numerical simulation of hypersonic turbulent boundary layers. Part 1. Initialization and comparison with experiments," *J. Fluid Mech.*, vol. 570, pp. 347–364, 2007.

[51] R. Nagata, T. Watanabe, and K. Nagata, "Turbulent/non-turbulent interfaces in temporally evolving compressible planar jets," *Phys. Fluids*, vol. 30, no. 10, p. 105109, 2018.

[52] S. B. Pope, *Turbulent Flows*. Cambridge Univ. Pr., 2000.

[53] M. Kozul and D. Chung, "Direct numerical simulation of the incompressible temporally developing turbulent boundary layer," in *Proc. 19th Austral. Fluid Mech. Conf.*, Austral. Fluid Mech. Soci., 2014.

[54] J. H. Lee, Y. S. Kwon, J. P. Monty, and N. Hutchins, "Time-resolved PIV measurement of a developing zero pressure gradient turbulent boundary layer," in *Proc. 19th Austral. Fluid Mech. Conf.*, Austral. Fluid Mech. Soci., 2014.

[55] A. Kempf, M. Klein, and J. Janicka, "Efficient generation of initial-and inflow-conditions for transient turbulent flows in arbitrary geometries," *Flow, Turbul. Combust.*, vol. 74, no. 1, pp. 67–84, 2005.

[56] G. Lodato, P. Domingo, and L. Vervisch, "Three-dimensional boundary conditions for direct and large-eddy simulation of compressible viscous flows," *J. Comput. Phys.*, vol. 227, no. 10, pp. 5105–5143, 2008.

[57] T. J. Poinsot and S. K. Lelef, "Boundary conditions for direct simulations of compressible viscous flows," *J. Comput. Phys.*, vol. 101, no. 1, pp. 104–129, 1992.

[58] Z. Wang, Y. Lv, P. He, J. Zhou, and K. Cen, "Fully explicit implementation of direct numerical simulation for a transient near-field methane/air diffusion jet flame," *Comput. Fluids*, vol. 39, no. 8, pp. 1381–1389, 2010.

[59] C. Bogey and C. Bailly, "Turbulence and energy budget in a self-preserving round jet: direct evaluation using large eddy simulation," *J. Fluid Mech.*, vol. 627, pp. 129–160, 2009.

[60] C. A. Kennedy and A. Gruber, "Reduced aliasing formulations of the convective terms within the Navier–Stokes equations for a compressible fluid," *J. Comput. Phys.*, vol. 227, no. 3, pp. 1676–1700, 2008.

[61] T. A. Zang, "On the rotation and skew-symmetric forms for incompressible flow simulations," *Appl. Numer. Math.*, vol. 7, no. 1, pp. 27–40, 1991.

[62] M. H. Carpenter and C. A. Kennedy, "Fourth-order 2N-storage Runge-Kutta schemes," *NACA Tech. Rep.*, 1994.

[63] R. D. Moser, J. Kim, and N. N. Mansour, "Direct numerical simulation of turbulent channel flow up to $Re_\tau = 590$," *Phys. Fluids.*, vol. 11, no. 4, pp. 943–945, 1999.

[64] R. E. Falco, "Coherent motions in the outer region of turbulent boundary layers," *Phys. Fluids*, vol. 20, no. 10, pp. S124–S132, 1977.

[65] M. Gampert, V. Narayanaswamy, P. Schaefer, and N. Peters, "Conditional statistics of the turbulent/non-turbulent interface in a jet flow," *J. Fluid Mech.*, vol. 731, pp. 615–638, 2013.

[66] E. J. Hopkins and M. Inouye, "An evaluation of theories for predicting turbulent skin friction and heat transfer on flat plates at supersonic and hypersonic Mach numbers," *AIAA J.*, vol. 9, no. 6, pp. 993–1003, 1971.

[67] E. R. Van Driest, *The problem of aerodynamic heating.* Aeronaut. Engng Rev., 1956.

[68] A. J. Smits, N. Matheson, and P. N. Joubert, "Low-Reynolds-number turbulent boundary layers in zero and favorable pressure gradients," *J. Ship Res.*, vol. 27, no. 3, pp. 147–157, 1983.

[69] E. R. Van Driest, "Turbulent boundary layer in compressible fluids," *J. Aeronaut. Sci.*, vol. 18, no. 9, pp. 145–160, 1951.

[70] L. P. Erm and N. J. Peter, "Low-Reynolds-number turbulent boundary layers," *J. Fluid Mech.*, vol. 230, pp. 1–44, 1991.

[71] M. V. Morkovin, "Effects of compressibility on turbulent flows," *Méchanique de la Turbulence*, vol. 367, p. 380, 1962.

[72] X. Wu and P. Moin, "Transitional and turbulent boundary layer with heat transfer," *Phys. Fluids*, vol. 22, no. 8, p. 085105, 2010.

[73] L. Duan, I. Beekman, and M. P. Martín, "Direct numerical simulation of hypersonic turbulent boundary layers. Part 3. Effect of Mach number," *J. Fluid Mech.*, vol. 672, pp. 245–267, 2011.

[74] T. Watanabe, Y. Sakai, K. Nagata, Y. Ito, and T. Hayase, "Turbulent mixing of passive scalar near turbulent and non-turbulent interface in mixing layers," *Phys. Fluids*, vol. 27, no. 8, p. 085109, 2015.

[75] R. R. Prasad and K. R. Sreenivasan, "Scalar interfaces in digital images of turbulent flows," *Exp. Fluids*, vol. 7, no. 4, pp. 259–264, 1989.

[76] C. B. da Silva and R. R. Taveira, "The thickness of the turbulent/nonturbulent interface is equal to the radius of the large vorticity structures near the edge of the shear layer," *Phys. Fluids*, vol. 22, no. 12, p. 121702, 2010.

[77] R. R. Taveira and C. B. da Silva, "Kinetic energy budgets near the turbulent/nonturbulent interface in jets," *Phys. Fluids*, vol. 25, p. 015114, 2013.

[78] M. Gampert, J. Boschung, F. Hennig, M. Gauding, and N. Peters, "The vorticity versus the scalar criterion for the detection of the turbulent/non-turbulent interface," *J. Fluid Mech.*, vol. 750, pp. 578–596, 2014.

[79] T. Watanabe, J. J. Riley, and K. Nagata, "Effects of stable stratification on turbulent/nonturbulent interfaces in turbulent mixing layers," *Phys. Rev. Fluids*, vol. 1, no. 4, p. 044301, 2016.

[80] R. D. Moser and P. Moin, "Direct numerical simulation of curved turbulent channel flow," *NACA Tech. Memo.*, no. 85974, 1984.

[81] T. Watanabe, R. Jaulino, R. R. Taveira, C. B. da Silva, K. Nagata, and Y. Sakai, "Role of an isolated eddy near the turbulent/non-turbulent interface layer," *Phys. Rev. Fluids*, vol. 2, no. 9, p. 094607, 2017.

[82] T. Watanabe, J. J. Riley, and K. Nagata, "Turbulent entrainment across turbulent-nonturbulent interfaces in stably stratified mixing layers," *Phys. Rev. Fluids*, vol. 2, no. 10, p. 104803, 2017.

[83] M. van Reeuwijk and M. Holzner, "The turbulence boundary of a temporal jet," *J. Fluid Mech.*, vol. 739, pp. 254–275, 2014.

[84] M. Holzner, A. Liberzon, N. Nikitin, B. Lüthi, W. Kinzelbach, and A. Tsinober, "A Lagrangian investigation of the small-scale features of turbulent entrainment through particle tracking and direct numerical simulation," *J. Fluid Mech.*, vol. 598, pp. 465–475, 2008.

[85] T. S. Silva, M. Zecchetto, and C. B. da Silva, "The scaling of the turbulent/non-turbulent interface at high Reynolds numbers," *J. Fluid Mech.*, vol. 843, pp. 156–179, 2018.

[86] T. Watanabe, Y. Sakai, K. Nagata, and Y. Ito, "Large eddy simulation study of turbulent kinetic energy and scalar variance budgets and turbulent/non-turbulent interface in planar jets," *Fluid Dyn. Res.*, vol. 48, no. 2, p. 021407, 2016.

[87] T. Watanabe, C. B. da Silva, Y. Sakai, K. Nagata, and T. Hayase, "Lagrangian properties of the entrainment across turbulent/non-turbulent interface layers," *Phys. Fluids*, vol. 28, no. 3, p. 031701, 2016.

[88] T. Maeder, N. A. Adams, and L. Kleiser, "Direct simulation of turbulent supersonic boundary layers by an extended temporal approach," *J. Fluid Mech.*, vol. 429, pp. 187–216, 2001.

[89] T. Watanabe, Y. Sakai, K. Nagata, Y. Ito, and T. Hayase, "Enstrophy and passive scalar transport near the turbulent/non-turbulent interface in a turbulent planar jet flow," *Phys. Fluids*, vol. 26, no. 10, p. 105103, 2014.

[90] T. S. Silva and C. B. da Silva, "The behaviour of the scalar gradient across the turbulent/non-turbulent interface in jets," *Phys. Fluids*, vol. 29, no. 8, p. 085106, 2017.

[91] H. Mouri, A. Hori, and Y. Kawashima, "Laboratory experiments for intense vortical structures in turbulence velocity fields," *Phys. Fluids*, vol. 19, no. 5, p. 055101, 2007.

[92] K. Chauhan, J. Philip, and I. Marusic, "Scaling of the turbulent/non-turbulent interface in boundary layers," *J. Fluid Mech.*, vol. 751, pp. 298–328, 2014.

[93] X. Zhang, T. Watanabe, and K. Nagata, "Turbulent/nonturbulent interfaces in high-resolution direct numerical simulation of temporally evolving compressible turbulent boundary layers," *Phys. Rev. Fluids*, vol. 3, no. 9, p. 094605, 2018.

[94] T. Watanabe, X. Zhang, and K. Nagata, "Turbulent/non-turbulent interfaces detected in DNS of incompressible turbulent boundary layers," *Phys. Fluids*, vol. 30, no. 3, p. 035102, 2018.

[95] A. Tsinober, *An informal conceptual introduction to turbulence*. Springer, 2009.

[96] T. Watanabe, Y. Sakai, K. Nagata, Y. Ito, and T. Hayase, "Vortex stretching and compression near the turbulent/nonturbulent interface in a planar jet," *J. Fluid Mech.*, vol. 758, pp. 754–785, 2014.

[97] T. Watanabe, C. B. da Silva, K. Nagata, and Y. Sakai, "Geometrical aspects of turbulent/non-turbulent interfaces with and without mean shear," *Phys. Fluids*, vol. 29, no. 8, p. 085105, 2017.

[98] B. Joung, "Real-world data and recommended dosage of non-vitamin k oral anticoagulants for korean patients," *Korean Circ. J.*, vol. 47, no. 6, pp. 833–841, 2017.

[99] J. Underberg, C. Cannon, D. Larrey, L. Makris, C. Schwamlein, H. Phillips, L. Bloeden, and D. Blom, "Global real-world data on the use of lomitapide in treating homozygous familial hypercholesterolemia: the lomitapide observational worldwide evaluation registry (lower), two-year data," *Circulation*, vol. 134, no. suppl_1, pp. A12117–A12117, 2016.

[100] H. Lasi, P. Fettke, H. G. Kemper, T. Feld, and M. Hoffmann, "Industry 4.0," *Bus. Inf. Syst. Eng.*, vol. 6, no. 4, pp. 239–242, 2014.

[101] Y. Lu, "Industry 4.0: A survey on technologies, applications and open research issues," *J. Ind. Inf. Integr.*, vol. 6, pp. 1–10, 2017.